Temporal and spatial hydrodynamic variability in a gravel-bed river: measurement, characterisation, and significance for spawning salmonids

by

Victoria Lounder

A thesis
presented to the University of Waterloo
in fulfillment of the
thesis requirement for the degree of
Master of Applied Science
in
Civil Engineering

Waterloo, Ontario, Canada, 2011

I hereby declare that I am the sole author of this thesis. This is a true copy of the thesis, including any required final revisions, as accepted by my examiners.

I understand that my thesis may be made electronically available to the public.

Abstract

The spatial and temporal flow field characteristics of a gravel-bed river supporting a robust rainbow trout (*Onchorhynchus mykiss*) and brown trout (*Salmo trutta*) fishery were studied in high resolution in attempts to hydraulically quantify the selection preferences and incubation characteristics of redds. Measurements were obtained at both the riffle- and redd-scale post-spawning, in addition to pre- and post-bed mobilization flow events. A Pulse Coherent Acoustic Doppler Profiler (PCADP) was adapted for use in the lotic environment where between 4000 to 5000 three-dimensional velocity measurements could be obtained on a daily basis at the riffle scale. Bed material samples were obtained and scour chains installed to characterise the bed mobility, critical shear, and macro-erosion of each riffle studied.

At the riffle-scale, seasonal variability in the mean and variance of commonly used hydrodynamic parameters (velocity, flow depth, Froude number, bed roughness, turbulent kinetic energy per unit area) was often explicitly related to changes in sampling discharge and channel structure. Riffle-scale directional semivariograms isolated varied scales of spatial dependency, and the occurrence of bed mobilizing and channel-forming discharge created a less smooth and poorly defined spatial structure. Redd-scale omnidirectional semivariograms presented the same response to channel-forming discharge, however overall did not reveal a coherent spatial structure. Although the commonly used Froude number did not present patterns or characteristics which could distinguish the redd properties from the riffle, the results for local velocity and turbulence at the redd-scale revealed evidence of optimal physical conditions for salmonid incubation, particularly convective flow acceleration which promotes downwelling at the egg pockets and unidirectional flow with low turbulence, which allows this behaviour to persist through a range in environmental flows.

Acknowledgements

I would like to thank my supervisor Dr. William Annable for his guidance and support in the past four years. Bill introduced me to the world of river research as an undergraduate student, and has provided me with countless opportunities to keep me engaged, involved, and ultimately passionate about this work. I cannot overstate how grateful I am for the guidance, advisement, and encouragement I received from Mr. Jack Imhof and Dr. Mike Power. Additionally, the assistance and foresight provided by Mason Marchildon while figuring out the field methods and post-processing is greatly appreciated.

The work which went into this thesis included countless hours in the field, and there are many people whose assistance cannot go unrecognized: Terry Ridgway, Ben Plumb, Mike McKie, Chris McKie, Rob Leonard, Nikita Tirskikh, Michael Szelwis, Kurtis Witzel, Maley Tudor, Aurelie Blanc, and Frank Hooijmeijer. Many hours were also spent developing the post-processing and plotting programs, and I will forever be indebted to Pete Thompson for his support and assistance.

To the department of Civil and Environmental Engineering, the National Science and Engineering Council (NSERC) - Discoveries Grant Program, and Trout Unlimited Canada: thank you for the support.

Table of Contents

List of Tables

List of Figures

List of Symbols

γ	specific weight of water	ML^{-3}
γ_s	specific weight of sediments	ML^{-3}
$\hat{\gamma}$	semivariance	-
κ	von Kármán constant ≈ 0.4	-
ν	kinematic viscosity of water	L^2T^{-1}
Ω	sinuosity	-
Φ_n	particle size	Φ-units
ρ	mass density of water $\approx 1000\,\mathrm{kg/m^3}$	ML^{-3}
ρ_s	mass density of sediment $\approx 2650\,\mathrm{kg/m^3}$	ML^{-3}
σ_n	standard deviation of velocity in the n-direction	LT^{-1}
τ_{*c}	critical dimensionless shear stress	-
τ_*	dimensionless shear stress	-
τ_0	bed shear stress	$ML^{-1}T^{-2}$
τ_c	critical shear stress	$ML^{-1}T^{-2}$
ξ	lag distance separating pairs of observations	L
d_c	critical particle diameter	L
d_n	grain size at which $n\%$ of the sample is finer by weight	L
d_s	sediment size	L

e_a	turbulent kinetic energy per unit area	MT^{-2}
f	Darcy-Weisbach friction factor	-
F_r	Froude number	-
g	gravitational acceleration	LT^{-2}
h	flow depth	L
k_s	Nikuradse equivalent grain roughness	L
N	number of velocity profiles collected	-
n	Manning resistance coefficient	-
$N(\xi)$	number of paired data at distance of ξ	-
p	profile height	L
Q	reach-averaged discharge	L^3T^{-1}
Q_{cn}	critical discharge for the $n\%$ particle size	L^3T^{-1}
R_e	Reynolds number	-
R_h	hydraulic radius	L
R_{e*}	grain shear Reynolds number	-
S_0	bed slope	LL^{-1}
s_I	Inman's sorting coefficient	-
S_w	water surface slope	LL^{-1}
s_{FW}	Folk and Ward sorting coefficient	-
$sk_{a,W}$	Warren's skewness coefficient	-
$sk_{g,F}$	Fredle index of skewness	-
U	local depth-averaged velocity	LT^{-1}
$u(z)$	point velocity at a depth of z	LT^{-1}
u_*	shear velocity	LT^{-1}
V	cross-sectionally averaged velocity	LT^{-1}
z_0	roughness length	L

Chapter 1

Introduction

Important conditions in river ecology contributing to habitat diversity and aquatic productivity are the hydraulic characteristics, which vary at numerous inter-dependent scales of time and space. The hydrologic and hydraulic environment (habitat) of stream-dwelling organisms is formed by the interaction of a number of variables, including: velocity, water depth, discharge, substrate composition, and channel configuration. At the reach scale, a river may manifest large-scale homogeneous geomorphic and hydrologic conditions, but will also display an important variety of smaller-scale hydraulic elements which have a large influence on local biotic communities (Kemp *et al.*, 2000; Thomson *et al.*, 2001). These spatial variations are due to physical characteristics of the river, such as vegetation, channel form, and roughness elements. Temporal variations in hydrologic and hydraulic conditions are primarily due to changes in discharge, but are also related to climate and changes in roughness and structure as a result of channel-altering discharges (Casado *et al.*, 2005). High biodiversity and aquatic ecosystem health has been attributed to high hydraulic spatial variability (Dyer & Thoms, 2006). It is therefore of value to develop standardised methods for comparing spatial and temporal hydraulic heterogeneity between river reaches, in order to develop predictive models of fluvial ecosystems (Roy *et al.*, 2010).

The complexity of fish behaviour generates additional challenges when attempting to comprehend the distribution and abundance of populations, or when striving to provide ideal habitat conditions which will be utilized because salmonids live in instantaneous velocity and turbulence conditions, not in an averaged environment (Dyer & Thoms, 2006; Kilsby & Walker, 2010). Furthermore, these velocity conditions vary under the broad range of natural flows conveyed, particularly in gravel bed rivers. The nature of turbulent flow in shallow streams involves complex eddy-like phenomena, which may vary over a range of scales of time and space (Dingman, 2009). The correlation and confounding of these physical variables in the lotic environment renders the selection of variables to study a further challenge (Heede & Rinne, 1990). Systematic research in turbulent flow conditions as they

relate to lotic habitat must accommodate for the complexity and unpredictability of natural systems and further research on appropriate sampling strategies and spatial analysis methods for gravel bed streams is required. A scale dependent approach to investigating stream ecosystems must involve consideration of hydraulic, morphological, and biological variables.

The purpose of this study was to measure and characterise velocity and profile-derived local variables, and examine their relationship with riffle dynamics and salmonid spawning site selection. High-resolution three-dimensional velocity measurements were repeated four times within a year on four riffles of a gravel bed stream in Southwestern Ontario. The measurements captured a distinct quasi-instantaneous description of the hydrodynamic behaviour at wadeable flow depths. Four brown and rainbow trout redds constructed on these riffles were more closely and frequently investigated using the same techniques, during the incubation and emergence periods of the salmonid life-cycle. These hydraulic measurements, along with substrate composition and a complete flow record for the reach, provided the details necessary for a quantified characterisation of these four similar but distinct units. By using the same methods to examine selected salmonid spawning habitat, it was possible to empirically identify the hydrodynamic characteristics which distinguished the selected sites.

The intensive discretized method applied in this study for velocity measurement provides an objective seasonal series of hydrodynamic qualities which contains significantly more detail of the phenomenal variance of a gravel bed system than traditional single-point, one-time measurements of physical conditions. The complexities of scale in a turbulent fluvial system were revealed in the spatial analysis at both the riffle and redd scale, and the relationship between quantitative variables (velocity, depth, Froude) and discharge are shown to be varied at both of these scales. These results contribute to the pursuit of creating reproducible associations between hydraulic patterns and substrate conditions necessary for reinstating and maintaining productive ecosystems in gravel bed river ecosystems.

Chapter 2

Background

A scalar approach to river ecology which groups regions of relative homogeneity (biotic, hydraulic, physio-chemical) has often taken a hierarchical approach (Woods *et al.*, 1996; Gordon *et al.*, 2006; Parsons *et al.*, 2004). Figure 2.1 illustrates the convergence of biotic and hydraulic spatial scales of various units used when discussing environmental flows and their impacts on habitat in gravel-bed rivers.

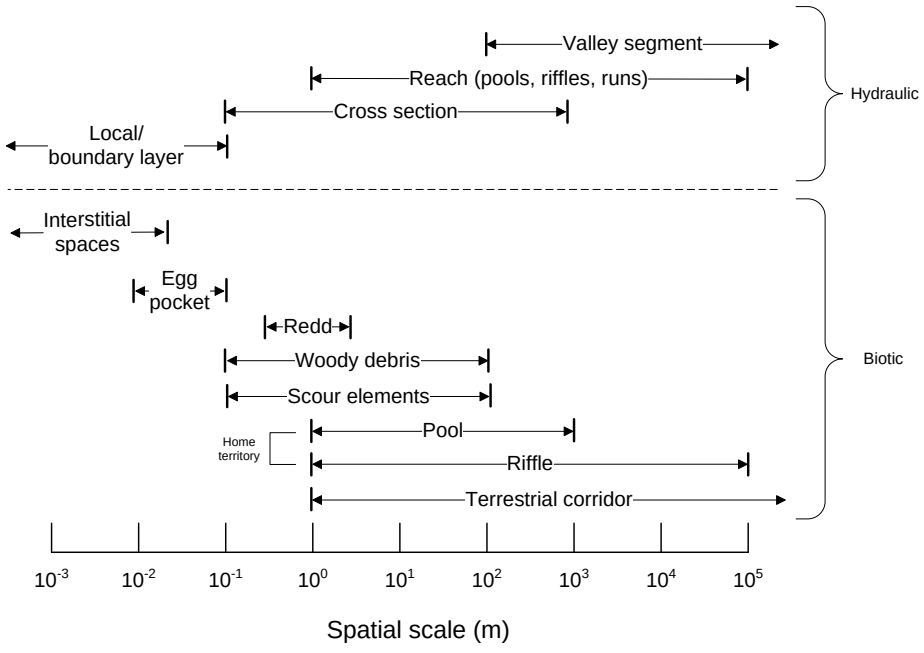

Figure 2.1: Spatial scales associated with hydraulic and biotic features in gravel-bed streams, based on Dingman (2009) with elements from Imhof *et al.* (1996)

2.1 Spawning habitat characteristics

When a female salmonid spawns in a gravel-bed stream, she turns on her side and begins to dig by flexing her tail and driving it into the bed to clear a hollow in the substrate (Figure 2.2). It has been suggested that the females can move particles up to 10% of their body length (Kondolf *et al.*, 2008). This movement also typically flushes fine sediments from the substrate, leaving clean gravels and cobbles. Fertilized eggs are deposited into the depression, and the female immediately covers the eggs with sediment, creating a subsequent pit upstream. It has been proposed and investigated that the unique morphology of salmonid redds may lead to optimal physical conditions for egg incubation (Chapman, 1988).

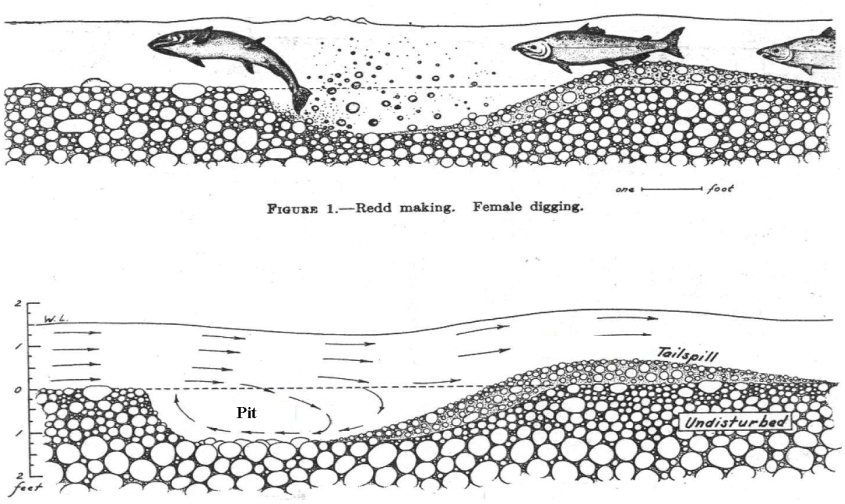

Figure 2.2: Salmonid redd construction modified from Burner (1951)

There exist many scale-dependent factors which have been found to influence the location within a river where adult salmonids spawn (Reiser, 1976; Witzel & MacCrimmon, 1983; Zimmer & Power, 2006; Moir & Pasternack, 2008). Flow depth, velocity, and substrate composition are the most commonly used abiotic descriptors of salmonid spawning habitat, however, there are many additional factors which have been highlighted such as temperature, inter-gravel dissolved oxygen, hydraulic gradient and hyporheic flow, channel morphology, and bed stability (Ottaway *et al.*, 1981; Witzel & MacCrimmon, 1983; Crisp & Carling, 1989; Armstrong *et al.*, 2003; Kondolf *et al.*, 2008). Figure 2.3 summarizes the recognized physical mechanisms, requirements, and controlling factors for the principle stages of salmonid spawning. The interplay of these factors at various times during the life stages of salmonids dictates the mechanics for opportunity and determines the survival of the salmonids (Witzel & MacCrimmon, 1983; Kondolf & Wolman, 1993; Knapp & Vredenburg, 1996; Schmetterling, 2000)

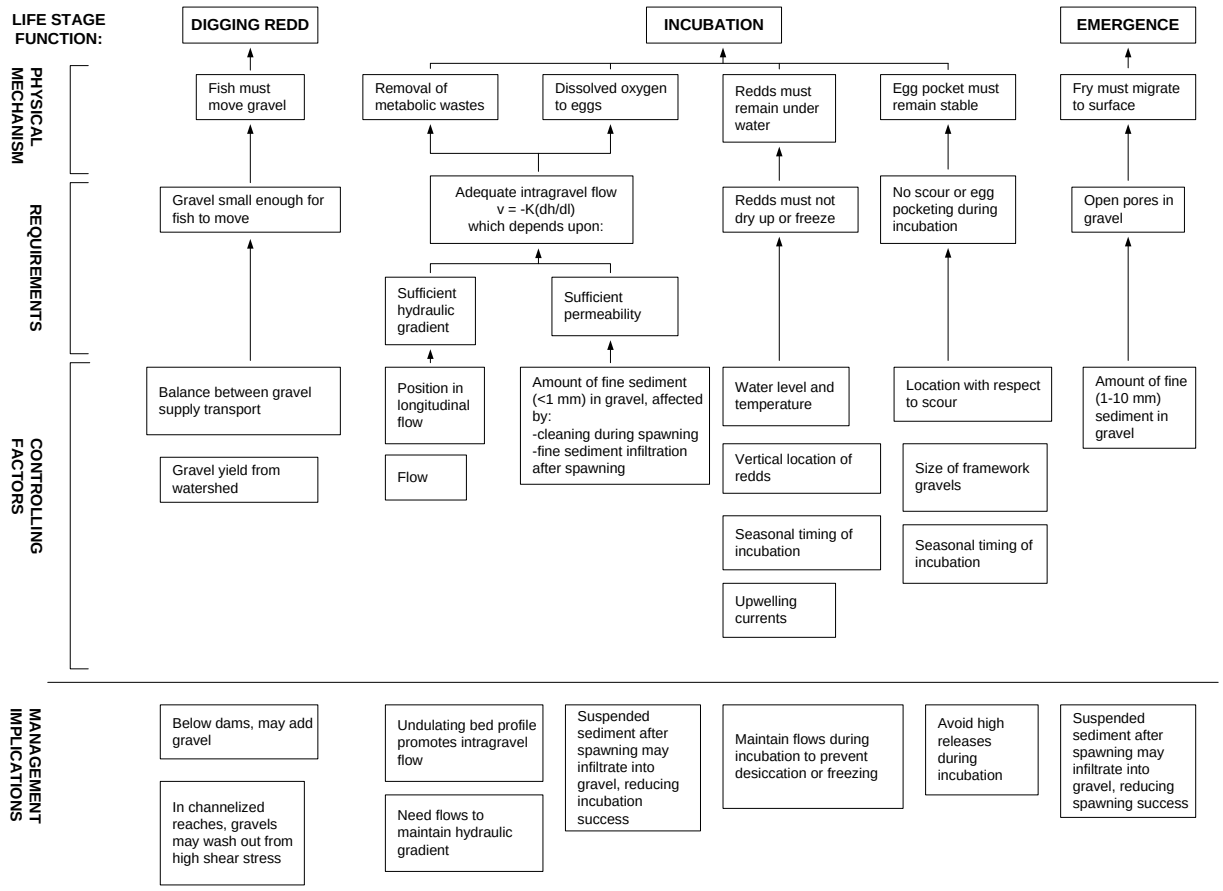

Figure 2.3: Physical requirements of salmonids during redd construction, incubation, and emergence (Kondolf *et al.*, 2008)

The tradeoff between high and low water velocities around redds must balance adult energy expenditure during construction and with the need for sufficient flow to oxygenate and remove metabolic waste from the redd during incubation (Chapman, 1988). High flows during incubation and emergence have been inversely related to year-class strength of stream-dwelling brown trout (Spina, 2001). The inter-gravel stage of incubation is the period during which the majority of salmonid mortality occurs (Rennie & Millar, 2000). Flow depths at redds are typically related to fish size; it is unlikely that a fish would spawn in water shallower than its body depth (Crisp & Carling, 1989).

At the crest of a riffle, the lower water surface elevation on the riffle creates a hydraulic gradient which induces downwelling at this location (Kondolf, 2000). Similarly, the structure of the redd in Figure 2.2 has also been found to induce downwelling by creating a hydraulic gradient across the redd mound, inducing flow from the pit region (high pressure

region) into the unconsolidated tailspill sediment (Thurow & King, 1994; Wu, 2000). The dune-like structure of the redd also induces convective acceleration over the crest of the tailspill further facilitating movement of water (including oxygen and metabolic waste) through the tailspill sediments (Cooper, 1965; Thibodeaux & Boyle, 1987; Schmetterling, 2000).

Substrate composition of selected spawning habitat for salmonids is characterised by coarse gravel which contains few fine particles (Burner, 1951; Kondolf *et al.*, 2008). In regards to bed mobility, redd scour is often postulated as the cause of reduced reproductive success of brown trout (Anderson, 1983). Rennie & Millar (2000) found using spatially intensive wiffle-balls (similar to scour chains) that a bankfull event on a gravel-bed stream in British Columbia caused scour of the tailspill of chum salmon (*Oncorhynchus keta*) redds exceeding burial depth, but not at the egg pocket locations. The spatial variability of scour and fill locations was high, and the egg pockets maintained a mobility similar to the rest of the bed while the tailspill did not. Montgomery *et al.* (1996) found that spawning related bed modifications reduced the likelihood of bed mobility, indicating that salmonids protect their embryos from scour by increasing the critical shear stress of the bed structure at the egg pockets, and that high discharges during incubation may not necessarily imply mortality. Rennie & Millar (2000) found the structure of the tailspill to be more readily mobilized than the surrounding bed or the egg pocket, which implies that analytical predictions of redd scour remain uncertain.

2.2 Turbulent velocity profiles

2.2.1 Flow characteristics

Open-channel flow is governed by the interaction of inertial, gravitational, and resistance (friction) forces (Graf & Altinakar, 1998). Flow may be defined as turbulent if the ratio of the inertial forces to the viscous forces is high (Chow, 1959). In open-channel flow, the ratio of turbulent to laminar resistance is typically represented by the Reynolds number (R_e), and describes the smoothness of the flow:

$$R_e = \frac{Vl}{\nu} \tag{2.1}$$

Where:

$$\begin{aligned} V &= \text{mean velocity} \\ l &= \text{characteristic length} \\ \nu &= \text{kinematic viscosity} \end{aligned}$$

A ratio greater than 2000 is generally accepted as the limit for turbulent flow, and virtually all open channel flow in natural channels can be classified as fully turbulent (Chow, 1959; Graf & Altinakar, 1998; Dingman, 2009). Irregular velocity fluctuations in open-channel flow are a characteristic indicator of this turbulence (Leopold & Maddock, 1953; Julien, 2010).

The ratio of the inertial forces to gravitational forces in open-channel flow is represented by the dimensionless Froude number (F_r), and is used to classify the nature of flow as sub- or supercritical ($F_r < 1$ and $F_r > 1$, respectively):

$$F_r = \frac{V}{\sqrt{gh}} \tag{2.2}$$

While the Reynolds number is considered a measure of internal flow conditions and resistance, the Froude number gives an indication of bulk flow characteristics and the quality of flow at the surface (Gordon *et al.*, 2006). It is commonly used in the field of ecohydraulics to hydraulically define and classify lotic habitat units, and in the majority of natural bed river flows it is found to be in the subcritical regime ($F_r < 1$) (Kemp *et al.*, 2000; Armstrong *et al.*, 2003; Gordon *et al.*, 2006; Moir & Pasternack, 2008).

2.2.2 Vertical velocity distribution

Formulating expressions and characterising resistance forces is a more complex problem in open-channel hydraulics, and the vertical velocity profile is an important tool in analysis (Dingman, 2009). By balancing the driving and resisting forces in the water column, a velocity distribution can be derived for turbulent flow in a wide channel. The law of the wall (Prandtl-von Kármán law) predicts that velocity in turbulent flows is logarithmically distributed with respect to depth (Von Kármán, 1930; Julien, 2010):

$$u(z) = a + \frac{u_*}{\kappa} \ln \frac{z}{z_0} \tag{2.3}$$

Where:

$u(z)$	=	time-averaged streamwise velocity at elevation z above the bed
a	=	additive constant
u_*	=	shear/friction velocity
κ	=	von Kármán's constant
z_0	=	roughness length, equivalent to the notional height above the bed where the velocity appears to be 0

The use of the log law is derived in uniform flow, but has been confirmed experimentally for gravel-bed rivers in non-uniform conditions (accelerating/decelerating) (Smart, 1999; Afzalimehr & Anctil, 2001; Song & Chiew, 2001; Marchildon *et al.*, 2011). The von Kármán constant κ is a proportionality factor in the relationship between mixing length and distance above the boundary. For flows carrying high concentrations of suspended sediment, κ has been found to be as low as 0.2 although a value of 0.4 is most commonly used (Yalin, 1992; Dingman, 2009; Julien, 2010). The nature of the Prandtl-von Kármán (P-vK) universal velocity-distribution law is such that most of the change in velocity occurs very close to the bed due to the fact that turbulent eddies are much more effective distributors of momentum than molecular viscosity, which controls the momentum distribution very close to the bed where eddy viscosity decreases. The nose-level velocity, measured at 10 cm from the bed, is considered the velocity which influences a salmonid's ability to hold station (Ottaway *et al.*, 1981; Chapman, 1988). The nose-level velocity can be used to characterise the flow conditions which the organisms most likely experience, and it differs from the depth-averaged velocity (Marchildon *et al.*, 2011).

The debate over appropriate velocity profile distributions and depths over which the distributions are applicable is complex (Dingman, 2009). "Far" above the bed, it is expected that the velocity gradient only depends upon the distance above the bed, and not on bed roughness. Afzalimehr & Rennie (2009) studied the behaviour of velocity profiles and shear velocity in gravel-bed rivers, based upon the premise that two regions of flow exist in gravel-bed rivers: near bed where the log law persists and the outer region where velocity profile deviates from the log law. In the outer region velocity may be represented by another distribution, such as the parabolic law or the velocity-defect law, which requires measurement of water surface velocity (Dingman, 2009). Middleton & Southard (1984); Smart (1999) and Bridge (2003) studied velocity data from gravel-bed rivers, and found that the Prandtl-von Kármán law "fits the velocity profile without great error all the way to the free surface" in turbulent boundary layer flows. Despite theoretical indications of invalidity, the P-vK law is generally accepted as the theoretical local velocity profile in wide uniform turbulent flows.

The shear velocity is a measure of the intensity of turbulent velocity fluctuations, expressed in kinematic (velocity) terms (Dingman, 2009). It can also be considered a characteristic near-bed velocity in turbulent flow. The boundary shear stress τ_0 defines the shear velocity:

$$\tau_0 = \rho u_*^2 \tag{2.4}$$

The law of the wall assumes that the total shear stress throughout the flow depth is due to turbulence. However, the "no-slip/zero velocity condition" at the boundary implies that there must be a zone close to the bed in which the Reynolds numbers are low enough to be considered laminar (the viscous sublayer) and that there is a transition/buffer layer where both viscous and turbulent shear stresses are important (Dingman, 2009). The buffer layer

is characterised by very energetic small-scale turbulence and a fluctuating upper boundary that is typically very thin relative to typical flow depths in gravel-bed rivers and is often neglected when analyzing the vertical velocity profile (Middleton & Southard, 1984). The flow boundary may be classified as hydraulically smooth or rough and is determined from the height of the roughness elements (d_s) relative to the thickness of the viscous sublayer. The boundary is evaluated using the grain shear Reynolds number (R_{e*}) as:

$$R_{e*} \equiv \frac{u_* d_s}{\nu} \tag{2.5}$$

If the height of the roughness layer exceeds six times the height of the viscous sublayer ($R_{e*} > 70$), the boundary layer is considered hydraulically rough and the logarithmic distribution is applicable to the velocity profile close to the bed (Julien, 2010).

The roughness length z_0 is always lower than the surface grain diameter and can be determined graphically from the intercept of Equation 2.3. It may also be empirically related to Nikuradses equivalent sand grain roughness (k_s) on rough boundaries (Nikuradse, 1933; Leopold, 1994; Julien, 2010):

$$k_s \approx 30 z_0 \tag{2.6}$$

Nikuradse's equivalent sand grain roughness height represents the roughness of the undulated surface of the bed and is a function of the shape, height and width of the roughness elements (Yalin, 1992; Schlichting & Gersten, 2000). Values for k_s can be estimated from grain size distributions. The values $6.8d_{50}$, $5.2d_{65}$, and $3.5d_{84}$ are most commonly used in fluvial geomorphology, where d_{50}, d_{65}, and d_{84} are the grain size diameters (Julien, 2010). These single-size estimates for roughness do not account for orientation or protrusion of particles, and Smart (1999) found that z_0 derived from turbulent profiles was independent of local bed material sizes. Nikora *et al.* (1998) developed an expression for roughness by considering the surface as a random field of elevations. By calculating a height using the standard deviation of surveyed bed elevation points in a predefined rectangular area, a localized measure of topographic variability can be developed, which can be used to characterise roughness.

The Manning formula is the most commonly used North American empirical equation for representing uniform flow in open-channels (French, 1985). Channel conveyance is quantified as (Gauckler, 1867; Dingman, 2009; Julien, 2010):

$$V = \frac{1}{n} R^{2/3} S_0^{1/2} \tag{2.7}$$

Where:

R = hydraulic radius
S = energy gradient
n = Manning resistance coefficient

Manning's n roughness varies slightly with depth, and empirically derived values for natural bed streams range from 0.02 to 0.08 (Leopold, 1994). Work by Smart (1999) highlights the challenges of identifying a representative roughness parameter in gravel-bed rivers, where there is a large range in bed material sizes and local water surface slope S_w is difficult to reliably estimate. The significance of scale (Figure 2.1) when considering roughness in alluvial channels remains to be thoroughly investigated (Yen, 2002).

2.2.3 Profile-based turbulence

A depth-wise modification to conventional time-series-based turbulent kinetic energy was developed by Marchildon (2009), and uses the variance between time-averaged velocities in the entire profile:

$$\bar{e}_a = \frac{1}{2}\rho p \left(\sigma_x^2 + \sigma_y^2 + \sigma_z^2\right) \tag{2.8}$$

Where:

$$\begin{aligned} \sigma_x, \sigma_y, \sigma_z &= \text{depth-averaged profile-based variance of velocities in the x, y, and z} \\ &= \text{direction} \\ p &= \text{length of velocity profile} \end{aligned}$$

Equation 2.8 therefore characterises the vertical variance of time-averaged velocity, and provides a quasi-three-dimensional metric of profile-based variance. This variable can assist in describing the spatiotemporal patterns of macroturbulence, but will not provide details on coherent turbulent flow structures.

2.3 Velocity measurement

The sampling effort involved in capturing multiple-point velocity profiles at a cross section scale (Figure 2.1) has decreased significantly in recent years as the use of Doppler profilers has become popular. Nevertheless, much research still remains to understand the capabilities and limitations of these technologies at a local scale (González *et al.*, 1996; Lacy *et al.*, 2005; Tilston, 2005; Kostaschuk *et al.*, 2005; Oberg *et al.*, 2007). The advantages of profile-based velocity measurement include a more accurate depiction of the velocity behaviour of the entire flow depth in shallow turbulent streams, which may provide better estimates of boundary shear stress given that "the inclusion of near-bed velocities is critical for the estimation of bed shear stress in a shallow river environment" (Biron *et al.*, 1998). Bedload transport analysis is dependent upon the estimation of the primary parameters

such as bed shear (τ_0) from the velocity profile, and uncertainty in their estimates must be fully acknowledged. It is also important to make the distinction between the intent to measure mean properties versus the turbulent characteristics of flow, that require detailed time-series velocity data.

The field work required for high-resolution sub-reach scale velocity surveys in rivers is both time consuming and expensive. Intuitively, any spatial data collection methodology benefits from higher sampling resolution. The priority of velocity measurement in a natural system is not only to minimize sampling effort and maximize interpolation accuracy, but also to minimize discharge variability in order to ensure stationarity in a single data set. The change in hydromorphological characteristics due to changes in discharge during sampling is rarely addressed (Casado *et al.*, 2005; Legleiter *et al.*, 2007). Of the few published works investigating suitable sampling strategies, Roy (2006) tested several interpolation models to determine the optimal sampling density required to develop an accurate interpolation model from grid-based velocity data. Using an acoustic Doppler velocimeter to characterise turbulence, a density of 4 measurements per square meter was found to be optimal in a 12 m wide gravel-bed stream. Similarly, Casado *et al.* (2005) compared transect versus grid sampling strategies on a reach scale ($L = 200$ m) and found that a transect sampling strategy performed poorly in the recognition of spatial pattern using geostatistical techniques. However, Legleiter *et al.* (2007) successfully employed geostatistical analysis with velocity data collected on transects (0.5 m vs 1.5 m resolution, transverse to streamwise). Bradbrook *et al.* (2000) noted that it is of prime importance to include the spatial scales at which the spatial patterns of study variables are expected to persist when selecting a sampling strategy, be it grid- or transect-based.

2.4 Bed mobility

Simplified stability analysis of particles on a river bed can describe the incipient motion of uniform grain sizes in a horizontal channel (Julien, 2010). As the boundary shear stress in alluvial channels increases, a threshold is reached at which point the bed material is no longer stable. The threshold is defined by the balance of resisting forces due to particle weights and the hydrodynamic moments of force. The critical Shields parameter τ_{*c} is used to describe the ratio of these forces, and is a function of the particle size:

$$\tau_{*c} = \frac{\tau_c}{(\gamma_s - \gamma_m)\, d_n} \tag{2.9}$$

Where:

τ_c = critical shear stress
γ_s = specific weight of sediment
γ_m = specific weight of water-sediment mixture
d_n = grain size at which n% by weight of the sample bed material is finer

A value of $\tau_{*c} \approx 0.047$ is widely used for single-particle sizes in turbulent flow over hydraulically rough gravel-bed streams, when $R_{e*} > 50$ (see Equation 2.5) (Meyer-Peter & Müller, 1948; Julien, 2010). The critical boundary shear stress can then be isolated as the following:

$$\tau_c = 0.047 \left(\gamma_s - \gamma_m\right) d_s \tag{2.10}$$

The measurement of the scour and fill dynamics of sediment is important in understanding the conditions of spawning and incubation habitat (Nawa & Frissell, 1993). While empirical calculation of threshold shear stress determines potential for bed erosion, most bed-load transport in gravel-bed streams occurs during flows approaching and exceeding bankfull discharge, in discrete scour and fill events (Nawa & Frissell, 1993; Leopold *et al.*, 1995).

2.5 Spatial statistics

A semivariance approach can be used to describe the spatial structure of flow variables, by incorporating variance as well as spatial structure. The semivariance ($\hat{\gamma}$) is calculated as half the average squared difference between the values of every data pair, and takes the units of the observed parameter squared (Goovaerts, 1997):

$$\hat{\gamma}(\xi) = \frac{1}{2} \cdot \frac{1}{N(\xi)} \sum_{i=1}^{N(\xi)} \left[Z(x_i + \xi) - Z(x_i)\right]^2 \tag{2.11}$$

Where:

ξ = lag distance separating pairs of observations
$N(\xi)$ = number of paired data at distance of ξ
$Z(x_i)$ = value of a given observation at location x_i

The semivariogram described by Equation 2.11 is based on the principle that on average, two observations closer together are more similar than two observations farther apart, and

the dissimilarity of observations is expressed as a function of the distance which separates them (ξ), as in Figure 3.10 (Legleiter *et al.*, 2007). The nature of river flow indicates that two directionally-dependent spatial patterns may emerge - downstream and transverse. An omni-directional semivariogram (equal circle radius) may therefore not reveal isolated patterns, and may in fact camouflage apparent spatial dependencies. By restricting the angular tolerance around the lag distance, directional semivariograms in the streamwise and transverse direction can be created, and the degree of continuity of a property in a specific orientation can be measured (Chiles & Delfiner, 1999; Roy, 2006).

Chapter 3

Methodology

3.1 Site selection

The Apps' Mill reach of Whitemans Creek was selected as a suitable study site due to its successful spawning reputation, existing previous topographic surveys and velocity measurements, and ease of access. Whitemans Creek watershed is a sub-catchment of the Grand River watershed (Figure 3.1). The river drains an area of 383 km^2, and discharges into the Grand River 20 km north west of Brantford, Ontario. The watershed is predominantly agricultural with a domesticated land use remaining relatively constant over the past 50 years. Current urban land use is estimated at less than 5%, and total impervious land cover is only 3.6% (Ontario Ministry of Natural Resources, 2008).

The study reach is primarily comprised of recent sandy glacio-fluvial deposits and the creek cuts through the Norfolk Sand Plain for several kilometres upstream (Ontario Geological Survey, 2007). The Water Survey of Canada operates a water level and streamflow gauge station at the upstream extent of the reach, at Cleaver Road Bridge (WSC 02GB008), as illustrated in Figure 3.2. Bankfull discharge at Whitemans Creek is estimated to be 40 m^3/s determined from both field calibration and a Log-Pearson analysis (Hartley, 1999; Marchildon, 2009).

Based upon results from previous spawning surveys (Marchildon, 2009), current fluvial conditions, and anecdotal guidance, three riffles were selected for detailed analysis and study. They will be referred to hereinafter as R1, R2, R3 (Figure 3.2). One of the initial objectives of the study was to examine the pre-to-post-spawning hydraulic conditions of salmonid redds, in order to identify selection patterns made by salmonids. In preparation for the brown trout spawning season in the autumn, velocity measurements were taken on these riffles in early fall 2009 with the intention of capturing pre-spawning conditions on these riffles. When water temperature and flow conditions indicated that spawning was

most likely completed in early October, a reach-long spawning survey was undertaken to identify established and attempted redds. A Trimble Geo XT sub-metre accurate Global Positioning System was used to locate three redds identified on a riffle which was not included in the original study, hereinafter R4 (Figure 3.2). Given that brown trout redds had not been identified on the three other riffles, it was decided that R4 should be included in the study, and velocity measurements were taken on this riffle in mid-October 2009, post-spawning activity. Velocity measurements above and proximal to the redds were continued throughout the fall and winter approximately every month and all riffles were re-surveyed in early February 2010. Following the major spring freshet event in mid-March, R2 and R4 were re-surveyed. Flow and weather conditions did not permit R1 and R3 to be measured until after another substantial event in early April. Rainbow trout spawning was observed through the reach both in early April, prior to this event, and immediately following this event. However, only a single rainbow trout redd was identified in the entire study reach, which was located on R3. This redd was monitored again through the spring and early summer, and all riffles were re-surveyed for the summer sampling season in late June, as seen in Figure 3.3.

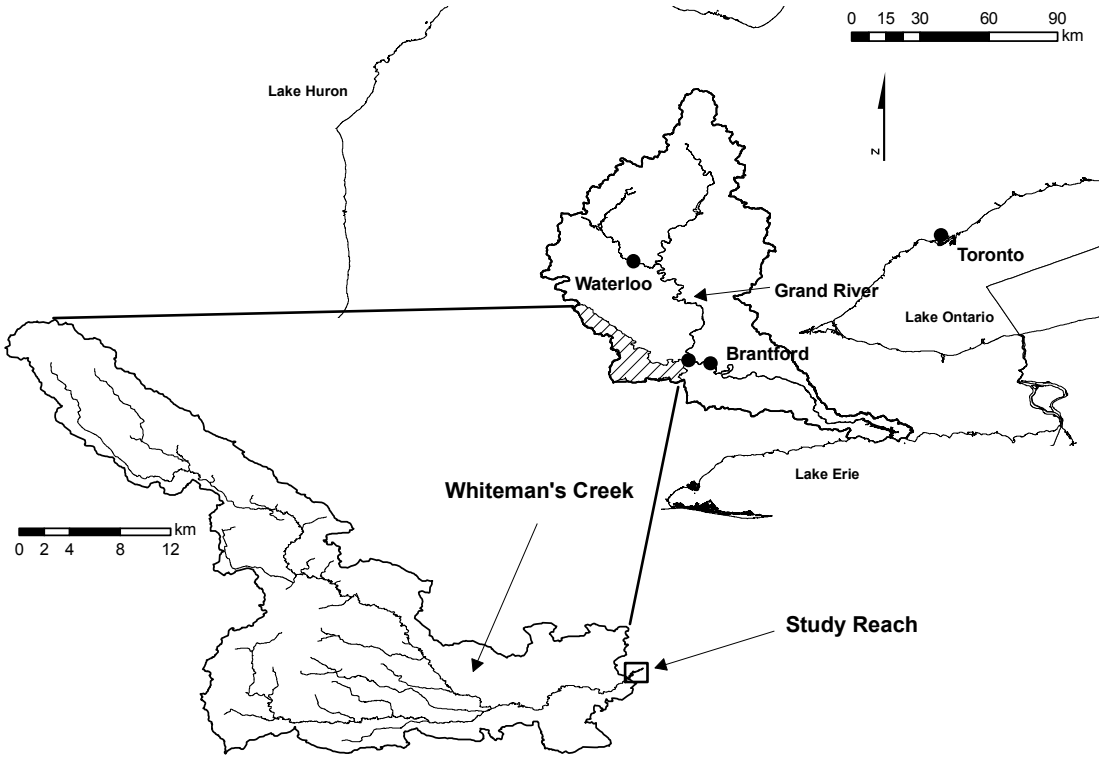

Figure 3.1: Site map of Whiteman's Creek watershed in Southwestern Ontario

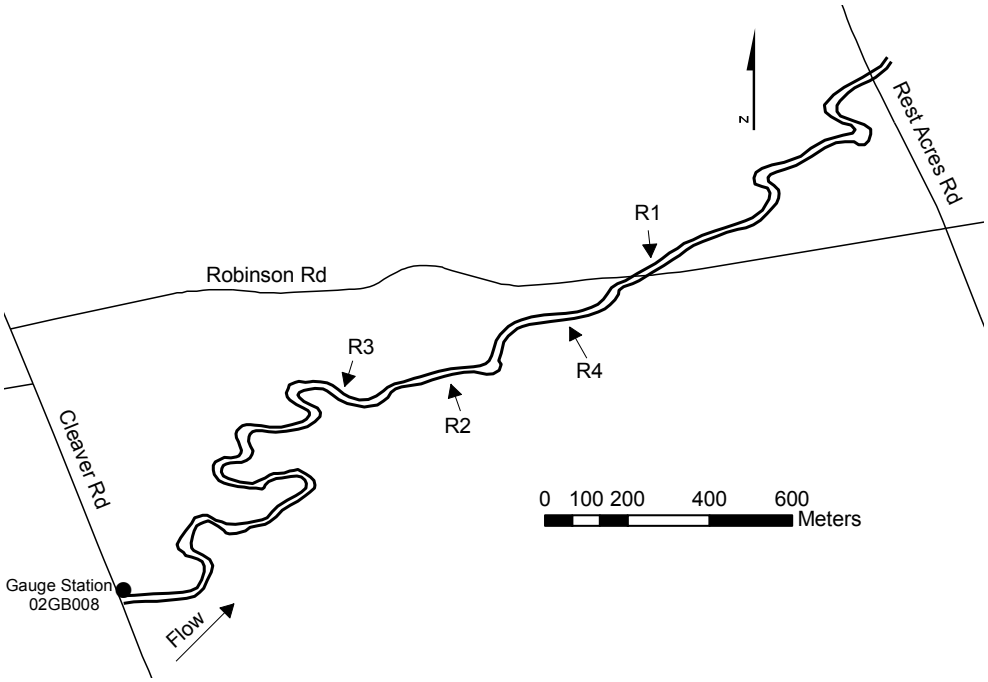

Figure 3.2: Study reach of Whiteman's Creek at Apps' Mill Conservation Area

The discharge through the study reach during velocity measurement ranged from 4-8% of the bankfull discharge, with the exception of the fall measurements on R1 (11%). An attempt was made to minimize the variability in discharge during measurement, however, the occurrence of optimal flow and meteorological conditions were not always achieved due to the constraints of field work conditions. The sampling priority was to collect velocity measurements at all riffles in as short as time as possible in order to ensure constant flow conditions, within the limits of available windows in wadeable flow depths and weather conditions.

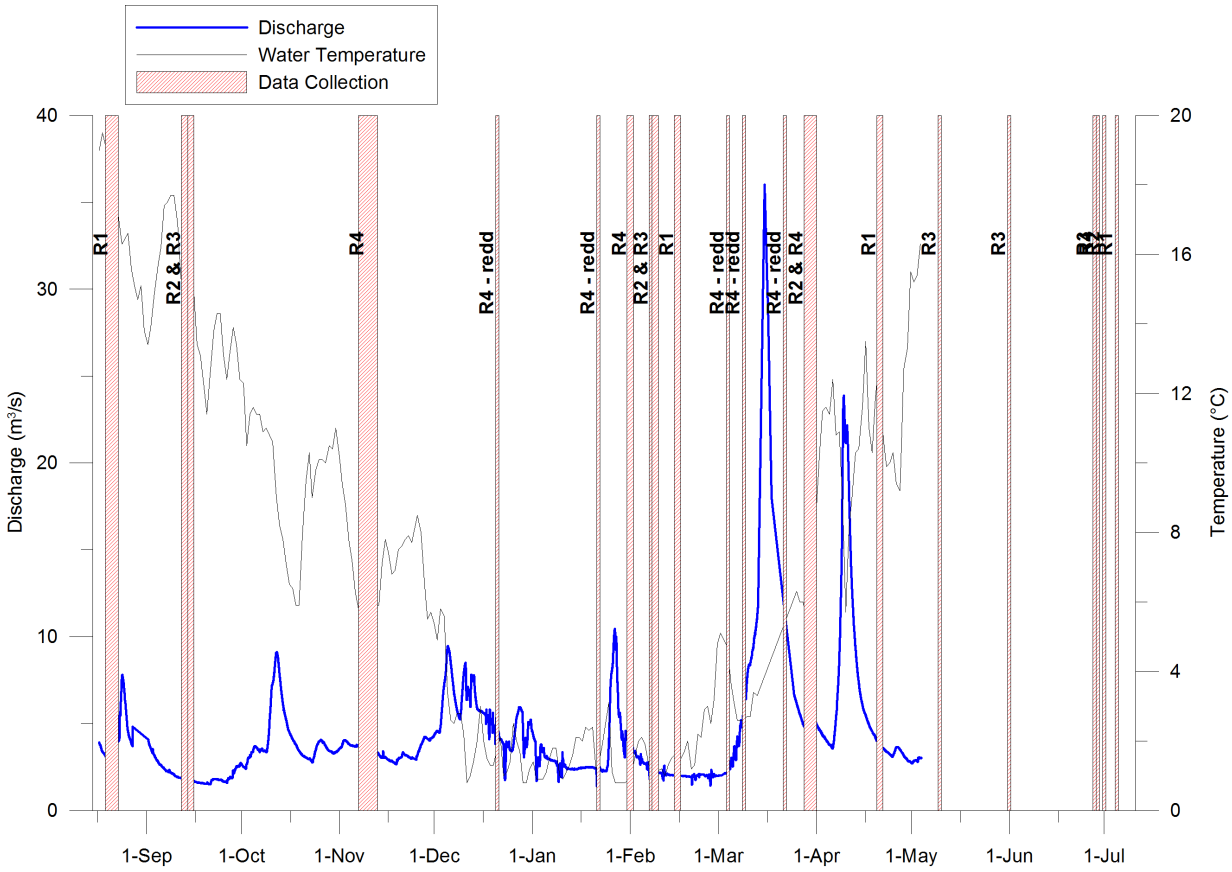

Figure 3.3: Chronology of velocity measurements taken at each study riffle at Whiteman's Creek, including daily average discharge and water temperature

3.2 Data collection

3.2.1 Velocity measurement

A downward-looking Sontek pulse coherent acoustic Doppler profiler (PCADP) was selected to acquire velocity measurements for its high precision in the boundary layer environment and the ability to measure at a high vertical resolution (vertically to 1.6 cm depth cell intervals). A typical ADP uses the Doppler shift principle to determine water velocity: transducers emit a beam of sound which is reflected by suspended particles in the water column. The frequency shift of the returning signal is used to determine the water velocity. The pulse coherent processing mode of the Doppler profiler designates that not one but two pulses are transmitted from each of the three transducers, angled at 15°, and the change in

phase between the two pulses is used to determine the water velocity. There exists therefore a trade-off between maximum velocity and depth range: streamwise velocities greater than 1.5 m/s must be associated with flow depths smaller than 0.5 m (SonTek/YSI, 2004). The PCADP is also limited by a minimum depth requirement as a blanking distance of 5 cm below the transducers is required to recover from transmitting the acoustic pulse and to dissipate any potential flow disturbance created by the probe. Although designed

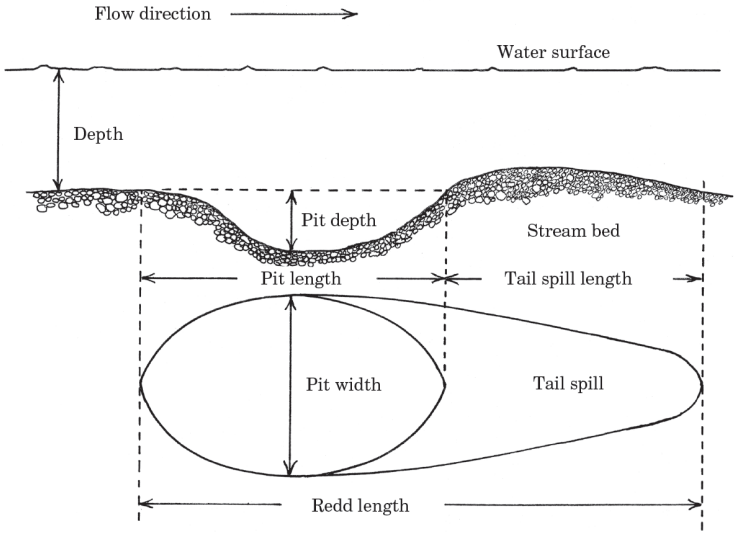

Figure 3.4: Longitudinal cross section and plan view of typical salmonid redd construction (Zimmer & Power, 2006)

primarily for long-term autonomous deployment, the PCADP system has been adapted to collect high resolution discretized velocity data at the riffle-scale (Marchildon, 2009). A table-like apparatus (cage) with a track was designed to accurately and efficiently discretize the region of the river to be studied. A trade-off between intensive and extensive data collection was made in an effort to collect velocity measurements on all four riffles in a short time-window to ensure steady discharge conditions. A planometric resolution of 80 cm was selected for all non-redd area measurements. The scale and structure of a salmonid redd is illustrated in Figure 3.4. When sampling velocities around a redd, a resolution of 40 cm was used corresponding to the lower scale of spatial structure manifested by redd features. A specific terminology for scales of measurement was adopted, as illustrated in Figure 3.5: cages, nodes (the planometric location of a velocity profile), and profile points (locations of individual velocity measurements, corresponding to the average velocity in a single depth cell).

The Sontek software ViewADP was used to initially process, visualize, and export the following data from the PCADP: three time-averaged velocity values (u_x, u_y, u_z),

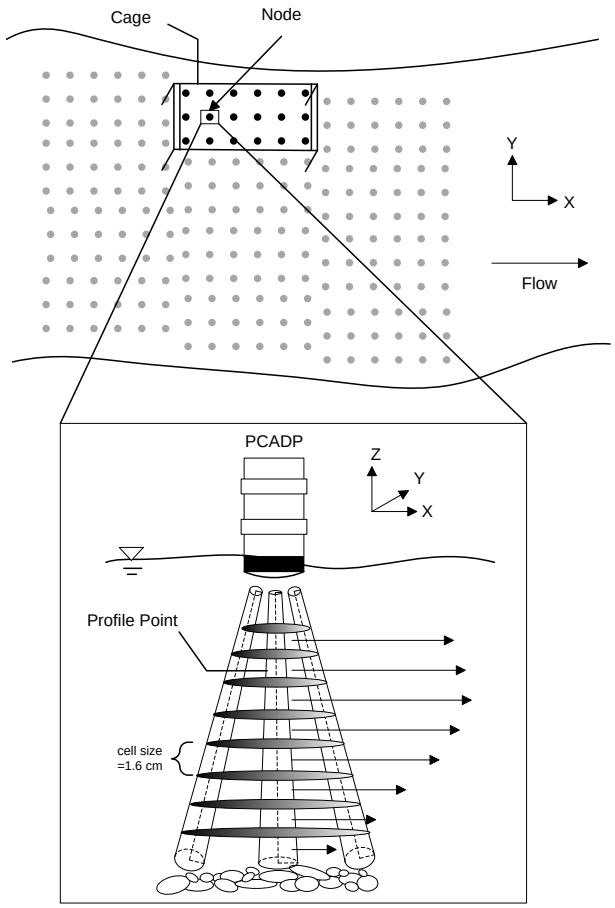

Figure 3.5: Velocity measurement methodology and terminology using a PCADP with the cage and track system

three signal strength values (SNR), and three percent correlation values. The ambiguity resolution routine of the ViewADP software was used to resolve high velocity conditions when a velocity "wrap" may have occurred (SonTek/YSI, 2004). A series of previously developed Visual Basic 6 executables were then used to georeference the data, following the cage methods described in Marchildon (2009). An additional object-oriented program was created to organize and output the data for further statistical and spatial analysis, and to provide a graphical interface for analyzing individual georeferenced profiles (e.g. Figure 3.6).

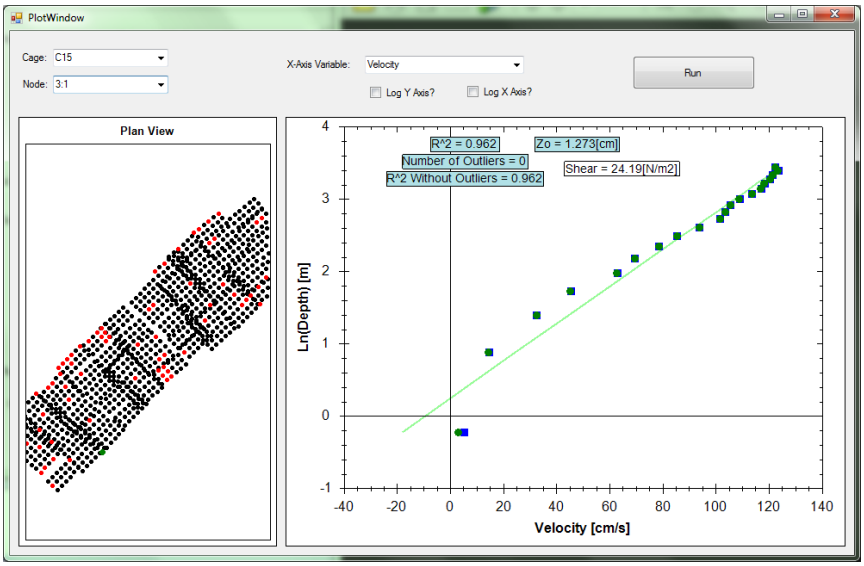

Figure 3.6: Screen capture of post-processing interface developed for velocity profile analysis

3.2.2 Sediment sampling

The barrel sampling technique was used to sample the sediment on all four riffles in August 2010, during base flow conditions (Bunte & Abt, 2001). Samples were collected at the top and bottom of each riffle and the middle if necessary (depending upon observed streambed heterogeneity and riffle length), as well as at the location of any previously identified redds. Grain size analysis was conducted in the laboratory on each sample using the dry sieving method (Bunte & Abt, 2001). The sediment samples were observed to be normally distributed when plotted on a log-normal scale, and the cumulative distribution curve was used to determine additional relevant parameters such as the sorting coefficient (the degree of fluvial dispersion) and skewness. The Inman sorting coefficient (s_I) was calculated using only two percentiles, whereas the Folk and Ward (s_{FW}) coefficient included a broader range of the distribution curve, as defined by:

$$s_I = |\frac{\Phi_{84} - \Phi_{16}}{2}| \tag{3.1}$$

$$s_{FW} = \frac{\Phi_{84} - \Phi_{16}}{4} + \frac{\Phi_{95} - \Phi_5}{6.6} \tag{3.2}$$

respectively. Warrens simplified equation for skewness as a function of median and sorting values is used to categorize the symmetry of the sediment samples, as defined by:

$$sk_{a,W} = \frac{\Phi_{84} - \Phi_{50}}{\Phi_{84} - \Phi_{16}} - \frac{\Phi_{50} - \Phi_{5}}{\Phi_{95} - \Phi_{5}} \tag{3.3}$$

The Fredle index is a measure of the geometric skewness of a substrate sample, and is frequently used to characterise permeability and porosity of spawning gravel (Bunte & Abt, 2001; Lotspeich *et al.*, 1981):

$$sk_{g,F} = \left(\frac{d_{84} d_{16}}{\frac{d_{75}}{d_{25}}} \right)^{05} \tag{3.4}$$

Seasonal monitoring of the streambed surface was accomplished by filtering the PCADP data to determine the elevation of the bed. In addition to velocity, the PCADP records the strength of the backscattered acoustic signal retrieved by the probe that is above the background noise (signal to noise ratio (SNR) in dB). When the ADP pulse hits a boundary, such as the river bed surface, the SNR value will peak as it receives an expectedly strong return signal from the solid boundary. The slant angle of the PCADP transducers is 15° (Figure 3.5). At a 50 cm flow depth and a maximum riffle slope of 1% (R2), an elevation difference of 2.3 mm is expected between beams. Localized changes in elevation can produce a greater discrepancy between the elevations of the peak identified by the beams. Here the maximum difference between any two beams peak elevation was less than 3.2 cm (two cell heights) 75% of the time. The algorithm was therefore further refined to determine the median value of the three bottom depths indicated by each beam.

The changes in bed elevation were iso-contoured according to the average particle size on the study reach. Any changes in bed elevation less than 5 cm may be considered inaccurate given the measurement technique and that the d_{50} value on any riffle never exceeds 5 cm. The priority is to measure significant changes in bed elevation, as opposed to micro changes in topography and particle readjustment. The interpolation necessary to determine the bed elevation between the 80 cm grid spacing also limits the vertical resolution available for topography mapping. Monitoring of the net change of the streambed elevation is useful in estimating erosion and deposition (MacVicar & Roy, 2011), however, the discrete events can result in significant amounts of erosion during peak flow which are re-aggraded during the same event and are not apparent during net change evaluation (Nawa & Frissell, 1993).

Scour chains are steel chains which are implanted vertically into the riverbed during wadeable conditions, and are commonly used to measure the scour and fill of flow events (Emmett & Leopold, 1963). During a peak flow event if the streambed is scoured, the exposed chain will be folded over in the downstream direction, and the scour depth can be recovered by digging through the newly deposited material after the event has passed and

measuring the length of chain which is now parallel to the streambed. In order to measure the discrete scour and fill of sediment, scour chains were implanted in the river bed on R4, the riffle with three established brown trout redds. Four chains were installed in January 2010, two at the top and two at the bottom of R4.

3.3 Post-processing of velocity data

3.3.1 Outlier removal

The PCADP velocity data must be evaluated and filtered prior to calculating flow statistics. Acoustic reflections from the substrate and turbulent decorrelation are common issues with Doppler velocity meters that can lead to erroneous velocity data which should be identified (Lane *et al.*, 1998). When turbulent mixing is strong, decorrelation can occur when the measured particles are redistributed within the cell, resulting in unbiased velocities with low correlations (SonTek/YSI, 2004). Studies have been undertaken to evaluate the accuracy of the PCADP (Gartner & Ganju, 2002; Lacy & Sherwood, 2004; Kobashi, 2009), and the United States Geological Survey has released a post-processing package for filtering and evaluating the raw binary files produced by the PCADP (Martini *et al.*, 2005). However, the majority of these studies are related to either autonomous oceanic or near-shore deployment of the PCADP and are not necessarily applicable in this environment and application.

As discussed in Section 2.2, the law of the wall is commonly used to analyze the coherency of the measured velocity profiles (Stone & Hotchkiss, 2007). The law of the wall can be transformed to the linear domain by obtaining the logarithm of both sides, and a linear regression can be performed by fitting the measured velocity profile points to Equation 2.3. Previous processing of PCADP velocity data in this stationary environmental application found that the removal of up to three points close to the bed greatly improved upon the coefficient of determination in the linear regression of the law of the wall. In order to optimize the regression results and automate the removal of outliers, Cooks distance (D_i) was used to objectively measure the effect of deleting a given observation (Maindonald & Braun, 2007). Data points with large residuals and/or high leverage, quantified by D_i, may distort the accuracy and outcome of the linear regression (Heiberger & Holland, 2004):

$$D_i = \frac{\sum_{j=1}^{n} \left(\hat{U}_j - \hat{U}_{j(i)} \right)^2}{pMSE} \tag{3.5}$$

Where:

$\hat{U}_j$ = predicted velocity from the full regression model for observation j

$\hat{U}_{j(i)}$ = predicted velocity for observation j from a refitted regression model in which observation i has been omitted

p = number of fitted parameters (= 1 for linear model)

MSE = mean squared error of the regression model

Cooks distance for each profile point was determined using Equation 3.5, and all points with a value less than $4/(N+1)$ were discarded, where N is the number of cells in the velocity profile. Deviations from the log profile are occasionally observed as distance from the boundary increases, due to the invalidity of the constant shear stress assumption and mixing length approximations (Julien, 2010). However, 88% of the outliers were identified within 9 cm of the bed, and 67% of the outliers were within 5 cm of the bed, which corresponds well with the reach-wide d_{50} particle size boundary layer. The heterogeneity of roughness elements on the river bed creates localized reductions in near-bed velocities, and can cause deviations from a log profile (Wiberg & Smith, 1987). Figure 3.7 summarizes the distance from the bed surface of the outliers which were removed from each riffle, during each sampling season. A common metric for evaluating the performance and accuracy of

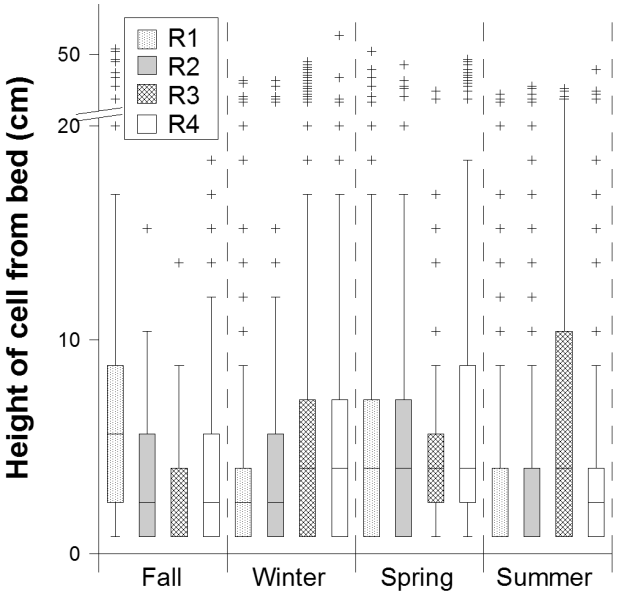

Figure 3.7: Vertical location of outliers removed from velocity profiles following regression analysis

a linear regression is the coefficient of determination (r^2). The accuracy of the parameters

extracted from the log law in Equation 2.3 (such as τ_0) is dependent upon the ability of the linear regression model to reproduce the velocity conditions observed at any distance from the bed. This ability was therefore quantitatively evaluated by examining various critical values for the coefficient of determination. After the outliers identified using Cooks Law were removed and the linear regression was performed again, all nodes with less than 5 valid profile points were discarded. The number of nodes discarded due to insufficient points remained nearly constant through all threshold values of the coefficient of determination. The remaining nodes were discarded because they did not meet the coefficient of determination (r^2) threshold, or regression correlation. At the highest threshold (r^2 =0.99) only 9% of the velocity profiles had a sufficient regression coefficient. Figure 3.8 summarizes the percentage of nodes discarded for both reasons and illustrates that during the fall and winter sampling periods a similar trend for node failure can be identified. However, in the spring

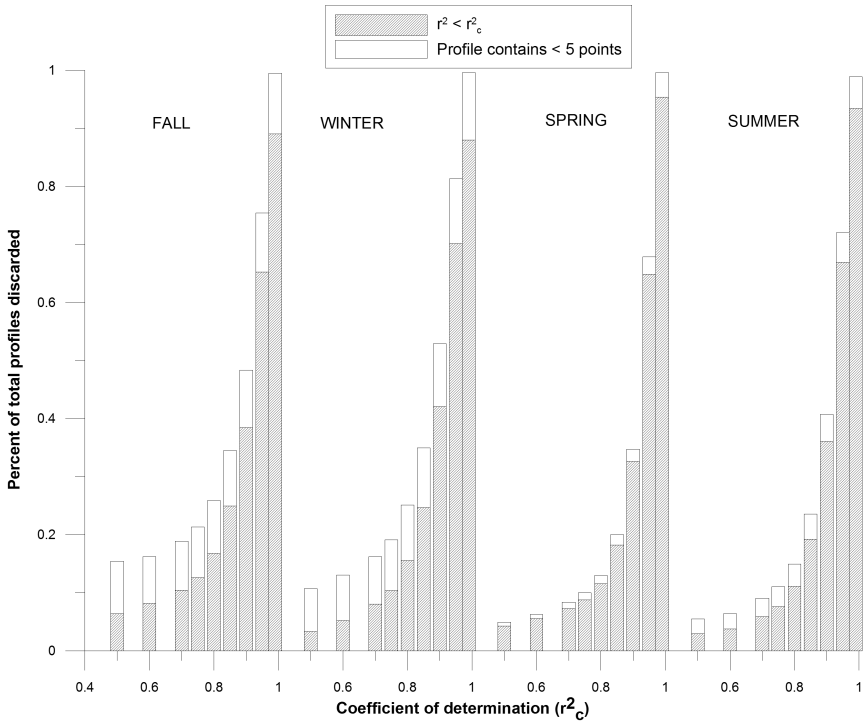

Figure 3.8: Seasonal distribution of discarded regressed velocity profiles at various critical coefficients of determination

and summer a larger proportion of nodes were discarded due to insufficient coefficient of determination and not due to an insufficient number of points in profile. This may be due to higher flow depths in the spring as well as more discretion by those taking measurements in not sampling sections of the riffle with insufficient flow depths. Seasonally and across all riffles, the performance of the PCADP when measuring regressed velocity profiles was

comparable. In addition, the identified outliers did not correlate with low PCADP burst correlation values, indicating that the post-processing using Cook's distance was in fact necessary to successfully identify outliers from the velocity profiles. Following these results, a critical threshold of the coefficient of determination was determined to be optimal at 0.8. Of the over 13 000 velocity profiles measured, 79% were retained following the regression analysis. Further analysis of the regression results indicates that through all seasons, the average coefficient of regression at each riffle was 0.88.

Casado *et al.* (2005) found that regardless of the velocity sampling density employed, the locations of outliers and extreme values remained approximately the same when measuring velocity profiles with an acoustic Doppler velocimeter, and these coincided with the location of unbroken-broken standing waves. Similar problems were encountered in this study, in particular near the right bank of R2. Although use of higher sampling densities in the presence of standing waves can compensate for potential outliers, use of higher sampling densities in selected areas introduces bias and reduces the validity of geostatistical methods which require equal sampling resolutions.

3.4 Hydraulic parameters

3.4.1 Depth-averaged velocity

The application of standard geostatistical methods to the velocity data requires a two dimensional data set, while still preserving a level of variance in the velocity measurements. To resolve the data into two spatial dimensions, a depth-averaged velocity must be adopted (U), obtained by applying the mean value theorem and integrating the law of the wall (Equation 2.3) over the water depth h and assuming $h \gg z_0$, as defined by:

$$U = \frac{u_*}{\kappa} \ln \frac{h}{e z_0} \tag{3.6}$$

The three sensors of the PCADP probe must be submerged while measurement is occurring and 5 cm is required for a blanking distance. Therefore, a portion of the water column at the surface is not captured in the velocity profile. This implies that the arithmetic average of the profile velocities (U_3) is not an accurate representation of the depth-averaged velocity. Several other point-velocity methods exist for estimating depth-averaged velocity: single-point method $0.6h$ from the surface (based on the analytical solution of the integration of the logarithmic velocity profile where the mean is found to be at a depth of $0.37h$), two-point average of $0.2h$ and $0.8h$, and three-point average (mean of $0.2h$ and $0.8h$, and $0.6h$) (Julien, 2010). In addition to these values, the nose depth velocity was defined to be at 10 cm from the bed surface, as discussed in Section 2.2.2. The representative vertical

velocity u_z from the profile was taken to be the vertical component measured at 10 cm above the bed.

A profile-based version of the Reynolds number was calculated using the local flow depth as the characteristic length and the depth-averaged velocity U in Equation 2.1. Similarly, the local Froude number was calculated using the depth-averaged velocity in Equation 2.2 to describe the highly varied relationship between flow depth and velocity at the node scale.

3.4.2 Boundary layer variables

The Prandtl-von Kármán law in Equation 2.3 can be simplified to:

$$u(z) = a + b\ln z \tag{3.7}$$

Where a and b are the intercept and slope of a log-transformed linear regression, as discussed in Section 3.5. Shear velocity u_* was then determined from the following:

$$u_* = \kappa b \tag{3.8}$$

Profile-based local bed shear (τ_0) was calculated for each node following Equation 2.4 from the law of the wall. Local Froude number and Reynolds number were determined using the depth-averaged velocity U and the total flow depth as the characteristic length at each node, as discussed in Section 2.2.

Grain roughness height z_0 was determined from the linear regression of the velocity profile (Equation 2.3), and Nikuradse's local grain roughness was estimated from these values using the relationship in Equation 2.6. Nikora *et al.* (1998)'s version was not considered acceptable due to the resolution of topographic data. As a representation of local surface roughness, k_s represents the size, shape, and distribution of roughness elements on the river bed.

A local estimate of Manning's (n) roughness was derived using the Darcy Weisbach dimensionless friction factor (f) as defined by:

$$f = \frac{8\tau_0}{\rho U^2} \tag{3.9}$$

The Darcy Weisbach resistance factor can be related to the Manning's n resistance in wide shallow channels such as Whiteman's Creek ($R \approx h$) by employing the following conversion:

$$\sqrt{\frac{8g}{f}} = \frac{h^{1/6}}{n} \tag{3.10}$$

Combining Equations 3.9 and 3.10 provides a local estimate of Manning's roughness coefficient at each node:

$$n = \frac{u_* h^{1/6}}{\sqrt{g}U} \tag{3.11}$$

3.5 Statistical methods

3.5.1 Coefficient of variation

The coefficient of variation (CV) is a common method for representing hydraulic diversity, and gives an indication of equitability of a given variable (Kilsby, 2008). By normalizing the standard statistics of a riffle by their respective mean values the relative variance of different spatial or temporal data sets (such as riffles or seasons) can be compared as defined by:

$$CV = \frac{\sigma}{\mu} \tag{3.12}$$

where σ and μ are the mean and standard deviation of a given profile-based hydraulic variable across a single riffle during a single sampling season. Figure 3.9 illustrates a box-and-whisker plot utilized throughout the analysis to represent the coefficient of variation for several variables across several seasons:

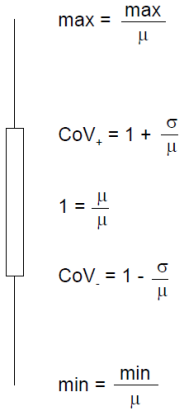

Figure 3.9: Modified box-whisker to represent coefficient of variation (CV) (Marchildon, 2009)

3.5.2 Semivariograms

The primary objective of geostatistical analysis is to characterise and quantify at a riffle scale, through several seasons, the spatial variability (streamwise and transverse) of various hydraulic parameters. A semivariogram approach (Equation 2.11) was employed which required intrinsic stationarity, such that the mean and variance of the parameters difference $(Z(x_i) - Z(x_i + \xi))$ was only dependent upon the displacement between the locations. This implies that the mean of the velocity data may vary spatially, but the semivariogram method will filter this influence (Wackernagel, 1995).

The three main parameters of a semivariogram are the sill, range, and nugget (Figure 3.10). The sill represents the overall variance of the data, and is identified as the maximum value of variance encountered in the semivariogram. The range is the maximum distance over which pairs of observations remain correlated; beyond this distance data behave as if they were independent. A nugget may be identified if the experimental semivariogram does not tend to zero as ξ approaches 0. This discontinuity at the origin may be due to measurement error or fine scale variability not captured at the designated sampling resolution. The presence of a microstructure with a range shorter than the smallest lag increment would also manifest as a nugget in the semivariogram.

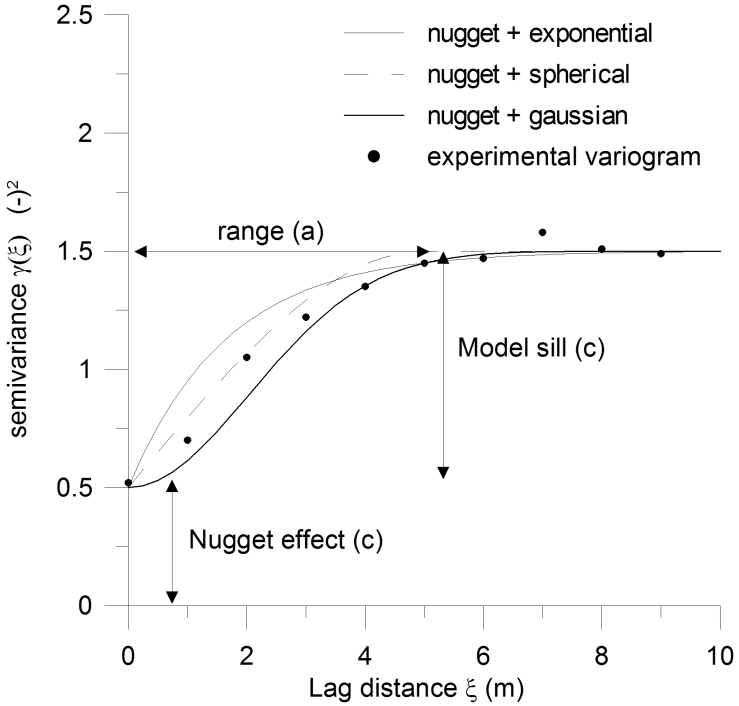

Figure 3.10: Example of experimental semivariogram and applicable parametric models

To account for changes in flow depth during measurement Legleiter *et al.* (2007) and Roy (2006) normalized the velocity and turbulence intensities using a riffle-averaged shear velocity (a measure of "flow strength") prior to a semivariogram analysis. It is also possible to normalize standard variables by the overall sample variance to create a quasi-unit semivariogram to enable comparison between semivariograms of different parameters (Lindsey Smart, 2009). However, the primary advantage of the semivariogram is that it does not require knowledge of the arithmetic mean, which may introduce bias if assumed from the sample data; the use of sample variance is often an inappropriate measure of population variance (Chiles & Delfiner, 1999). Furthermore, converting parameters to relative values may change the interpretation of the semivariogram and may discard biologically relevant information (Clifford *et al.*, 2005).

Semivariogram models are a set of mathematical functions that describe the spatial relationships indicated by the experimental semivariogram. While no model is the perfect fit for a given semivariogram, the Gaussian, exponential, and spherical models are most suitable for data of this nature (Legleiter *et al.*, 2007; Roy, 2006) and are summarized in Equations 3.13, 3.14, and 3.15. The nugget effect (Equation 3.16) is treated as a nested model which contributes to the total sill of a given model, while the Gaussian model exhibits parabolic behaviour at the origin, and represents very smoothly varying properties (Chiles & Delfiner, 1999).

$$\gamma_{\text{sph}}(\xi) = c\left(\frac{3\xi}{2a} - \frac{1}{2}\left(\frac{\xi}{a}\right)^3\right) \tag{3.13}$$

$$\gamma_{\text{exp}}(\xi) = c\left(1 - \exp\left(\frac{-3\xi}{a}\right)\right) \tag{3.14}$$

$$\gamma_{\text{gau}}(\xi) = c\left(1 - \exp\left(\frac{-3\xi^2}{a^2}\right)\right) \tag{3.15}$$

$$\begin{aligned} \gamma_{\text{nug}}(\xi) &= 0 \text{ when } \xi = 0 \\ &= c \text{ when } \xi > 0 \end{aligned} \tag{3.16}$$

Where a and c represent the range and sill, respectively, as illustrated in Figure 3.10. Gaussian and exponential models reach their sill asymptotically, therefore the effective range is the distance at which the semivariogram reaches 95% of its maximum (Wackernagel, 1995). However, the form of the Gaussian model is characterised by smaller spatial velocity gradients (weaker convective accelerations) than an exponential model with similar parameters (Legleiter *et al.*, 2007).

The velocity data collected at Whiteman's Creek was organized into two-dimensional georeferenced node-based local sets, separated by riffle and season. Various hydrodynamic parameters (depth-averaged U, U_{10}, F_r, h, R_e, u_*, τ_0) were calculated for each node, creating a planometric data set of georeferenced data. The third dimension was incorporated into this spatial analysis using semivariograms at the nose-depth. Riffle-scale streamwise and transverse directional semivariograms were calculated and models were fit to the sample semivariograms using Gstat, an open source code for geostatistical modelling and prediction (Pebesma & Wesseling, 1998).

Table 3.1 summarizes the values of the semivariogram parameters used in this study. Only empirical rules of thumb exist for determining the class size of a sample semivariogram. Higher lag increments smooth the semivariogram curve but may compromise smaller scale features, whereas small lag increments may produce erratic experimental semivariograms if there are too few comparisons at each lag (Clifford *et al.*, 2005; Webster & Oliver, 2007). Based upon the sampling interval of 0.8 m and results from previous studies, $\Delta\xi$ =0.5 m was chosen for both streamwise and transverse lag increments. This value is a compromise between providing an adequate number of points in the empirical semivariograms to suggest a suitable theoretical model, while also maintaining a sufficient number of points within each lag class to ensure the accuracy of the semivariogram point.

Table 3.1: Specifications for semivariograms in the (s)treamwise and (t)ransverse directions from literature and study riffles

	Legleiter (2007)		Roy (2006)		Kilsby (2008)		R1		R2		R3		R4	
W(m)	14		15-20		10		15		10		12		14	
L(m)	8		10		125		55		55		25		85	
S_0(m/m)	0.011		0.002		0.0005		0.0075		0.010		0.007		0.006	
	s	t	s	t	s	t	s	t	s	t	s	t	s	t
ξ increment (m)	1.5	0.5	0.25	0.25	0.5	0.5	0.5	0.5	1.5	0.5	1.5	0.5	1.5	0.5
ξ_{max}(m)	6	10	8	8	5	110	26	7	22	6	15	7	45	6
Azimuth tolerance (°)	15	15	15	15	-	-	15	15	15	15	15	15	15	15

The spatial dependencies are not defined in detail at scales smaller than the average minimum distance between the gridded data. Any further investigation must be accomplished by evaluating the nugget effect for evident microscale correlations. Furthermore, the maximum lag distance (ξ_{max}) at which the semivariogram is calculated is typically set at half the maximum distance between sample pairs, which will vary by riffle (Morris, 1991; Deutsch & Journel, 1998). It is likely that pairs at classes higher than this are independent with respect to the spatial scale that the semivariogram is detecting, and will contribute noise to the curve. To create directional semivariograms, two azimuths unique

to each riffle must be specified corresponding to the streamwise and transverse directions. The tolerance of this angle dictates the maximum deviation from the direction tolerated for a pair of points, and defines a cone of searchable area for valid pairs of points to be included in the experimental semivariogram.

Following the development of the experimental semivariogram using the parameters summarized in Table 3.1, appropriate semivariogram models were fit to the curves in order to more concisely describe a standardised spatial structure. The sill, nugget, and range are the quantitative parameters of a semivariogram which can be identified as illustrated in Figure 3.10. While it is possible to determine these parameters by inspection of the experimental semivariograms without the use of a fitted model, scattered data and noise may render the definition of the parameters to be time-consuming. Furthermore, knowledge of the fluid structure can introduce subjectivity and bias into the analysis and manual fitting of parametric models (Chiles & Delfiner, 1999). Gstat was employed using an iterative algorithm to minimize the weighted least squares difference between the fitted model and the sample semivariogram to determine the values of the sill, nugget, and range parameters (Cressie, 1985). Gaussian, spherical, and exponential models were considered, in addition to a nested nugget effect. Visual examination of the model fit was always performed, and in some isolated cases when the parameters from the automated fit were suspect, values determined by inspection were retained instead.

Chapter 4

Riffle hydrodynamics

This chapter serves to present and discuss the results of the riffle-scale velocity measurements, focusing on the high levels of variance observed in numerous features of the riffle environment. Further, this chapter moves from the reach-averaged hydraulic variables to below the sub-riffle scale (Figure 2.1), in order to better define and clarify the heterogeneity and unit-specific geomorphic-biotic relationships (Moir & Pasternack, 2008). The discussion begins at the reach scale with the hydrologic conditions, moves down to the riffle-scale results for various profile-based hydraulic variables, and ends at the local boundary layer where sediment conditions and shear stress describe the seasonally-dependant fluvial responses.

Table 4.1: Morphologic properties of four study riffles at Whiteman's Creek

	S_0 (m/m)	W (m)	L (m)	h_{bf} (m)
R1	0.0075	15	55	1.61
R2	0.0100	10	55	1.67
R3	0.0070	12	25	2.58
R4	0.0060	14	85	1.96

Four riffles within the Apps' Mill Conservation Area concession on Whitemans Creek were included in the study (Figure 4.1). The four riffles (R1, R2, R3, R4) have varying slopes, widths, and lengths, and characterise the common reach-averaged yet varied morphology of the shallow gravel-bed stream outlined in Table 4.1. Width here is defined at low flow conditions when velocity measurements occurred. R1 is located immediately downstream of Robinson Road, and is a straight and heavily armoured steep riffle. R2 is of similar length, however the width contracts mid-riffle to produce two distinct flow regions (wide, shallow and slow; narrow, fast and deep). R3 is located between two sharp meander

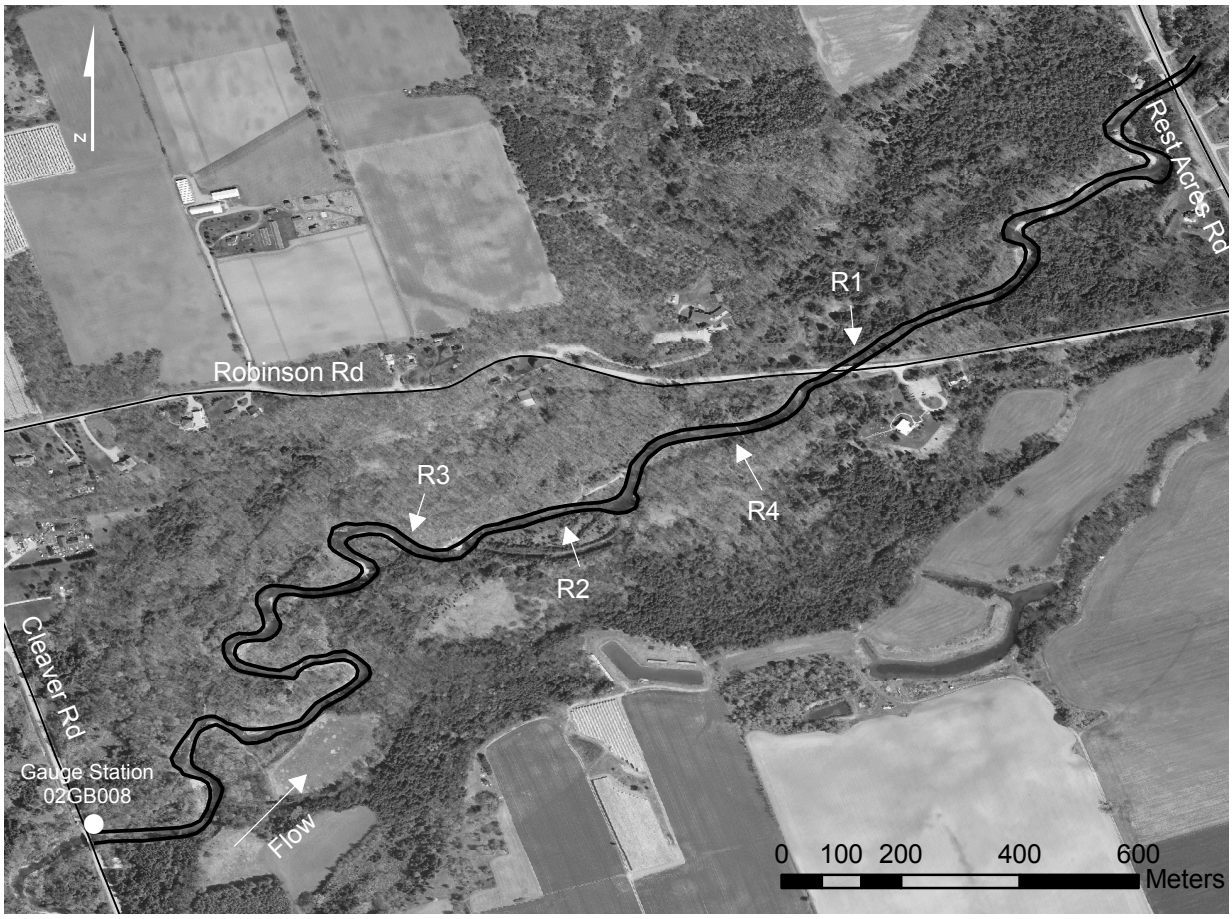

Figure 4.1: Locations of study riffles at Whiteman's Creek

bends, and was observed to be a dynamic structure. R4 is a long, reasonably straight riffle with a constant moderate slope, which is spanned by a pedestrian bridge.

4.1 Hydrologic setting

Bed material samples were used to determine various critical shear stresses on each riffle, following the Shields method described in Chapter 2. Based upon the results for critical shear stress on each riffle, the critical discharges were estimated. A one-dimensional Hydrologic Engineering Centers River Analysis System (HEC-RAS) model was used to determine the approximate discharge at which critical shear stress on each riffle was exceeded for various particle sizes. The critical discharges for the d_{25}, d_{50}, and d_{65} particles are indicated in Figure 4.2 in correspondence with the WSC gauge-measured discharge. The chronology of

field velocity measurements for each riffle are also indicated by the vertical bars. Although R3 had the largest average particle size, the highest critical discharge determined from the model was on R1. Both R1 and R3 have similar bed slopes (see Table 4.1) however the wider cross-sectional geometry on R1 results in lower bed shear stress values for the same discharge. It was observed during velocity measurement that the particle sizes on R3 appear to have increased following the spring flood event. If sediment sampling were to have occurred prior to the spring event, it is expected that the d_{50} value found would have been lower than that collected in August 2010 and it is probable that the Q_{c65} was exceeded during the spring flood.

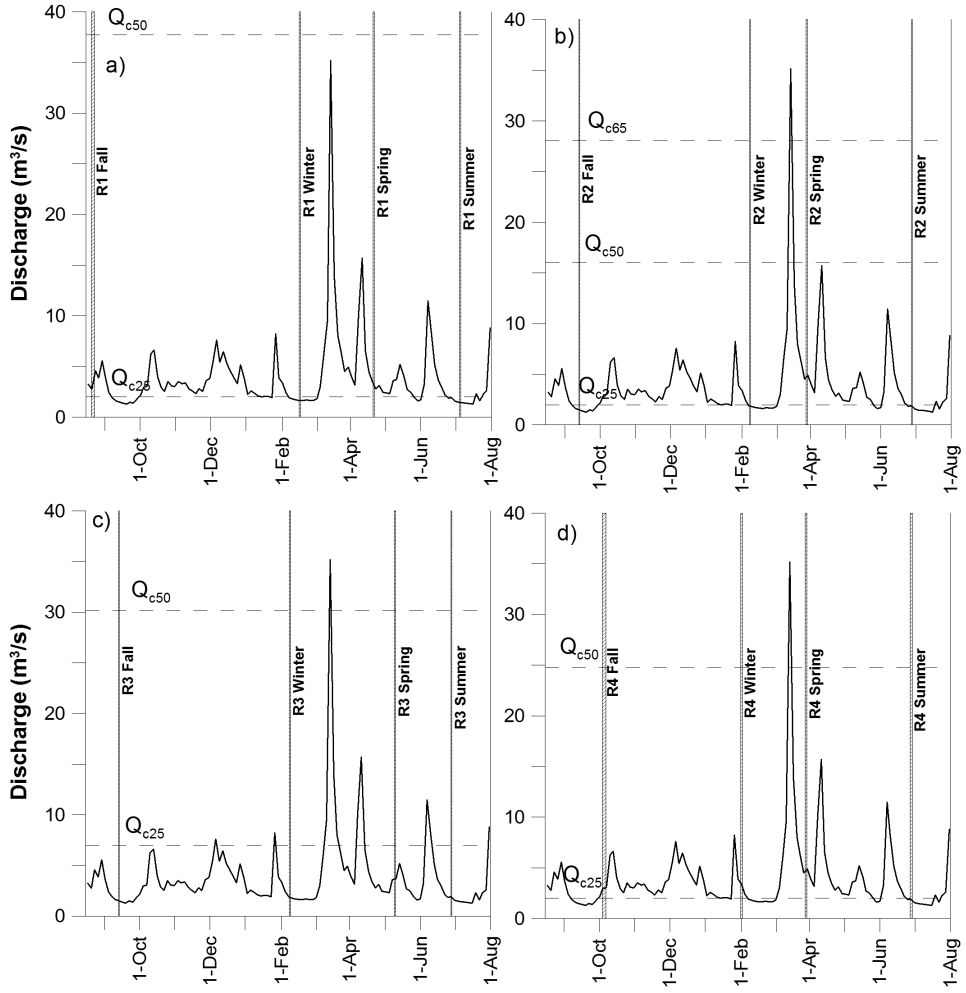

Figure 4.2: Hydrograph (02GB008) and seasonal velocity measurements, with critical discharges (Q_c) of various particles sizes on a)R1 b)R2 c)R3 and d)R4

Two principle hydrological events occurred in the spring of 2010: mid-March and early April. The first event exceeded critical shear stress for d_{50} on all study riffles except R1, as illustrated in Figure 4.2. The peak discharge of the event occurring from March 3 to March 16 with a maximum discharge of 40 m^3/s (uncorrected WSC gauge data), which is also expected to have exceeded the critical shear stress of particles smaller than the d_{65} on all riffles except R1. This discharge also corresponds to the estimated bankfull discharge, determined from field calibration and a Log-Pearson analysis (Lounder & Thompson, 2009). The secondary event, reaching a peak discharge of approximately 25 m^3/s, exceeded critical shear stress of the average particle size of only R2 and R4.

4.2 Riffle-scale results

10 727 vertical velocity profiles were retained for analysis from all sampling periods (R1: 2782, R2: 1978, R3: 1301, R4: 4666). From these profiles, 215 670 three-dimensional velocity measurements were analyzed, at a vertical resolution of 1.6 cm. Prior to the application of standard statistical analysis to the collected velocity data, the Kolmogorov-Smirnov (KS) goodness of fit statistic was used to confirm normal distribution (Chakravarti *et al.*, 1967). The KS test indicated that the depth-averaged streamwise three-dimensional velocity vectors for each reach over the sampling periods were normally distributed ($\alpha = 0.05$). Table 4.2 summarizes the primary hydraulic values for each riffle and season, expressed by the mean (standard deviation).

A one-way analysis of variance (ANOVA) test for equality of all means of riffle and seasonal velocity was performed (Heiberger & Holland, 2004) and the null hypothesis of all means being the same was rejected at a significance of 0.05. A Tukey test was then performed on each pair of means to determine the differences between pairs of seasons (Tukey, 1973). The means were found to be different for all pairs except for fall-winter on R4 and winter-summer on R1. The fall and winter coincide with the typical spawning and incubation period for brown trout. Three redds were identified on this reach during this period. The riffle selected for spawning by salmonids during the study year maintained statistically similar high-resolution velocity conditions through two sampling periods.

Table 4.2: Riffle-scale seasonal mean values (standard deviation) of various hydrodynamic parameters

	R1				R2			
	Fall	Winter	Spring	Summer	Fall	Winter	Spring	Summer
Q (m^3/s)	4.12 (0.28)	1.69 (0.01)	3.05 (0.1)	1.14 (0.07)	1.62 (0.15)	1.92 (0.26)	4.86 (0.1)	1.50 (0.02)
T (°C)	18 - 20	1 - 2	10 - 13	18 - 21	14 - 16	0 - 1	5 - 8	14 - 17
N	733	608	941	500	652	349	572	405
h (cm)	46.3 (12.7)	27.9 (7.1)	39.8 (10.8)	26.3 (5.7)	29.0 (5.8)	30.5 (8.5)	36.9 (8.3)	27.8 (6.1)
U (cm/s)	54.5 (20.4)	48.2 (16.9)	57.4 (19.1)	45.8 (15.3)	46.0 (22.2)	50.6 (20.8)	80.0 (23.1)	56.6 (19.9)
e_a (J/m^2)	11.3 (8.5)	7.0 (6.6)	11.3 (7.0)	5.6 (3.7)	8.6 (9.3)	11.6 (12.7)	24.4 (15.6)	11.1 (9.4)
n ($m^{1/3}/s$)	0.044 (0.010)	0.048 (0.016)	0.045 (0.011)	0.050 (0.014)	0.053 (0.014)	0.053 (0.014)	0.048 (0.011)	0.055 (0.017)
τ_0 (N/m^2)	9.7 (7.7)	12.6 (10.4)	12.6 (9.65)	12.6 (9.6)	15.0 (13.4)	16.5 (12.7)	26.0 (12.3)	20.8 (12.8)
R_e (-)	2.3E5 (1.0E5)	1.2E5 (4.5E4)	1.8E5 (6.5E4)	9.9E4 (3.5E4)	1.1E5 (5.4E4)	1.1E5 (5.5E4)	2.7E5 (1E5)	1.7E5 (7.8E4)
F_r (-)	0.28 (0.10)	0.35 (0.12)	0.33 (0.13)	0.35 (0.13)	0.33 (0.16)	0.35 (0.14)	0.47 (0.11)	0.40 (0.13)

	R3				R4			
	Fall	Winter	Spring	Summer	Fall	Winter	Spring	Summer
Q (m^3/s)	1.35 (0.02)	1.83 (0.01)	4.16 (0.05)	1.90 (0.07)	2.81 (0.24)	2.75 (0.39)	4.21 (0.35)	1.68 (0.12)
T (°C)	14 -16	0 - 1	8 - 10	17 - 20	6 - 9	0 - 1	6 - 9	16 - 20
N	436	295	292	278	954	1176	1406	1130
h (cm)	29.1 (8.1)	30.0 (8.7)	47.0 (8.3)	31.5 (7.4)	35.1 (11.5)	37.6 (13.7)	45.4 (10.9)	33.8 (8.9)
U (cm/s)	36.6 (16.0)	41.5 (18.8)	65.0 (17.9)	50.8 (17.5)	54.5 (15.1)	54.2 (15.2)	74.0 (17.9)	50.0 (12.3)
e_a (J/m^2)	4.75 (4.06)	6.4 (7.2)	18.0 (12.0)	8.8 (6.0)	10.8 (7.8)	10.7 (8.2)	21.2 (13.4)	8.5 (4.9)
n ($m^{1/3}/s$)	0.051 (0.016)	0.047 (0.012)	0.047 (0.011)	0.049 (0.013)	0.052 (0.015)	0.048 (0.011)	0.045 (0.01)	0.050 (0.013)
τ_0 (N/m^2)	8.7 (8.1)	9.8 (9.9)	15.1 (10.4)	14.0 (11.4)	16.0 (10.9)	13.5 (9.6)	17.5 (9.6)	12.2 (7.8)
R_e (-)	1.1E5 (6.1E4)	8.8E4 (4.8E4)	2.3E5 (6.7E4)	1.7E5 (6.5E4)	1.5E5 (6.1E4)	1.3E5 (4.9E4)	2.2E5 (7.3E4)	1.8E5 (5.8E4)
F_r (-)	0.26 (0.11)	0.29 (0.13)	0.33 (0.1)	0.34 (0.13)	0.35 (0.11)	0.34 (0.12)	0.38 (0.09)	0.32 (0.09)

4.2.1 Discharge and flow depth

The relationship between the reach-averaged discharge Q during velocity measurement and the flow depths h of sampled locations is illustrated in Figure 4.3. The dashed line between winter and spring indicates the occurrence of a bed-mobilizing event for particles smaller than d_{50}. A one-way ANOVA test performed on the flow depths showed a significant difference between all seasons on each riffle. An ANOVA performed on the discharge found that all discharges during sampling were also not equal ($\alpha = 0.05$, similar to Legleiter *et al.* (2007). This implies that 16 independent data sets of velocity were collected, and each set is discharge controlled. The effect of the discharge control varies as a function of both time (seasonal) and space (intra- and inter-riffle).

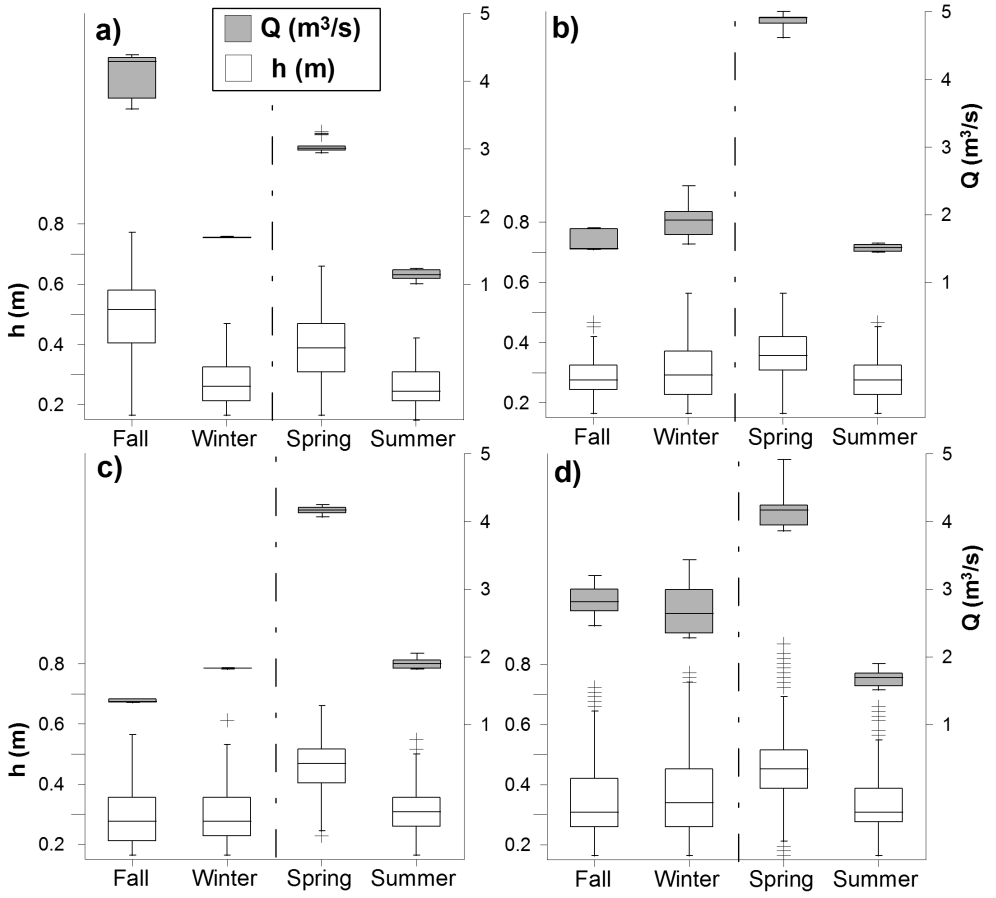

Figure 4.3: Seasonal sampled flow depths h and gauge-measured discharge Q on a) R1 b) R2 c) R3 and d) R4

With the exception of R1, the highest flow depths on each riffle were measured during the spring sampling season. Of particular interest are the spring flow depths on R2 and R3: following the mobilizing flood event where the hydrodynamic response of each riffle to the higher spring sampling discharges can be observed. In the case of R2, the average spring sampling discharge is over 150% greater than the average during the other seasons. The sampled flow depths, however, did not increase as significantly ($\approx$25%).The hydraulic relationship identified in the fall and winter does not appear to persist following the bed mobilizing event in the spring, most likely due to some change in the hydraulic geometry or roughness. In the case of R3, the sampled flow depths in the spring were only slightly higher than those of the other seasons, despite the gauge-indicated discharge being over 2 m^3/s higher than the discharge during the other sampling seasons. Similarly, when com-

paring the fall and summer sampling seasons on R3, it can be observed that although the discharge during sampling was higher in the summer, the sampled flow depths were similar. This potential change in hydraulic response of the riffle is attributed to the spring mobilizing event, which significantly altered the morphology and channel geometry on R3. The hydraulic geometry relationship of flow depth to discharge is evidenced to be temporally variable, and seasonal variability of sampling discharge created varying responses in measured flow depths in this study.

4.2.2 Statistical variance

Figure 4.4 illustrates the coefficient of variation for several relevant hydraulic variables. The ANOVA test determined that the means of the seasonal velocity, discharge, shear data on each riffle were statistically different, therefore the CV provides a unit-less approach to comparing the relative variability both seasonally and inter-riffle, such as that evaluated by Marchildon (2009). The maximum, minimum, and standard deviation (σ) of several relevant hydraulic metrics on each riffle were normalized using the mean, and modified box-and-whisker plots were created following the format in Figure 3.9. For all metrics except turbulence, the coefficient of variation is less than 1 which implies that the standard deviation is not significantly larger than the sample mean. A higher CV identifies a more diverse hydraulic environment (Kilsby, 2008). A higher flow depth is normally associated with lower hydraulic diversity, or lower variance. Changes in velocity and other hydraulic metrics between seasons may be due to either changes in bed form (hydraulic geometry, roughness, scour and deposition) or changes in observed discharge during sampling, as mentioned previously. The average flow depth during the fall sampling period on R1 was over 10 cm (40%) higher than during the three other sampling seasons, however the CV of all metrics remains relatively constant through all seasons. Changes in hydraulic geometry or bed form are not likely to have occurred between fall and winter on R1 (Q_{c50} not exceeded), therefore, any changes could be attributed to the difference in discharge during sampling ($h = f(Q)$). However, the CV does not significantly change despite the statistical differences in discharge between the fall and other seasons. Therefore, changes in sampling discharge did not affect the majority of variance on R1. Only e_a exhibits an expected higher variation during the lower winter discharges.

A higher seasonal variability of the CV can be identified on R2 and R3, with the highest variance observed during fall and winter. Fall and winter had the lowest flow depths of all seasons on these riffles. The lower variance associated with higher flow depths were observed during the spring on both riffles. The spatial structures of turbulence (e_a) on R2 and R3 are seemingly affected between the levels of discharge variability observed between seasons, given that the CV is higher during the lower depths of fall and winter, and lower variance is observed during the higher depth of spring. The roughness parameters (n and k_s) derived

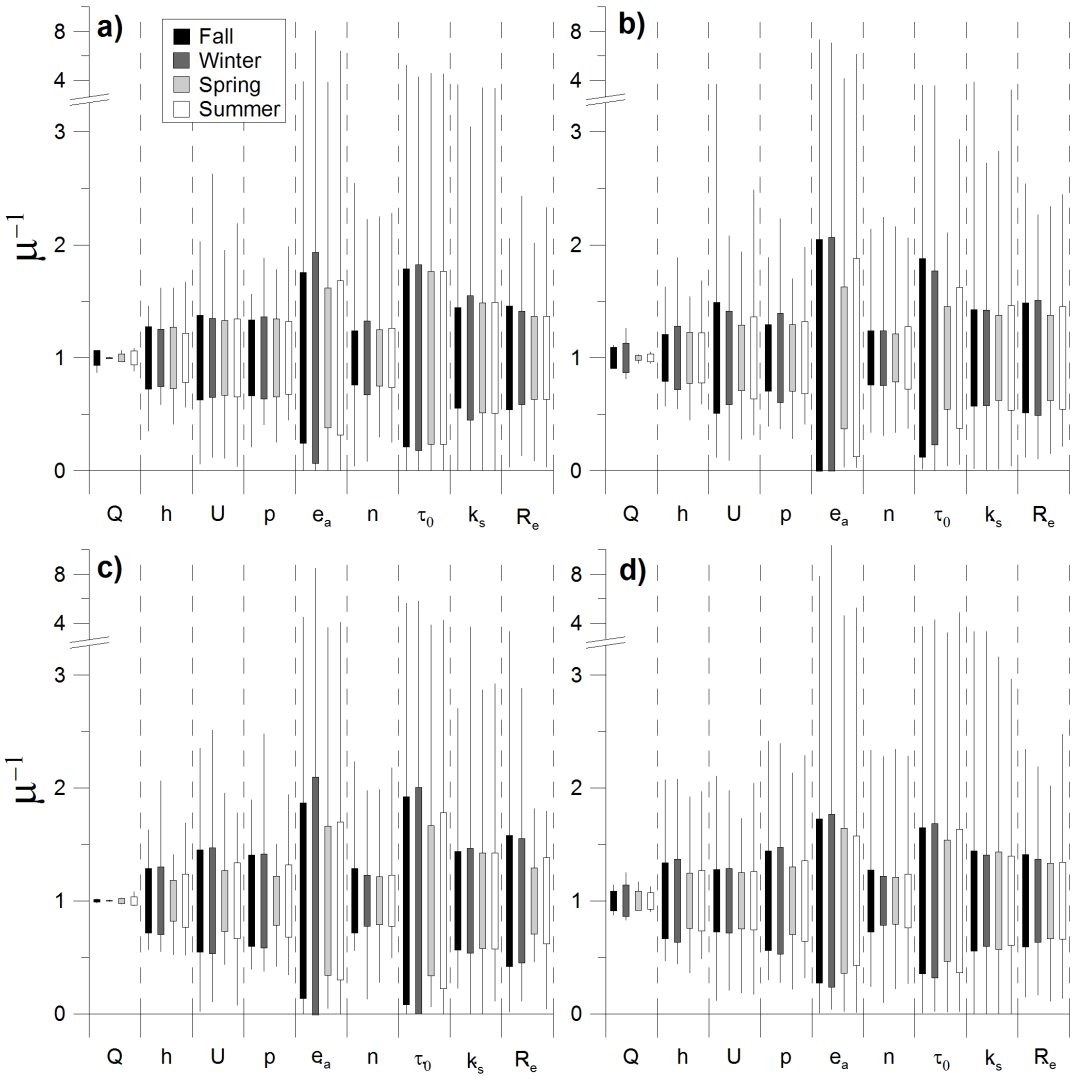

Figure 4.4: Coefficient of variation box-whisker plots for various hydraulic parameters on a) R1 b) R2 c) R3 and d) R4

from the velocity profile indicate different levels of variance. The grain roughness height (k_s) shows greater variance overall, however exhibits the same patterns in seasonal variability as Mannings roughness coefficient.

The spatial complexity of the flow field becomes apparent when interpreting the range in the CV of profile-averaged turbulent kinetic energy (e_a). The large variability of e_a indicates the possibility that a three-dimensional turbulent flow structure is maintained

on all riffles for all seasons. In particular, the variance of e_a during the winter sampling is higher than all other parameters for all riffles, and greater than 1 for all riffles except R4. The winter variance could be explained when considering the presence of anchor ice, which was observed during the winter sampling on all riffles. Anchor ice raises the effective channel bed elevation, and alters the bottom roughness. Although a significant overall increase in bed elevation was not observed, Kerr *et al.* (2002) found that the hydraulic resistance of anchor ice was reduced for smaller particle sizes, and that the resistance also decreases with increases in flow rate. The higher hydraulic resistance over greater particles means that the roughest sections of the riffle were even rougher in the winter due to anchor ice. The higher variance in e_a during winter could be attributed to this increase in apparent roughness.

4.3 Boundary layer and substrate characteristics

This section will follow the scale-specific approach to variance by linking the previously discussed profile-averaged characteristics to boundary layer information such as substrate, local bed shear and roughness, and riffle-scale erosion and sedimentation.

4.3.1 Sediment analysis

Table 4.3: Substrate particle sizes (mm) for each riffle

	d_5	d_{16}	d_{25}	d_{50}	d_{65}	d_{75}	d_{84}	d_{90}	d_{95}
R1	0.5	3.0	8.6	39.8	62.1	82.4	111.1	134.2	144.8
R2	0.6	4.1	10.7	32.8	46.3	53.7	67.2	75.7	85.4
R3	0.6	5.7	18.3	48.0	62.5	83.0	114.6	125.3	142.8
R4	0.5	2.9	8.4	32.0	54.5	64.9	79.0	85.4	93.2

Table 4.3 summarizes the sediment data collected in August 2010 on the four riffles studied at Whitemans Creek. Top, middle, and bottom of riffle samples were averaged to determine a representative particle size for each riffle. R3 has the largest average particle size of all riffles, for both the top and bottom of the riffle samples. This does not correspond with the highest slope, which was identified on R2. As expected, the substrate samples indicated grain size distributions skewed to larger particles on the top of each riffle compared to the downstream end.

In comparison with previous substrate particle sampling done on riffles at Whitemans Creek, the results produce a similar sediment size distribution and average particle sizes

(Marchildon, 2009; Hartley, 1999). The d_5, d_{16}, and d_{25} values were slightly lower ($\approx$15%) for this study, indicating a greater amount of sand in the substrate of the riffles selected for this study. This could be due to the fact that the sediment sampling was undertaken during low summer discharges, when deposition of fines within interstitial spaces is more pronounced than during the higher autumn discharges which occurred during and prior to when the previous sediment sampling was undertaken.

The sorting coefficients of both Inmans and Folk and Ward produced similar results, and characterise the sediment as being poor to very poorly sorted. The sorting coefficients calculated in this study are greater than those previously found at this site. Again, this is most likely due to the higher amount of fine sediments found in the most recent sediment sampling, given that the remaining particle distributions and fractions are similar. The Warren skewness calculation found that the sediment samples of all riffles were negatively skewed, toward the finer particles. The presence of these sands and finer particle fractions can be attributed to the creek's path upstream of the study reach through the shallow sandy aquifer of the Norfolk Sand Plain (Ontario Geological Survey, 2007).

4.3.2 Seasonal deposition and erosion

Between fall and winter sampling periods, critical shear stress of the average particle size was not exceeded on any riffle. Between winter and spring sampling, bed movement is expected to have occurred as a result of two flood events exceeding critical shear stress of particles smaller than d_{50} (see Figure 4.1). Figure 4.5 illustrates the measured change in bed elevation between these two sampling periods for each riffle. In the sampled region of R3, both net erosion and deposition occurred during the spring events. The most significant change was the formation of a mid-bar which raised the bed over 10 cm. R1, however, did not exhibit the same dynamic bed morphology. As indicated by the HEC-RAS model, the bed shear occurring on R1 during flood flow was insufficient to exceed critical shear stress of particles greater than d_{50}. Fewer than 10 sampling nodes indicated erosion or deposition greater than 5 cm. From field observations and bed elevation measurements, R1 appears to be more resistant to change, which may be attributed to the straighter reach and larger armour layer, despite having the highest gradient.

When compared with the changes between the other sampling seasons, R3 experienced the greatest morphological adjustments during the two spring events, as expected based on flow conditions and exceedance of critical shear stress. In fact, post freshet field observations at R3 led to the abandonment of the riffle for sampling due to the significant change in bed structure and flow conditions. After April 2010, the R3 structure became dominated by a bend, and only limited areas of typical riffle flow patterns could be visually identified. A slight increase in overall gradient on R3 was identified, primarily due to the deposition in the middle of the channel near the top of the riffle. R3 was only continued in the sampling

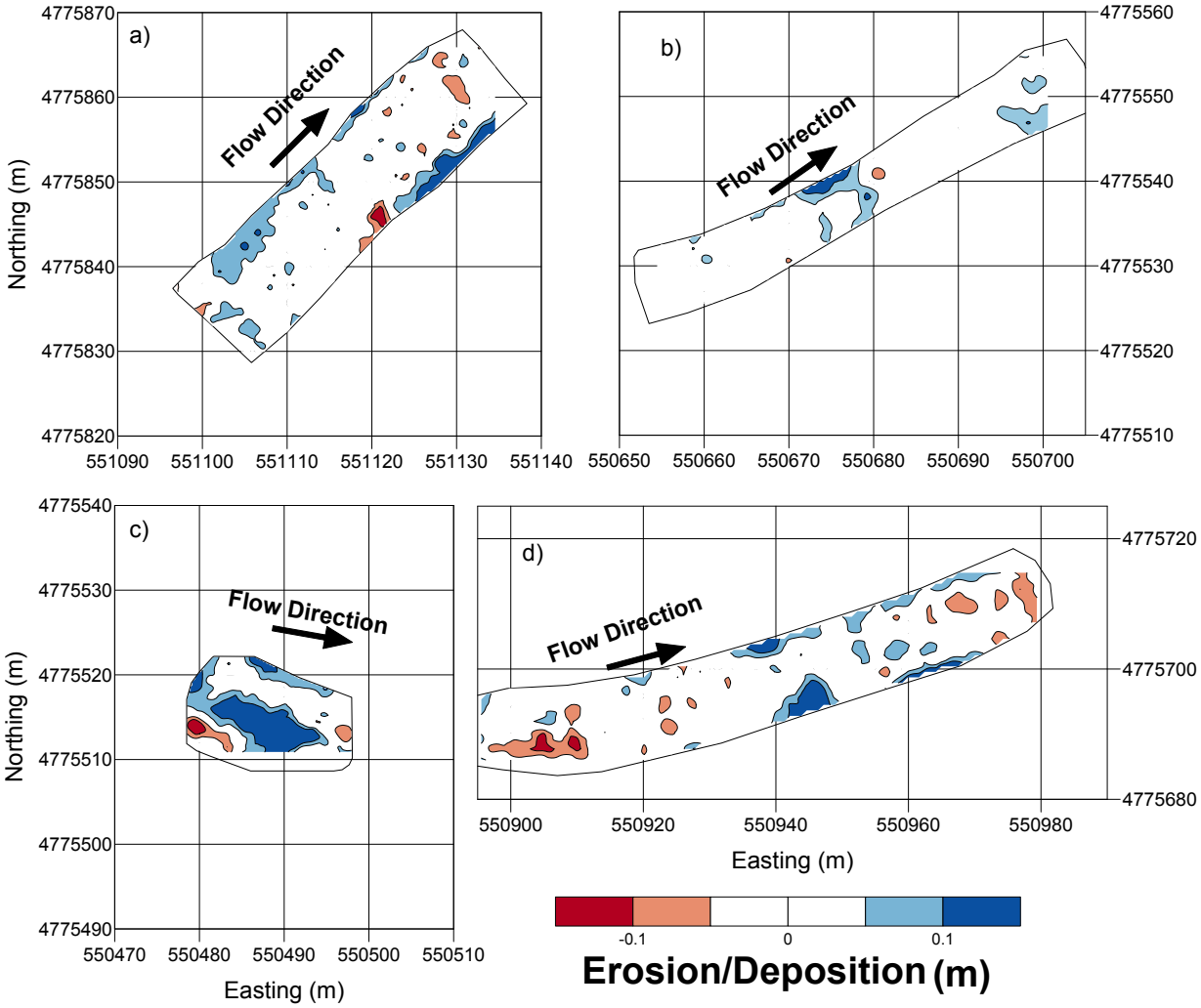

Figure 4.5: Changes in bed elevation (m) between winter and spring sampling on a) R1 b) R2 c) R3 and d) R4

process in May 2010 when a rainbow trout redd was identified near the right bank. In addition to vertical instability, Rosgen & Silvey (1996)'s indice for near-bank shear stress suggests that R3 is at extreme risk for bank erosion, whereas the remaining riffles are at a very low risk (Lounder & Thompson, 2009). A high level of near-bank shear stress intensifies erosion on the outer bank and deposition on the point bar. The characteristic was confirmed by the presence of a depositional mid-bar on R3 following the spring flood event, seen in Figure 4.5. It should also be noted that sediment sampling occurred after the spring event, and may not reflect the substrate conditions on R3 during fall and winter sampling periods.

During the largest flood event (between Winter-Spring), R2 did not experience erosion or sedimentation greater than 5 cm, while R4 generally experienced erosion at the top and bottom of the riffle, and deposition on the banks, as illustrated in Figure 4.5. The bed surface changes between the Spring and Summer sampling, the period during which the secondary event occurred, are not significant, with only minimal patches of deposition in the centre of the channel and erosion near the banks. The scour chains installed on R4 and recovered in the summer of 2010 indicated scour depths of approximately 5 cm on the top of R4 and 8 cm on the bottom of the riffle.

The critical shear values illustrated in Figure 4.2 describe the dynamic abiotic characteristics of a typical riffle in a gravel-bed stream, however these observations also relate to the biotic communities on these morphological units. Successful salmonid reproduction depends in part on egg burial depths exceeding the depth of scour during the incubation period (Montgomery *et al.*, 1996). The bed-mobilizing event which most likely created the erosion observed in Figure 4.5 was in late March 2010, when the water temperature had only risen above 5 °C for several days. It is not likely that the brown trout had emerged from the substrate at this time. Developing a field-based relationship between bed scour depths, shear, and discharge is a useful tool in predicting reproduction success. Data on egg burial depths of brown trout vary widely and are inconsistent (DeVries, 1997), however Witzel & MacCrimmon (1983) reported general burial depths greater than 13 cm in southern Ontario streams. Crisp & Carling (1989)'s results from regressions of redd dimensions, female body length and burial depths of freeze-core recovered salmonid eggs confirms this value as being between 10-15 cm for the redds discovered at Whiteman's Creek. This implies that even during a morphological modifying discharge event at Whiteman's Creek, the bed scour on R4 did not exceed a typical burial depth for salmonid redds.

4.3.3 Surface roughness characteristics

Depth and velocity are functions of roughness, which is partly a function of channel geometry, which is in turn a function of depth and velocity (Richards, 1973). The complexity of the linkage between roughness and discharge and flow depth and velocity is highlighted by investigating the seasonal variations in roughness estimates.

The Nikuradse grain roughness height (k_s) at each node was calculated from the values of roughness length (z_0) derived from the logarithmic profile regressions. An ANOVA test on each riffle's local k_s values found that the means were not the same throughout the year on all riffles except R2. These roughness values were averaged by section of riffle (Top, Middle, Bottom) and compared with the empirical estimates of k_s. Of the four most common empirical estimates for k_s as a function of particle diameter, $5.2d_{65}$ was the best approximation of the regionally-averaged node roughness values. Figure 4.6 illustrates the variance of the velocity profile-derived roughness results compared to this empirical

riffle-scale estimate. $6.8d_{50}$ was the least similar estimate of roughness on all riffles, and consistently underestimated the roughness values, both at the top and bottom of riffles. The substrate-based riffle-scale estimate of roughness on R2 is significantly lower than the profile-derived roughness. As mentioned at the beginning of Chapter 4, R2 has two distinct flow regions. The true heterogeneity of the substrate sediment may not be reflected in these empirical estimates due to difficulties sampling in the narrow, fast, and deep sections.

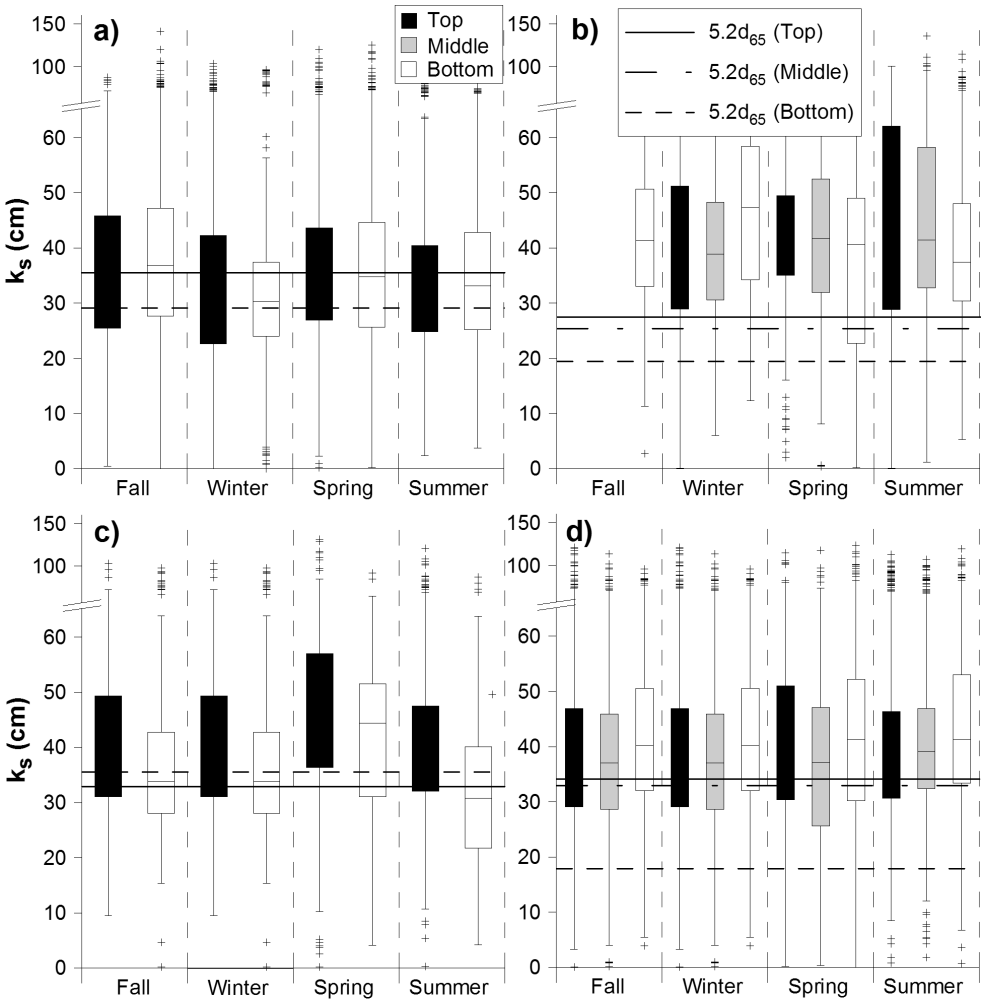

Figure 4.6: Grain roughness heights on the top, middle and bottom of a) R1 b) R2 c) R3 and d) R4

The trend of decreasing roughness from top to bottom of riffles is observed, and the empirical estimates confirm this. However the change in roughness from top to bottom of riffle determined from the velocity profiles is not as significant as that indicated by the

empirical estimates. The estimates of roughness determined from the substrate samples indicate a greater range in roughness from the top to the bottom of the riffle and the velocity profiles indicate more homogeneous roughness conditions on the riffles.

The mean roughness on R3 increased between the winter and spring, despite little to no change in discharge at these samplings periods. This may be due to the removal of fine particles during the primary mobilizing event which occurred between these samples, and coarsened the sediment matrix of the bed. As previously mentioned in Section 4.1, it was observed that the particle sizes appear to have increased on R3 following the spring flood event, which would correspond with the increase in boundary roughness as the re-deposition of coarser bed materials on R3 would create higher roughness. The subsequent decrease in roughness observed in the summer could be related to re-depositing of fines following two smaller but significant discharge events.

4.3.4 Bed shear stress

Figure 4.7 illustrates the estimated shear stress at each riffle during the sampling year. The highest bed slope was identified on R2, which also experienced the highest bed shear of all riffles. Table 4.2 also indicates R2 experienced the highest bed shear stress of all other riffles and seasons during the spring sampling period specifically. The highest sampling discharge on R2 also occurred during the spring, however, the average flow depth was only 7 cm (25%) higher than during the other measurement periods on R2. A possible explanation for this seemingly uncharacteristic hydraulic response may be the presence of a large tree ($d = 0.4$ m) which was lying across the downstream end of the riffle, creating a backwater effect. The impact of large woody debris such as this on the hydraulic characteristics of the channel is the creation of a geomorphic subunit. This subunit, at the downstream end of the riffle in this case, is usually characterised by an increase in the upstream flow depth, a decrease in velocity and subsequently shear stress, and potentially the deposition of sediment (Gurnell *et al.*, 1995). The tree on R2 remained across the riffle until the spring freshet event, prior to the spring sampling. The tree was carried downstream, presumably during this flood event, and the flow conditions immediately upstream were altered once the impeding structure was removed. A comparison of the spatial distribution of shear stress on R2 in Figure 4.8 indicates that following the spring flood bed shear increased in the downstream section of riffle. A slightly elevated shear stress in this region was also observed in the summer season. However, the results of the bed elevation measurements for R2 between winter and spring indicate over 5 cm of deposition in the region immediately upstream of the location of the tree.

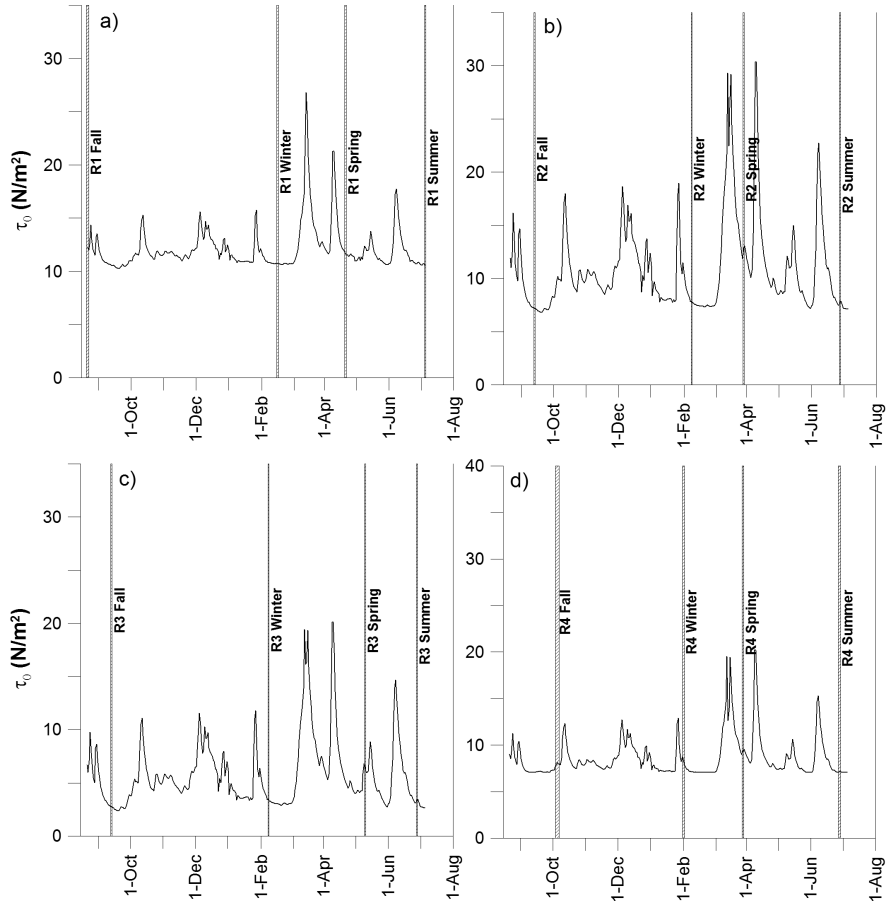

Figure 4.7: Bed shear stress τ_0 from HEC-RAS model during entire sampling year on a) R1 b) R2 c) R3 and d) R4

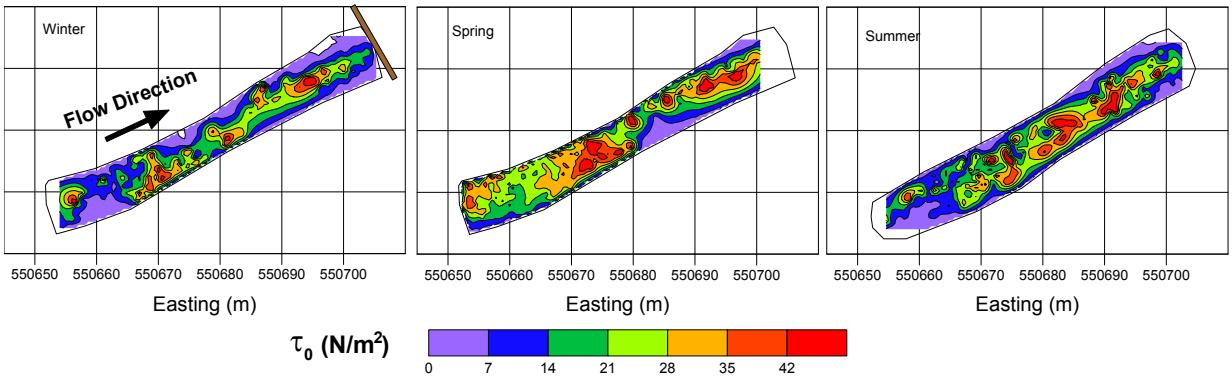

Figure 4.8: Bed shear stress τ_0 on R2 derived from velocity profiles during winter, spring, and summer measurement periods

4.4 Spatial characterisation

Directional experimental semivariograms of several fundamental hydraulic quantities were generated for each riffle and for each sampling season. Figure 4.9 illustrates the number of pairs of points found in the range of lag distances, at increments of 0.5 m. Standard practice for building experimental semivariograms is to ensure that more than 30 pairs are available at each lag distance, and the distance of reliability (maximum lag distance) is half the maximum distance over the field of data (Journel & Huijbregts, 1978). Table 3.1 summarizes the semivariogram parameters selected for this study. As expected, the maximum transverse distance is significantly lower than the maximum streamwise distance, and ranges between 7 m to 14 m depending upon the width of the channel. Although the range of the streamwise data is greater than the transverse, when inspected within the same lag distance the number of pairs are similar in both directions, and the number is significantly greater than the minimum threshold of 30 points. The number of pairs separated by a given distance may be used as a comparative index of the precision which can be expected from each data set, however, the precision is also dependent upon the correlations (Morris, 1991). The integrity of the comparison of the semivariograms derived from datasets of varying pairwise distance distributions is not considered compromised due to the high number and relative similarity of the number of pairs.

The automated fitting of semivariogram models involves a considerable amount of observation and discretion on the part of the interpreter. Several cases of modelling uncertainty were identified during this process. The most common was the presence of a "pure nugget" effect. The fitting algorithm would often associate this type of empirical semivariogram with a very long range. In the case where the range is not distinguishable, and a nugget effect is assumed, it may be an indicator that the sampling density is insufficient to capture the spatial variability of the flow structure (Legleiter *et al.*, 2007). Similarly, several experimental semivariograms with increasing variance as a function of distance were identified when the algorithm was unable to define the semivariograms parameters, indicating a linear model. An unbounded semivariogram increases indefinitely with increasing lag distance, indicating that covariance does not exist (Webster & Oliver, 2007). In both of these cases, the model parameters were rejected and the semivariograms were not included for comparison. For cases where the models were rejected, it can be interpreted that the spatial structure of the characteristic flow variable is poorly defined within the lag distances (Legleiter *et al.*, 2007). At large lag distances, beyond the measured scale of the perceived flow structure, harmonic effects can be observed. The automated fitting of the models attempts to accommodate for this harmonic behaviour and ensure a valid fit is achieved without bias.

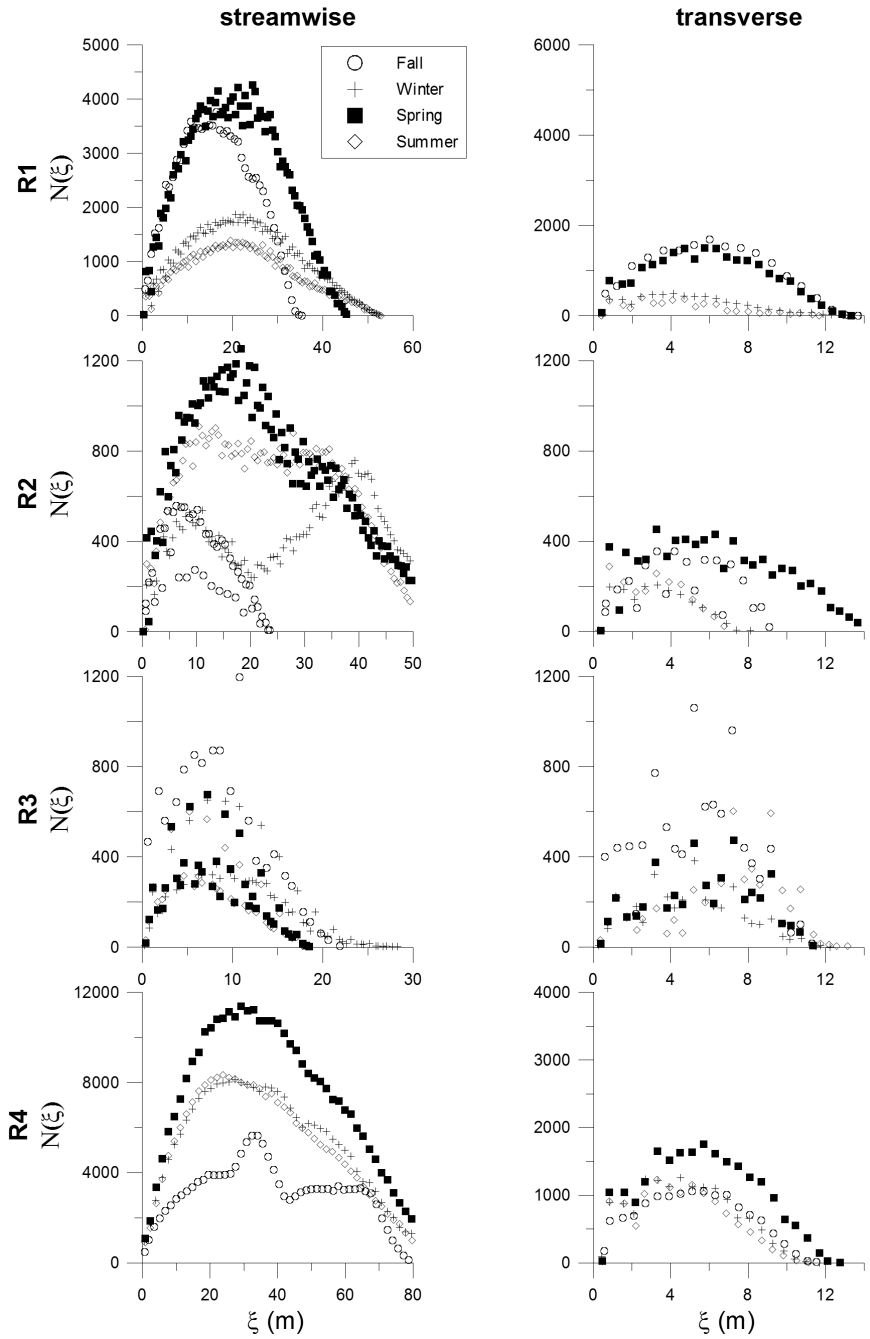

Figure 4.9: Number of data pairs at varying lag distances in the streamwise and transverse directions

4.4.1 Depth-averaged velocity semivariograms

Figure 4.10 contains the directional semivariograms of depth-averaged velocity for all riffles through all seasons. The ranges of the transverse semivariograms are similar for all riffles, and vary between 1.9 - 5.9 m. In the streamwise direction the range of spatial dependence varies more broadly, between 7.7 m to 17.6 m. It was not possible to fit models for several of the streamwise semivariograms, and some fitted semivariograms indicated the presence of secondary sills. The streamwise experimental semivariogram for the spring season at R1, for example, reveals a nested structure which is characterised by a second longer range. This hierarchical structure can be identified by the presence of the secondary sill, located at approximately 30 m. The initial sill is identified at 17.6 m and is within 5% of other magnitudes for R1, indicating that this sill is describing the same spatial pattern as the other semivariograms in this set. The secondary sill, however, is a result of some larger scale spatial structure in the velocity data, or the presence of processes operating at different scales (Armstrong, 1998). The streamwise velocity semivariograms for R4 also indicate this behaviour, as the fall and spring data only revealed a secondary sill present at over 30 m. Nested variation in semivariograms is a result of physical processes operating and interacting at different spatial scales, and this spatial variation can occur on scales that differ by several orders of magnitude simultaneously (Webster & Oliver, 2007).

The ranges of the streamwise semivariograms were consistently two to three times greater than the ranges of their respective transverse semivariograms. Although the resolution of measurement was the same for both directions, the spatial pattern observed using semivariograms was not. The streamwise ranges are all greater than the transverse ranges because the transverse bathymetric range is mostly related to microtopography, which does not dominate the flow structure on scales as high as bathymetric changes such as the streamwise slope at Whiteman's Creek. As more and better data become available, the range of the semivariogram tends to increase (Goovaerts, 1997).

The magnitude of velocity semivariance is consistently higher (10-50%) in the transverse direction, indicating a less smooth spatial structure. R2 consistently has the highest sills during all sampling seasons in both directions. In addition to having the highest mean velocities of all riffles for all seasons except during the fall, the flow structure on R2 is asymmetric, with only a 2 m wide strip of high velocities (often higher than 90 cm/s) along the right bank (See Appendix). It appears the higher velocities and partitioned flow structure on R2 produced higher relative semivariance.

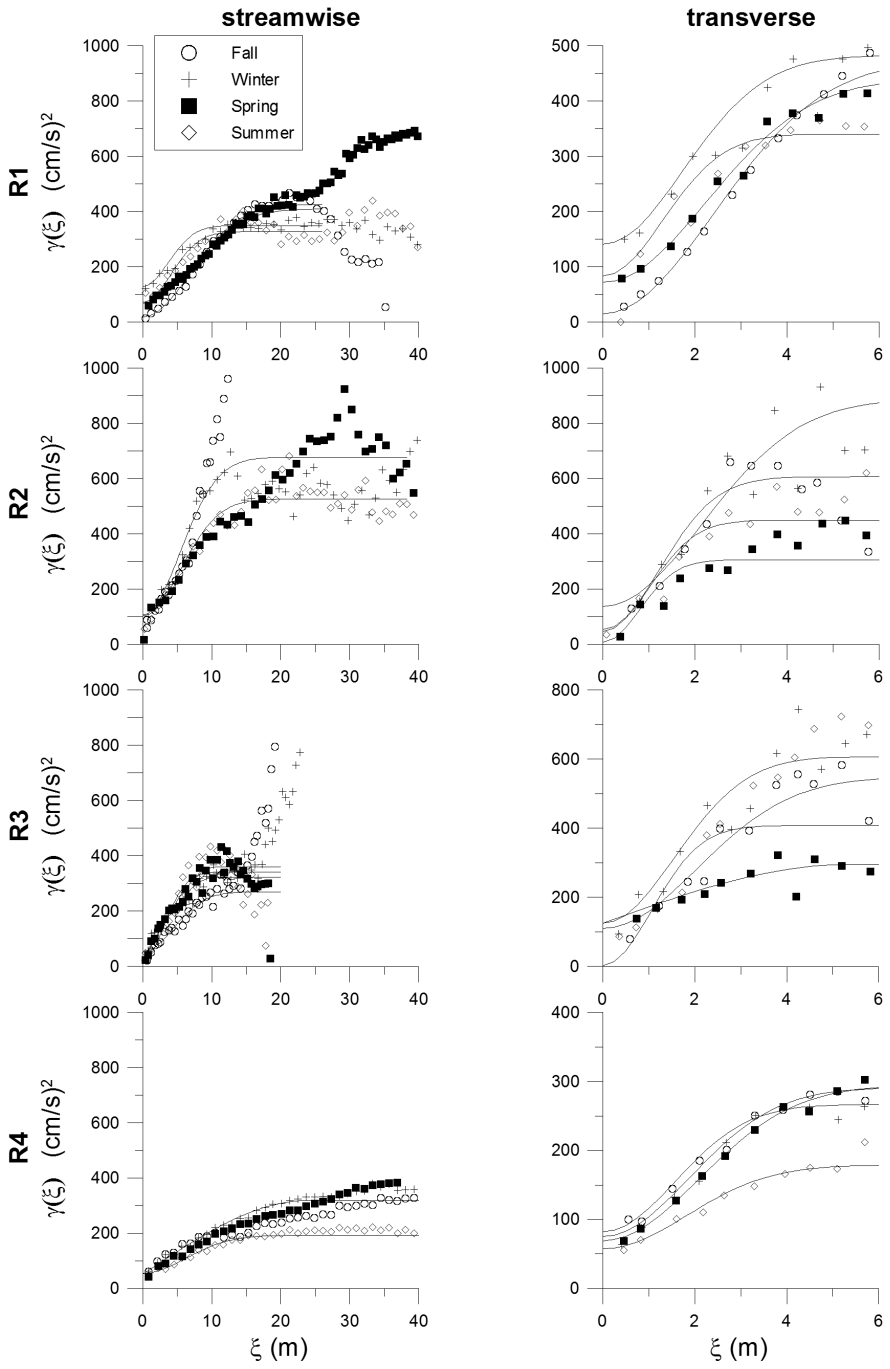

Figure 4.10: Semivariograms of depth-averaged velocity U in the streamwise and transverse directions

The nugget values were similar in both directions for all seasons and riffles, with the exception of R3 which had significantly higher nugget variance in the transverse direction. In the case of R3, a pure nugget effect may be identified during the spring sampling season. This is expected to occur if large roughness elements preclude the development of an organized flow field (Legleiter *et al.*, 2007). R3 had the largest average particle diameter of all riffles, as well as consistently low sampling flow depths (see Figure 4.3) this lack of spatial correlation in the velocity measurements is expected. It may also be possible that this nugget effect is due to a spatial structure on R3 with a shorter range than the smallest interpoint distance.

Given that the sill of the semivariogram is a representation of the overall variance (Legleiter *et al.*, 2007), it is expected to decrease for velocity as discharge increases. The influence of discharge must be isolated and it must be ensured that the roughness and geometry conditions are relatively the same. This can be confirmed for fall and winter sampling for all riffles or spring and summer for R1 and R3 (critical shear of d_{50} was not exceeded). As previously discussed, the lowest sampling discharge for all riffles occurred during the summer, which also coincides with the season of the lowest sampled flow depths (see Section 4.2.1). During this season, it is expected that the flow field will be most influenced by bed roughness elements, producing a less smooth spatial structure (Legleiter *et al.*, 2007). This spatial structure would be characterised by a higher sill value. However, the summer sampling seasons did not produce the highest sill value for depth-averaged velocity for any of the riffles, in either the transverse or the streamwise directions. Similarly, although a higher range of the semivariograms indicates a smoother spatial structure, which is expected as stage increases, this pattern is not identified in the semivariograms of depth-averaged velocity. As suggested from the coefficient of variation results in Section 4.2.2, the differences in gauge-measured sampling discharges during sampling did not produce significant patterns or changes in the semivariograms.

There does not appear to be any significant changes in the semivariograms for depth-averaged velocity after the bed-mobilizing events in the spring of 2010 on R1 and R3. In the streamwise direction for R2 and R4, however, a semivariogram model could not be fit to the experimental data, indicating a lack of spatial structure within the scale of measurement. Although the transverse semivariograms have well-defined sills which compare well with the other sampling seasons, both of these streamwise experimental semivariograms tend toward infinity at increasing lag distances, indicating a lack of spatial correlation within the scale of measurement in the streamwise direction. Between the spring and summer sampling seasons, another precipitation event exceeded critical shear stress on R2 and R4. The summer semivariograms for these riffles produce lower sill magnitudes than the preceding seasons, indicating a smoother spatial structure than prior to the peak discharge events.

4.4.2 Froude number and flow depth semivariograms

The riffle-scale semivariogram analysis of the local Froude number indicates a slightly smaller scale of spatial dependence than that observed for depth-averaged velocity (Figure 4.11). The range of the semivariograms in the transverse direction varied between 1.5 to 3.9 m, and 2.3 to 9.1 m for the streamwise directional models. The lower spatial scale of Froude number which was observed, as well as the ability to clearly define the spatial structure of the Froude number, contradicts the results of Casado *et al.* (2005), who found greater range values (up to three times longer) for F_r compared to velocity and depth.

The semivariograms in Figure 4.12 illustrate the spatial patterns of depth, in the streamwise and transverse direction. These variograms present similar scales of spatial dependence as depth-averaged velocity, and confirm the longer ranges in the streamwise direction, where the bed slope has a greater influence on changes in flow depth than microtopography in the transverse direction. Further investigation into the spatial relationship of riffle-scale flow depth can be done by taking the square root of the value of semivariance, such that the variance carries the units of the parameter itself. In terms of flow depth, this is relevant when analyzing the nugget value of the semivariograms. The range in values for the nugget magnitude of the flow depth semivariograms is 1 to 3 cm, and the average nugget is 2 cm for all riffles through the sampling seasons. These values compare well to the grain size distribution of the bed material for the riffles, summarized in Table 4.3. The nugget effect represents the randomness of the variables as the lag distance approaches 0. This is a unique characteristic of the variable, and should remain constant in all directions; the range and average of the nugget values for the flow depth semivariograms remains constant both in the transverse and longitudinal directions for all riffles. R3 has the largest d_{16}, d_{25}, and d_{50} particles, however R2 and R4 have the slightly higher maximum nugget magnitudes in both directions. The relationship between larger average particle size and a greater nugget effect is not apparent in these semivariograms for flow depth.

4.4.3 Spatial characteristics of turbulent kinetic energy

While the transverse semivariograms specified similar ranges, the streamwise semivariograms for turbulent kinetic energy did not present as well a defined spatial structure as those of depth-averaged velocity and Froude number. It was found in the coefficient of variation analysis of e_a in Section 3.5.1 that the arithmetic variability of turbulence was higher than any other parameter, and in most cases was greater in magnitude than the mean e_a, which indicates that the spatial structure may be difficult to define due to high variability. The semivariogram ranges varied from 2 m to 36 m, indicating the possibility that several scales of spatial structure were identified in the models. The magnitudes of the sills are similar in the transverse and streamwise directions, even on R2 which presented

the highest nugget and sill values of all riffles.

The spring season had the most poorly identified spatial structure in turbulence, and it was difficult to characterise and model the semivariograms. Conversely, the covariance (normalized arithmetic variance) of e_a was lowest or second lowest during the spring season on all riffles. This suggests that the variability of turbulent kinetic energy is not suitably characterised using non-spatial techniques. The parameter e_a describes a per-profile turbulence intensity per unit area and between the local and riffle scale a well-defined spatial dependency in the streamwise direction was not observed. The spatial structure of e_a during the spring on R4 is significantly different than for the other seasons on R4. Furthermore, the spatial structure of h, U, and F_r in the spring was not different than during other seasons, despite the higher sampling discharge during this period. The higher discharge perhaps revealed a coherent flow structure (measured by e_a) at the scale of measurement which was not revealed during lower discharges and flow depths.

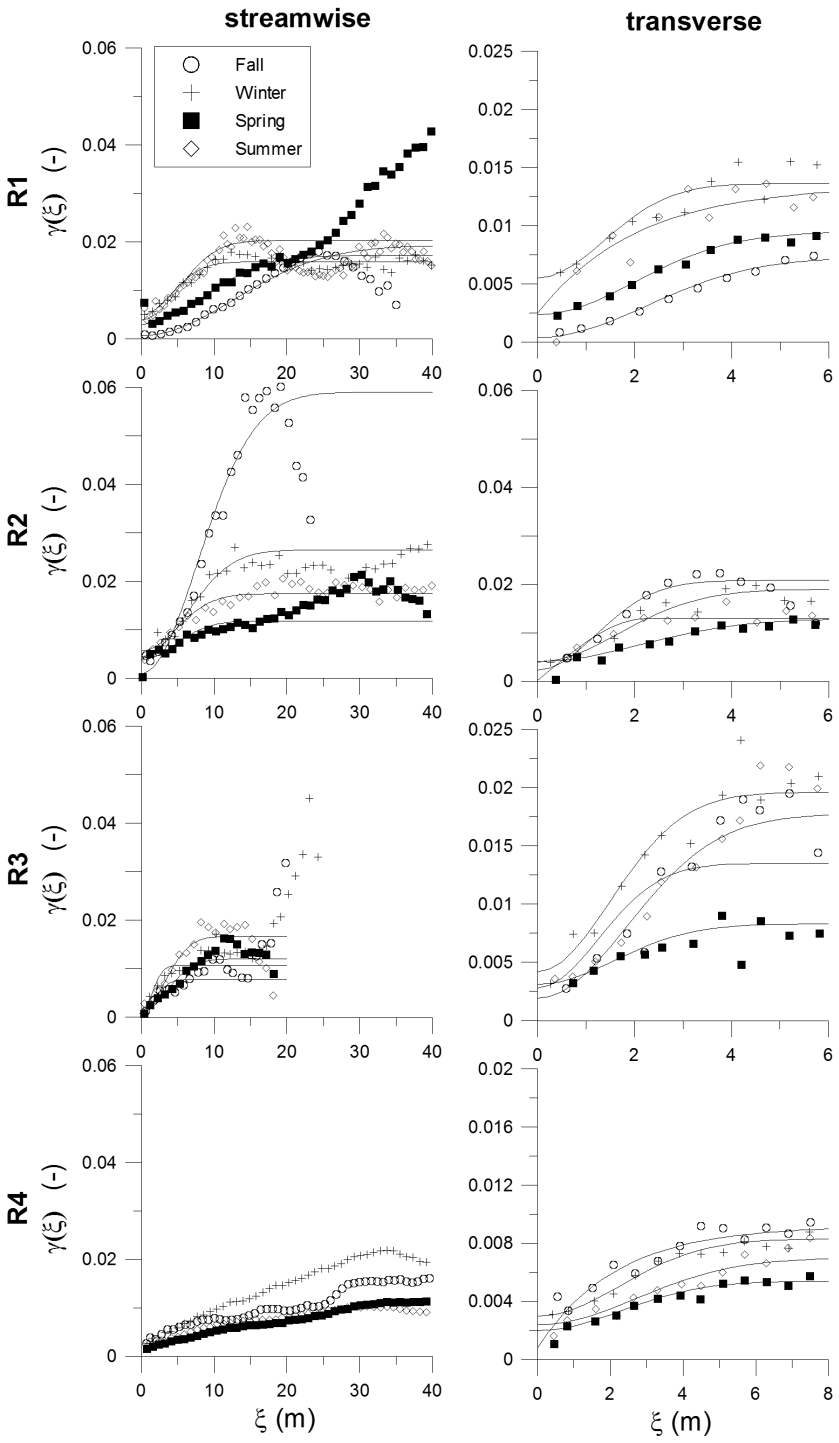

Figure 4.11: Semivariograms of local Froude number F_r in the streamwise and transverse directions

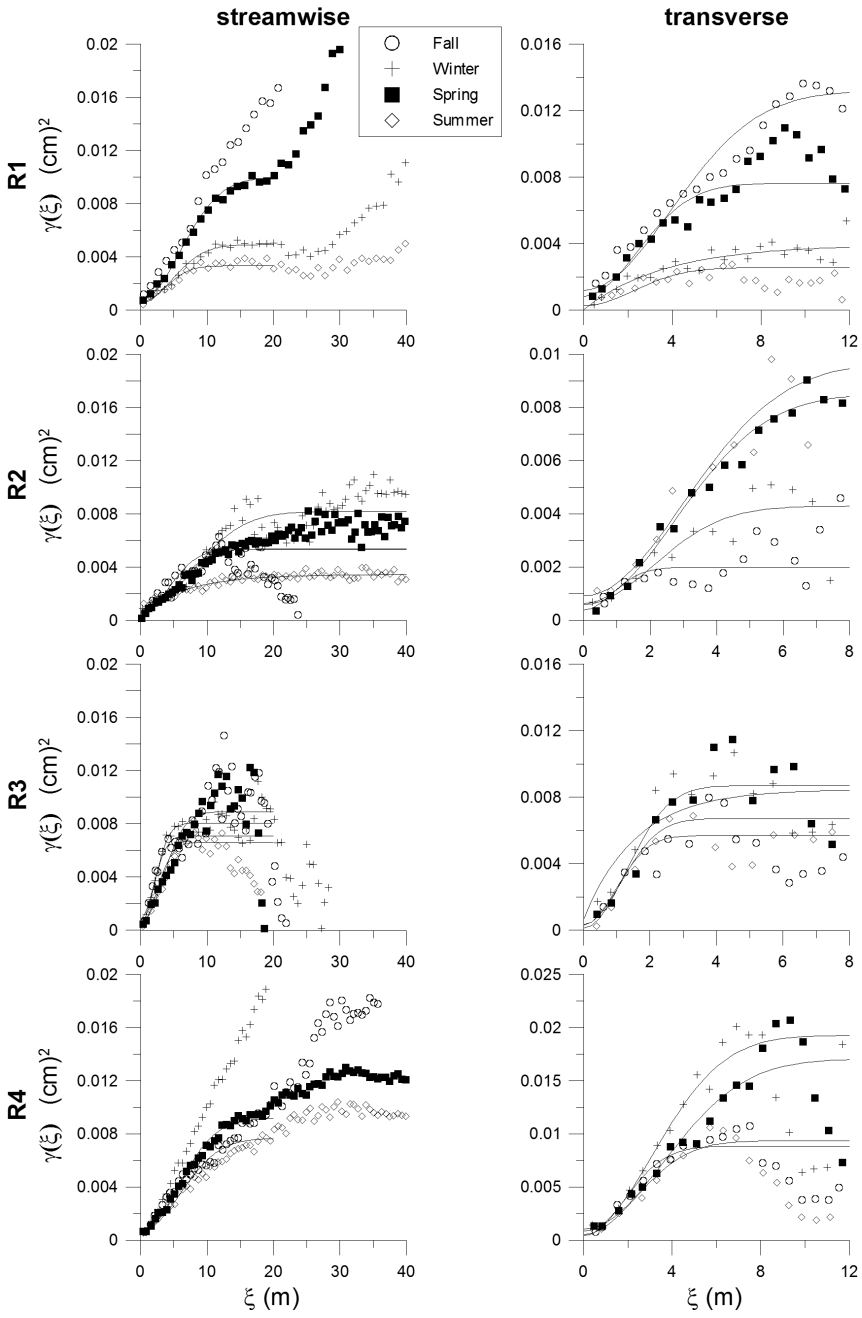

Figure 4.12: Semivariograms of flow depth h in the streamwise and transverse directions

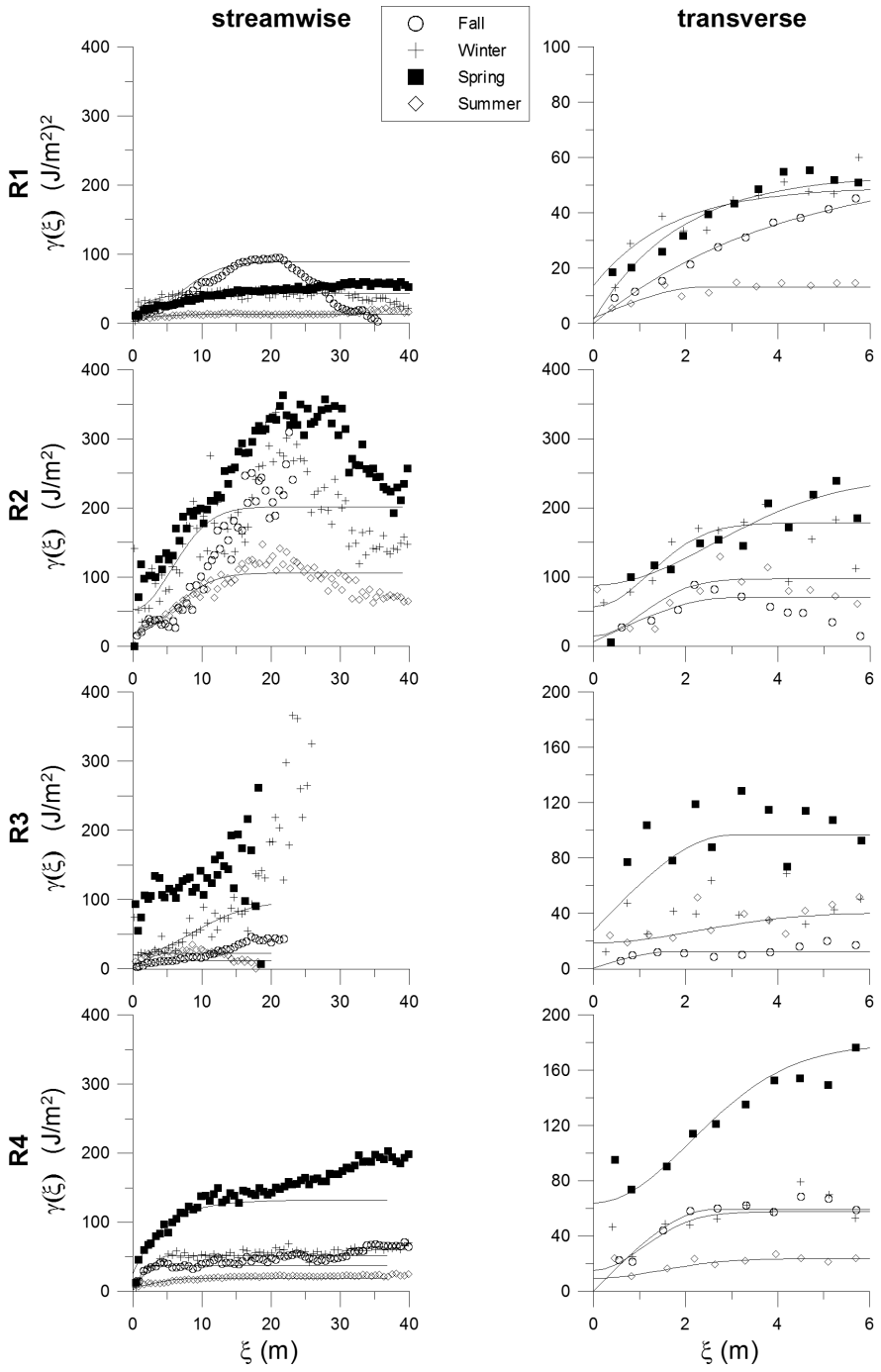

Figure 4.13: Semivariograms of turbulent kinetic energy e_a in the streamwise and transverse directions

Chapter 5

Redd-scale hydrodynamics

This chapter investigates the temporal and spatial characteristics of various hydrodynamic conditions of several brown and rainbow trout redds identified within the study reach at Whiteman's Creek. It is a high resolution intensive study of the extremely variable physical conditions in which the salmonids not only spawn, but also the abiotic environment in which the salmonid eggs incubate and hatch.

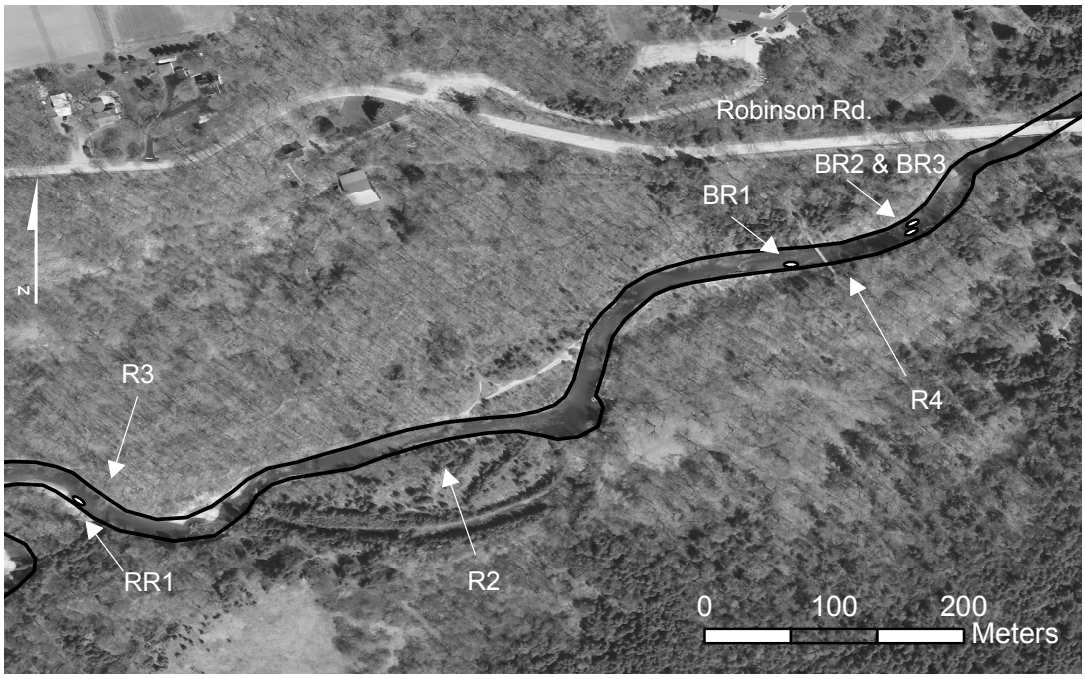

Figure 5.1: Locations of three brown trout redds (BR) and rainbow trout redd (RR) at Whiteman's Creek

Four successful redds were identified at Whiteman's Creek: three brown trout redds in the fall of 2009, and one rainbow trout redd in the spring of 2010 (BR1, BR2, BR3, RR1). The three brown trout redds were located on R4, and the rainbow trout redd was located on R3, as illustrated in Figure 5.1. Given that relatively few redds were identified, data from the different salmonid species have been combined. Based on Crisp & Carling (1989)'s regression analysis of the length of the redd tailspill to female body size, the rainbow trout was estimated to be 60 cm long, and the three brown trouts were estimated to be between 45 to 60 cm long.

5.1 Redd-proximal sediment analysis

5.1.1 Substrate conditions

Substrate samples were collected proximal to the redds following the methods described in Section 3.2.2. The sorting coefficients of both Inmans and Folk and Ward indicate that the substrate proximal to the all redds was very poorly sorted, similar to the riffle-scale substrate samples. The Fredle indices of gravel samples taken at the redds are not significantly different than the samples from the rest of the riffle ($\alpha < 0.05$).

Table 5.1: Substrate particle sizes (mm) at brown and rainbow trout redds

	d_5	d_{16}	d_{25}	d_{50}	d_{65}	d_{75}	d_{84}	d_{90}	d_{95}	$sg_{g,F}$
BR1	0.4	0.9	2.9	14.9	23.2	30.1	37.3	43.8	45.7	2.3
BR2	0.5	3.4	9.1	39.2	45.8	70.0	98.4	105.0	111.0	6.6
BR3	0.6	5.7	13.5	30.8	38.7	44.1	51.3	55.9	62.2	9.5
RR1	0.4	0.8	3.4	14.8	23.7	31.1	44.0	61.2	75.9	2.0

Of particular note in Table 5.1 are the samples collected at BR1 and RR1, which demonstrate the lowest d_{50} values (<15 mm) of any sediment sample collected in the study. The spawning substrate was also found to be negatively skewed (an extended fine tail), which is expected when sampling redds post-construction (Kondolf *et al.*, 2008). The average percentage of fine values (<1 mm) for the three brown trout redds is approximately 7%, and for the rainbow trout redd is 16 %. Based on documented maximum levels of fine sediment for both successful incubation and emergence which allow 50% emergence, these values are low enough to allow inter-gravel permeability and prevent entombment of alevins (Kondolf *et al.*, 2008). Figure 5.2 compares the grain size distributions of the riffles, redds, and published results from similar gravel bed streams.

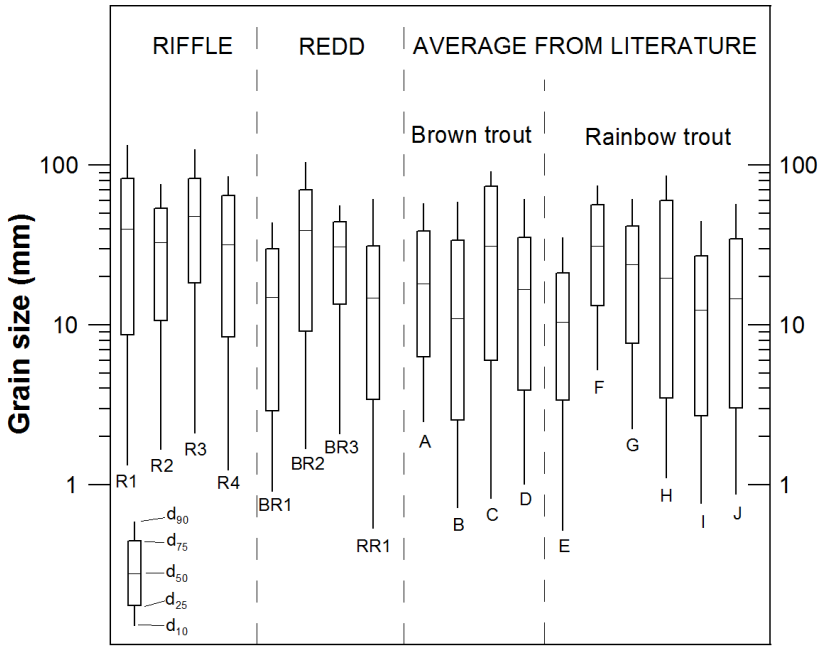

Figure 5.2: Gravel-size distributions of redd, riffle, and literature-based spawning substrate for brown and rainbow trout redds, after Kondolf & Wolman (1993). Data for the plot obtained from Hobbs (1937) (A), Reiser (1976) (B, C, D), Maddux *et al.* (1987) (E), Kondolf & Wolman (1993) (F), Hartman & Galbraith (1970) (G), Platts *et al.* (1979) (H), Spoon (1985) (I, J)

5.1.2 Erosion and deposition

Figure 5.3 illustrates the net erosion and deposition patterns on R4 during the fall, winter, and early spring. Between November to mid-march, the bed elevation surrounding/at the redds remained relatively constant, within 3 cm as indicated by the PCADP measurements. Between March 9 and March 22, erosion occurred on the downstream end of both BR2 and BR3. By the time the spring flood event (bankfull) had passed, on March 30 net deposition had occurred on the downstream end with the net result from Feb to March 30 (post freshet) being that erosion between 5 and 10 cm occurred in limited areas around BR1 and BR3 particularly. As mentioned in Section 4.3.2, the scour chains indicated erosion up to 8 cm between the winter and spring.

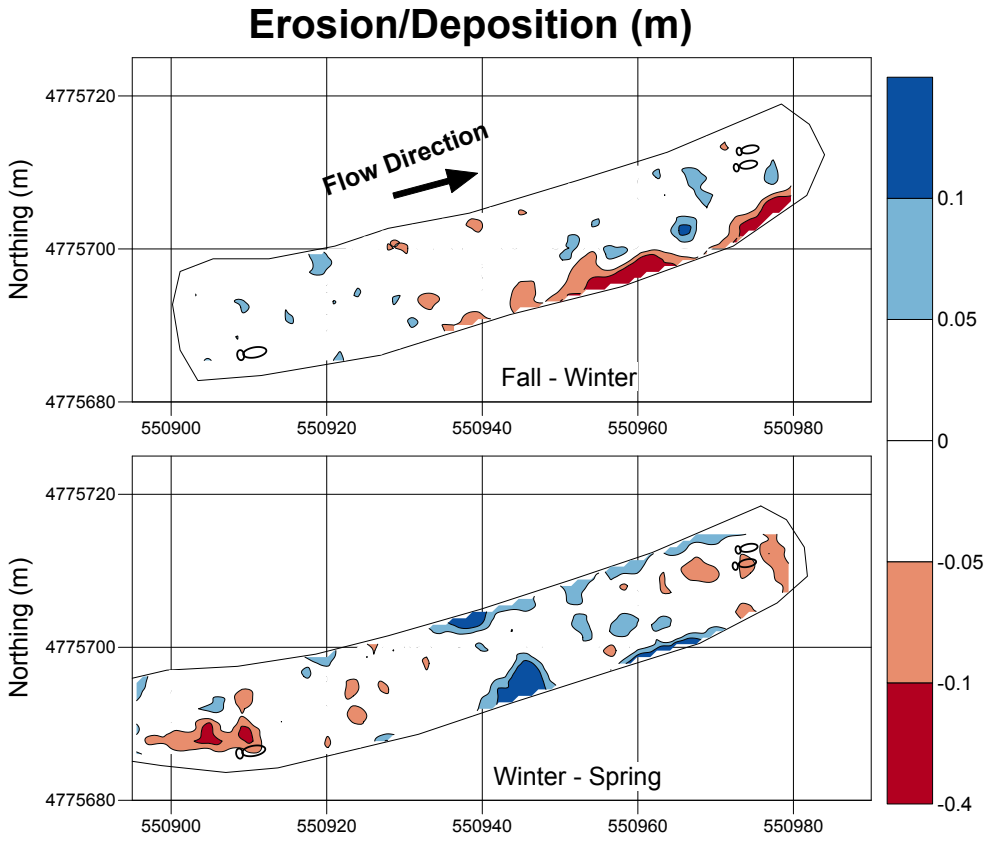

Figure 5.3: Erosion and deposition on riffle 4 during spawning and incubation periods

5.2 Hydrologic setting

5.2.1 Seasonal flows

A one-dimensional HEC-RAS model was used to develop a velocity record along the entire study reach at Whiteman's Creek. The 15-minute discharges at the WSC gauge station 02GB008 during which velocity measurement was occurring were extracted and used in the model. Figures 5.4 and 5.5 compare the distribution of velocities from the model with the field measured velocities on R3 and R4. The average and standard deviation of the field measured velocities have also been indicated. Theoretically, these two histograms should produce similar results, since they represent the same location at the same discharges. The model results are based upon the geometry and roughness of a single cross section surveyed at R3 and R4, and the velocity corresponds to the average main channel velocity. Given

that the spatial resolution of the field data is significantly higher than that of the model, it is expected that the variance of the model-based histogram would be lower.

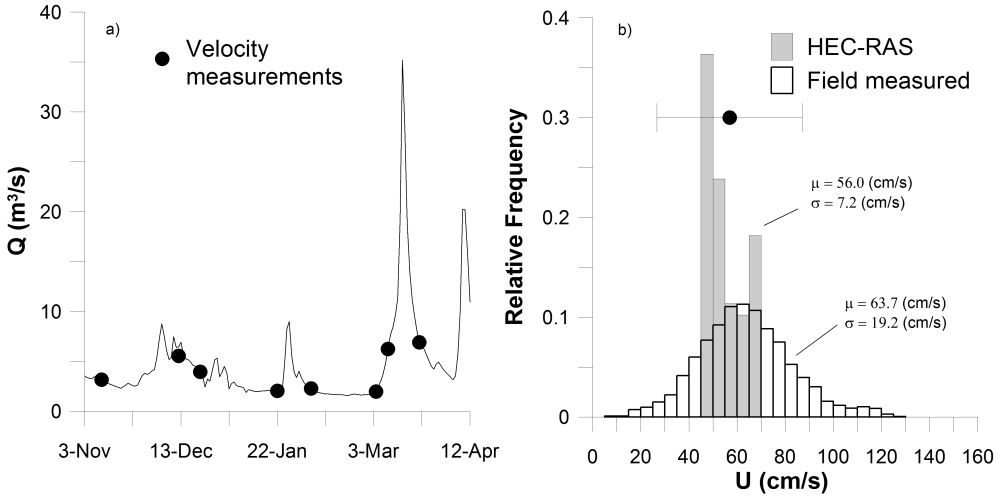

Figure 5.4: a)Hydrograph at Whitemans Creek 02GB008 and R4 velocity measurements b) Average cross-sectional velocity at R4 from HEC-RAS model during sampling periods and field measured depth-averaged velocity on R4.

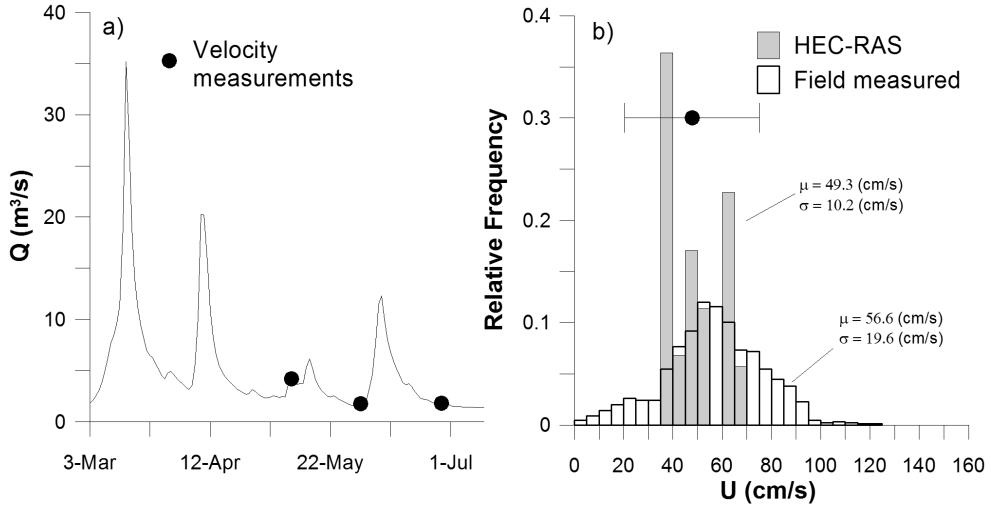

Figure 5.5: a)Hydrograph at Whitemans Creek 02GB008 and R3 velocity measurements b) Average cross-sectional velocity at R3 from HEC-RAS model during sampling periods and field measured depth-averaged velocity on R3

For both riffles 3 and 4, the mean velocity values of the model and the field data are statistically different (ANOVA) but only differ by less than 13%. Conversely, the entire range of model-derived velocities is smaller than a single standard deviation of high resolution velocity data. In other words, a reach-calibrated longitudinal model gives a poor representation of the highly variable hydrodynamic characteristics of a shallow gravel-bed stream. Furthermore, cross-sectionally-averaged roughness estimates used in the model contribute to greater uncertainty when considering the variability of roughness observed riffle-wide (see Section 4.3.3).

5.2.2 Critical discharges

Similar to Figure 4.2, Figure 5.6 illustrates the critical discharge associated with the d_{50} particle at each redd. The critical discharge values were derived from the HEC-RAS model; the critical shear stress for the d_{50} particle size was calculated following Shields method, and the critical shear values were associated with a corresponding discharge in the HEC-RAS model. The method incorporates uncertainty when considering the shear values in the model are cross-sectionally averaged, and the variance of local τ_0 across a single riffle is high (see Figure 4.4).

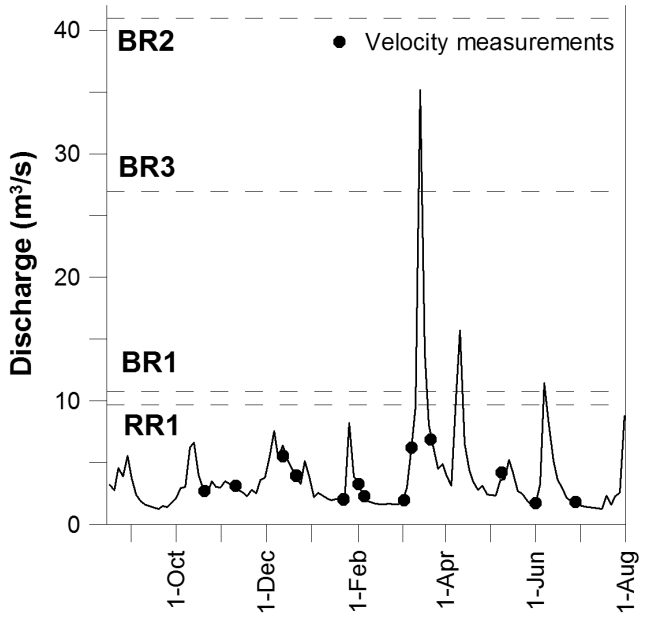

Figure 5.6: Critical discharges of the d_{50} particles at each redd location (dashed lines), in relation to the hydrograph during 2009/2010

Considering only the local bed shear determined from the velocity profiles during measurement, Figure 5.7 illustrates the variability of local bed shear. Through all sampling discharges, τ_0 tended to be higher over the tailspill of the redd, and higher over the redd than on points on the riffle which were not proximal to redds. There were many occurrences when the shear stress during velocity measurement exceeded the critical shear stress of the d_{50} particles on BR1 (10.8 N/m^2) or RR1 (9.7 N/m^2) however, the critical shear stress on the other two redds was never exceeded during sampling. Although the profile-derived bed shear does not provide a complete image of the incubation period conditions, the local bed shear results during the isolated but frequent sampling periods indicate that the four redds experienced varied boundary shear stress.

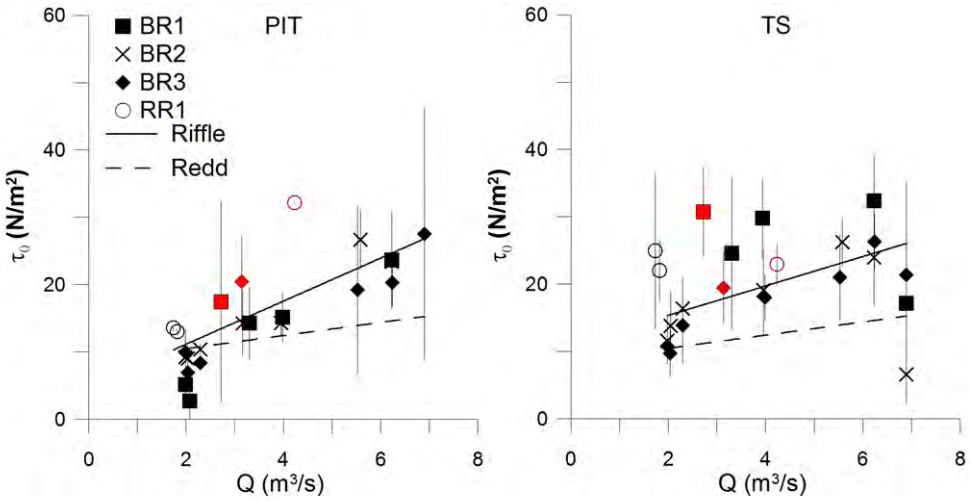

Figure 5.7: Discharged-ranked bed shear (τ_0) derived from measured velocity profiles over the pit and tailspill (TS)

5.3 Hydrodynamic characteristics of redds

5.3.1 Discharge-ranked hydraulic variables

Figures 5.8, 5.9, and 5.10 illustrate the range of commonly used physical variables evaluating habitat conditions at the pit and tailspill of the redds, ranked by the discharge at which measurement occurred. These measurements occurred during the sampling periods indicated in Figures 5.5 and 5.4, and red indicates measurements taken immediately following redd construction.

A linear regression of the selected parameters at the redds with respect to discharge produced significant relationships ($p<0.0001$). The same relationship for all other points on the riffle was also included for comparison. The data from the rainbow trout redd is included in these plots for comparison, but was not included in the regression analysis. The regressions in these figures are a redd and riffle-scale form of linear hydraulic geometry relationships (Leopold, 1994).

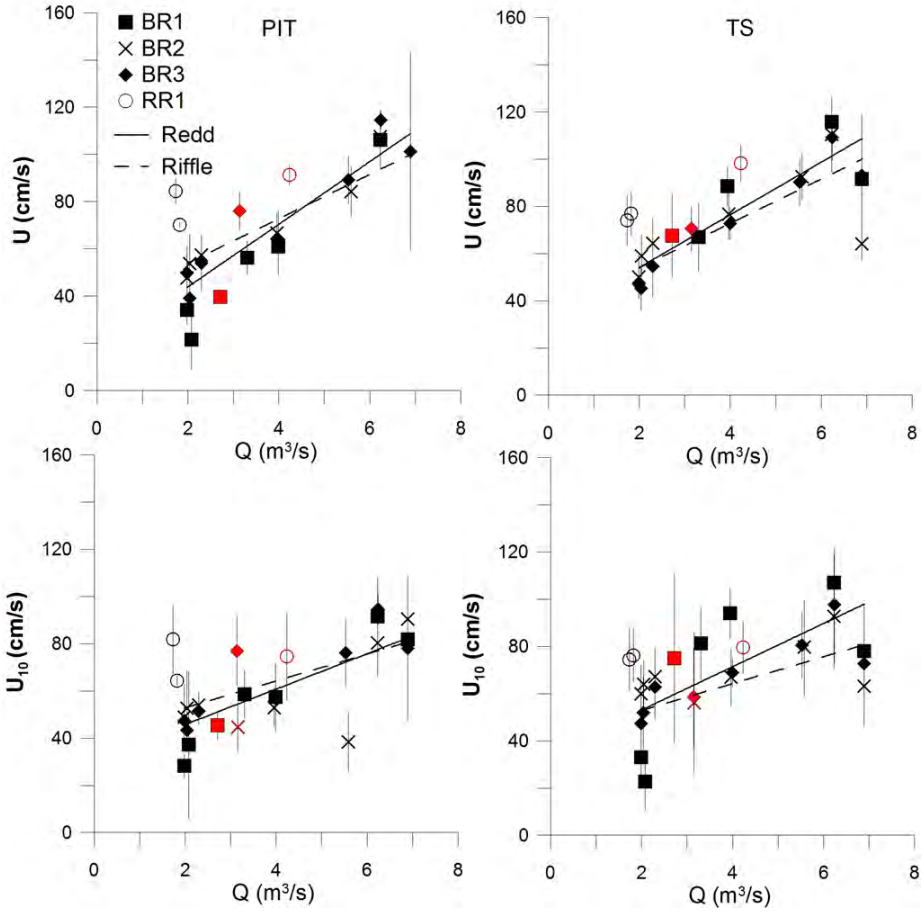

Figure 5.8: Discharge-ranked average and standard deviation of pit and tailspill (TS) depth-averaged velocity U and nose-level velocity U_{10}

Both the pit and the tailspill distinguish themselves when considering depth-averaged velocity. In this case they both present slightly higher velocities than the rest of the riffle at high discharges. The different intercepts of the regression of pit and tailspill depth-averaged velocity (but similar slopes) ($p<0.05$) implies that the tailspill reveals higher velocities than the pit and rest of the riffle at low discharges. This may be an indication

of the convective flow hypothesis at the redds: flow is accelerating over the top of the tailspill, and the behaviour persists (but decreases) through all discharges (Wu, 2000). In the region close to the bed, the nose-level velocities reveal even stronger evidence of the flow acceleration. While the pit velocities are similar to the rest of the riffle, the tailspill velocities are consistently higher through the range in sampling discharges. Lower velocities observed at low discharge in the pit of the redd compared to the remaining riffle may allow female salmonids to remain virtually motionless in the pit during the spawning process (Schmetterling, 2000).

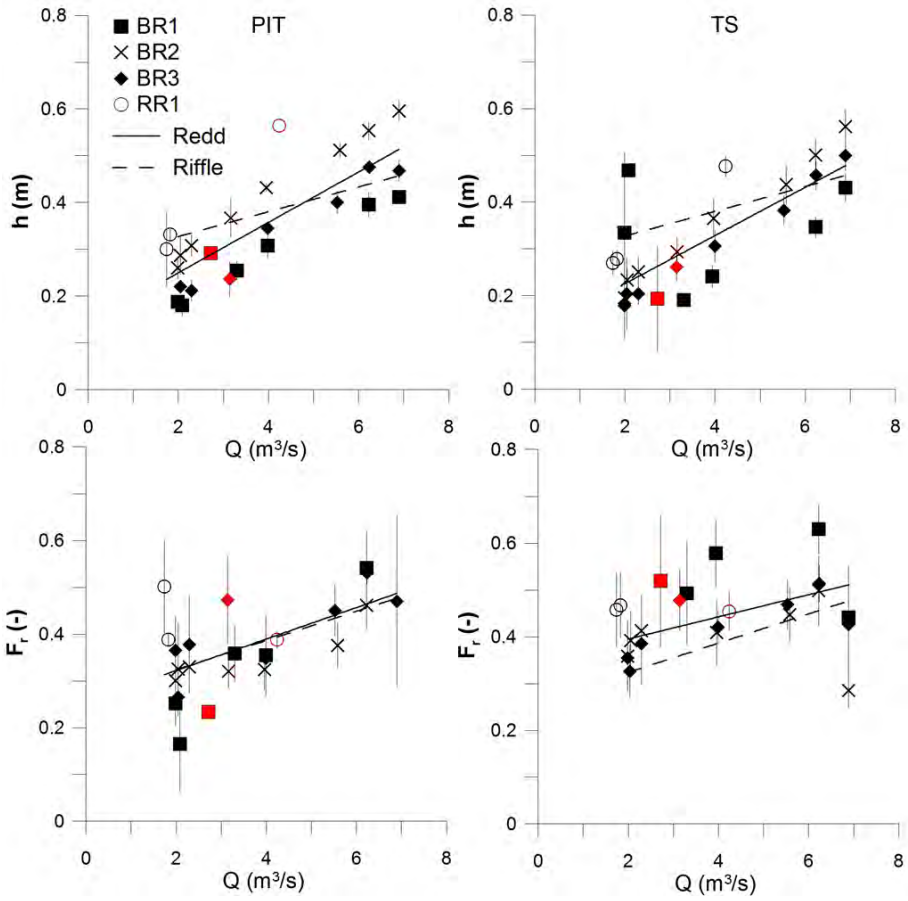

Figure 5.9: Discharge-ranked average and standard deviation of pit and tailspill (TS) local flow depths h and Froude number F_r

When regressing flow depth with discharge, the pit and tailspill both exhibit relationships which vary significantly from the remaining points on the riffle, but have statistically similar ($p<0.05$) slopes to each other. The pit and tailspill flow depths behave similarly,

except for the greater intercept of the pit regression, confirming higher flow depths at the pit than the tailspill for all discharges measured. In both cases at low discharges the flow depths are lower than on the rest of the riffle. This pattern persists for the tailspill measurements over almost all discharges, as expected. The lower pit flow depths compared with the riffle appear contradictory, given that the flow depths in the pit are expected to be higher. However, this confirms that the redds were located in regions of existing lower flow depths than the riffle-average, and despite the salmonids creating a localized higher flow depth by digging a hollow (in the pit), the flow depth at the redd was still lower than the remaining riffle average.

As described in Equation 2.2, the Froude number is the ratio of depth-averaged velocity to flow depth. As discharge increases, the velocity and depth have been shown to increase at varying rates. On a riffle-scale, F_r was observed to increase with increasing discharge (Table 4.2). The redd-scale results confirm a similar F_r - Q relationship at both the pit and the riffle, and higher F_r values occurred over the tailspill for all discharges sampled. This indicates that flow over the tailspill is more likely to reach critical depth and attain supercritical flow before the rest of the riffle, creating a higher potential for erosion and scour of the egg pockets.

The e_a vs discharge relationship at the pit and tailspill is the same (both slope and intercept), and indicates lower turbulent kinetic energy values at low discharges than the rest of the riffle and slightly higher e_a for high discharges. Although it is not possible to identify whether or not this condition existed prior to redd construction, it appears that at lower discharges the salmonids are selecting locations which allow for lower turbulence than the remaining riffle. Additionally, this phenomenon is statistically the same over both the pit and the tailspill, so either the redd structure did not modify the existing low e_a condition in the location, or the pit and tailspill create similar characteristically low-turbulent structures. Regardless, the presence of low e_a at the redd location corroborates the findings of Marchildon *et al.* (2011), who noted that the salmonid redds at Whiteman's Creek were consistently located in regions of low turbulence ($<15\,\mathrm{J/m^2}$) at low discharges ($<4\,\mathrm{m^3/s}$).

It is also important to note the difference in e_a values between the rainbow trout vs brown trout immediately after spawning (Figure 5.10). Although brown trout and rainbow trout both select riffle habitats for spawning, the brown trout in this study appear to have selected redd locations that were very similar in e_a over various discharges, whereas the rainbow trout redd appears to have higher e_a values throughout the incubation period, and indicating less linear flow. It is not possible to determine if this is a specific difference between the species with only a single rainbow trout redd, but it is worth noting for future study. A possible explanation for differences in e_a between brown and rainbow may be the difference in rigorous selection behaviour of the trout. The incubation period for spring-spawning rainbow trout can be as low as 2.5 months, whereas brown trout eggs may

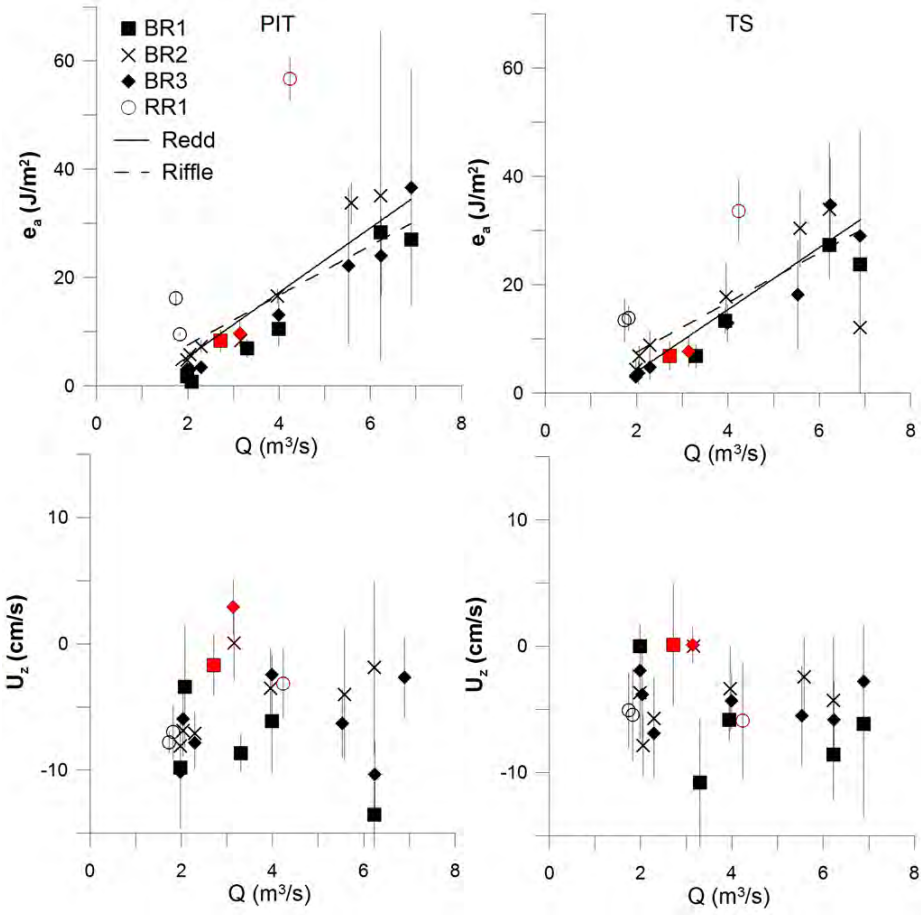

Figure 5.10: Discharge-ranked average and standard deviation of pit, tailspill (TS) of turbulent kinetic energy e_a and vertical velocity u_z

incubate for up to 6 months during the winter-spring, where they are susceptible to much more variable flow conditions.

These results for profile-based turbulence and depth-averaged velocity may indicate that salmonids select locations for redds with consistently higher velocities over the tailspill which allows for downwelling. These sites are also characterised by lower turbulence, which would allow the downwelling to continue consistently without interruption from coherent turbulence.

The vertical velocities measured by the PCADP at the nose-depth (Figure 5.10) do not indicate a coherent relationship with discharge, although over the pit and the tailspill, downward vertical velocity persists through the entire range in measured discharges. While this does not necessarily correspond to downwelling or upwelling groundwater velocities, the persistent tendency does indicate that it may be possible, following further calibration and confirmation, to accurately measure strong tendencies in groundwater discharge/recharge using the high-resolution PCADP in the near-bed environment.

5.3.2 Relative frequency histograms

The frequency distribution of depth-averaged velocity at points other than the redds during each sampling period is illustrated in Figures 5.11 and 5.12. Normality was confirmed for each sampling period ($\alpha = 0.05$) except for $Q = 6.23\,\mathrm{m}^3/\mathrm{s}$, and the 95^{th} percentile was determined for the associated Gaussian distribution curves. Also included in Figures 5.11 and 5.12 is the Gaussian curve fit to the frequency distribution for all of the depth-averaged velocity measurements taken at locations other than the redds (all sampling seasons pooled). This curve may be considered as a riffle-scale baseline, representing the average distribution of depth-averaged velocity on R4 at wadeable flow depths during 2009-2010. While Section 5.3.1 examines a specific redd-to-riffle discharge-dependent comparison, Figures 5.11 and 5.12 highlight the variability between the redd and riffle measurements at specific discharges.

The depth-averaged velocities measured over the pit and tailspill of the redd are within the 95^{th} percentile of other points measured on the riffle during each sampling period, with the exception of the pit at BR1 during the January sampling period when the average flow depth was only 0.24 m.

The majority of the frequency distributions of profile-based turbulent kinetic energy in Figures 5.13 and 5.14 were not normally distributed ($\alpha = 0.05$) most likely due to the substantial positive skewness exhibited. The longer tail to the right side of the distribution indicates relatively few high turbulence values. As discussed in Section 5.3.1, the redds do not present high e_a relative to the rest of the riffle, at each sampling discharge.

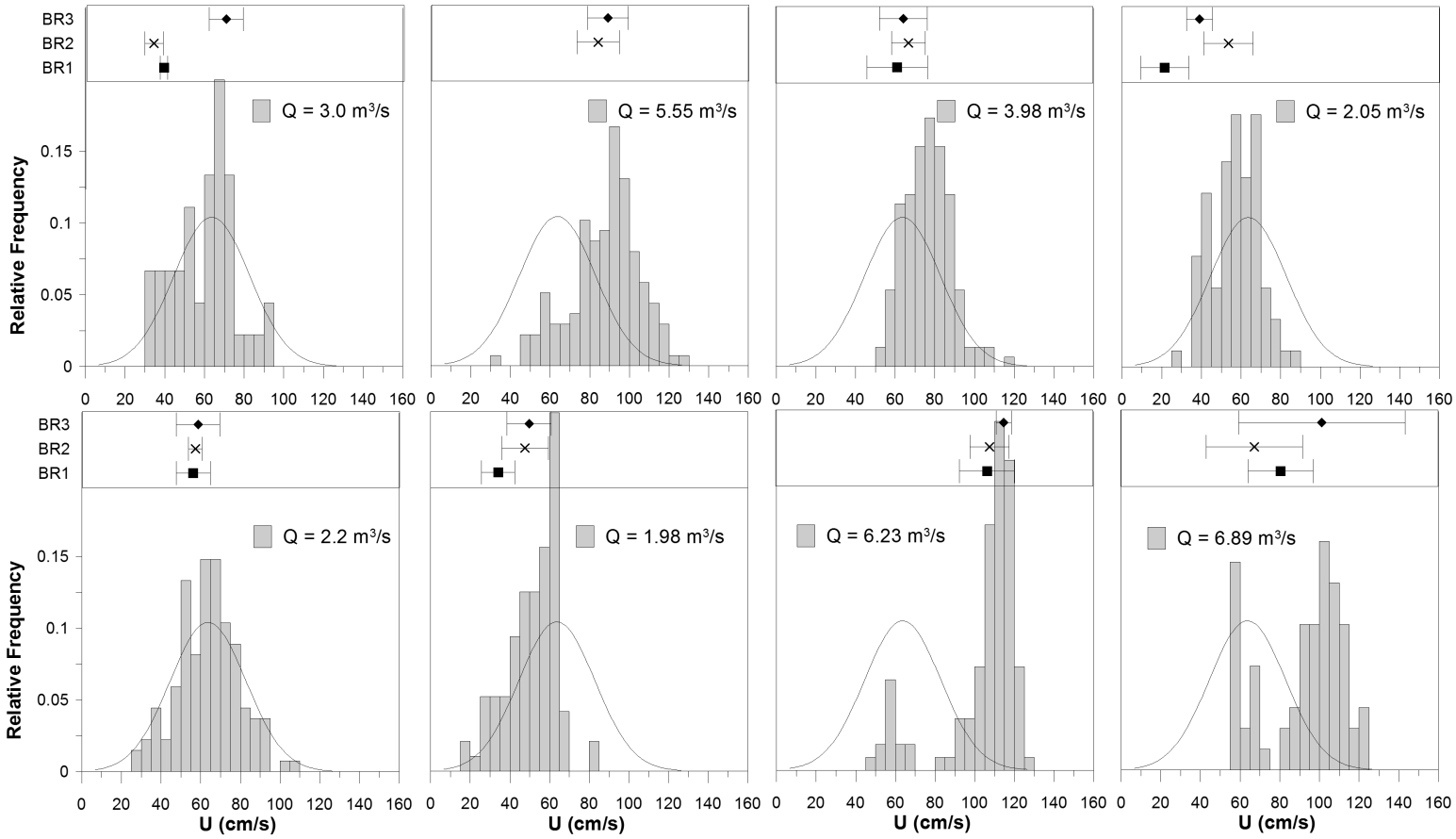

Figure 5.11: Relative frequency histograms of depth-averaged velocity at various discharges (grey) and measurements collected during entire sampling year (solid line), with average and standard deviation of depth-averaged velocity over the pit

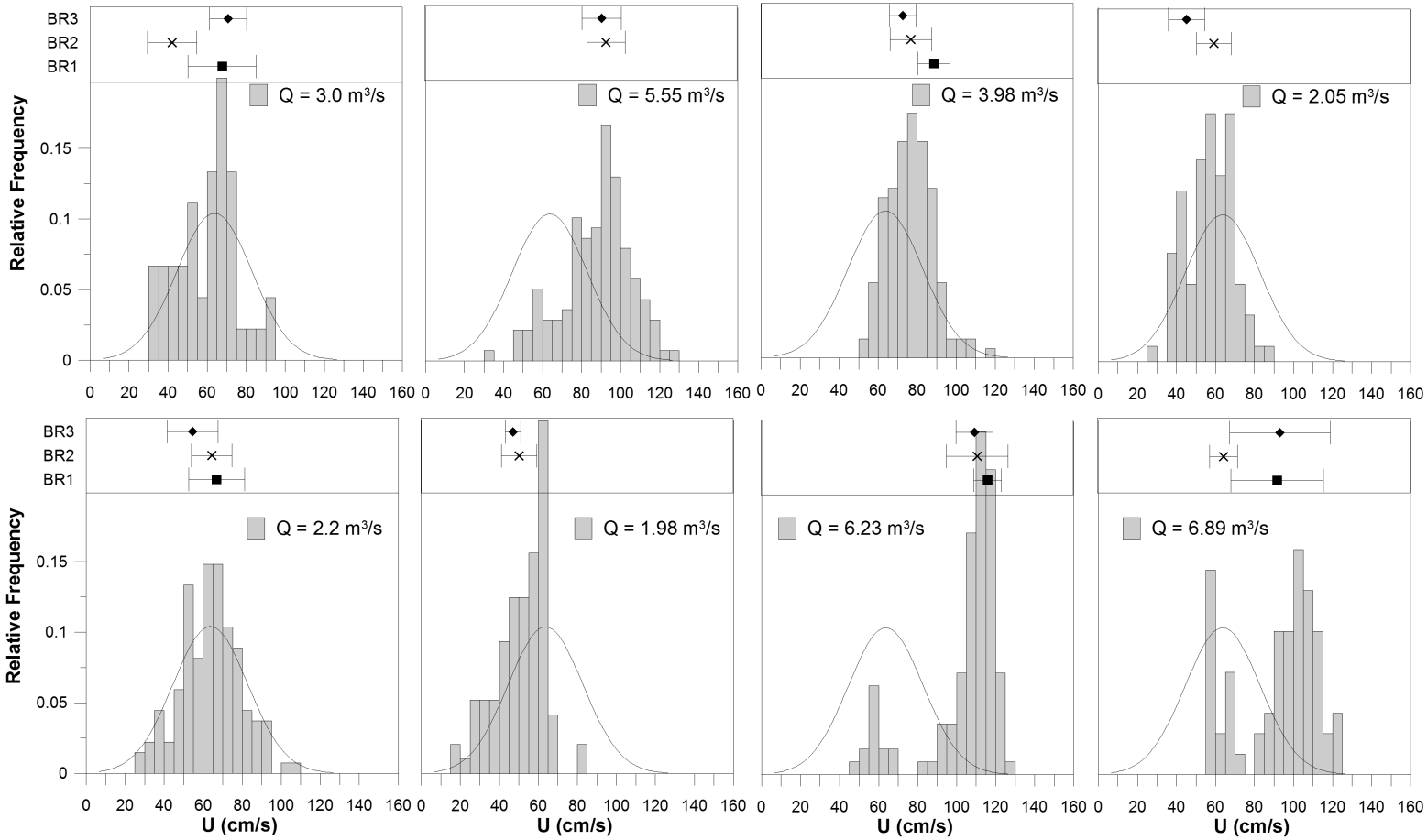

Figure 5.12: Relative frequency histograms of depth-averaged velocity at various discharges (grey) and measurements collected during entire sampling year (solid line), with average and standard deviation of depth-averaged velocity over the tailspill

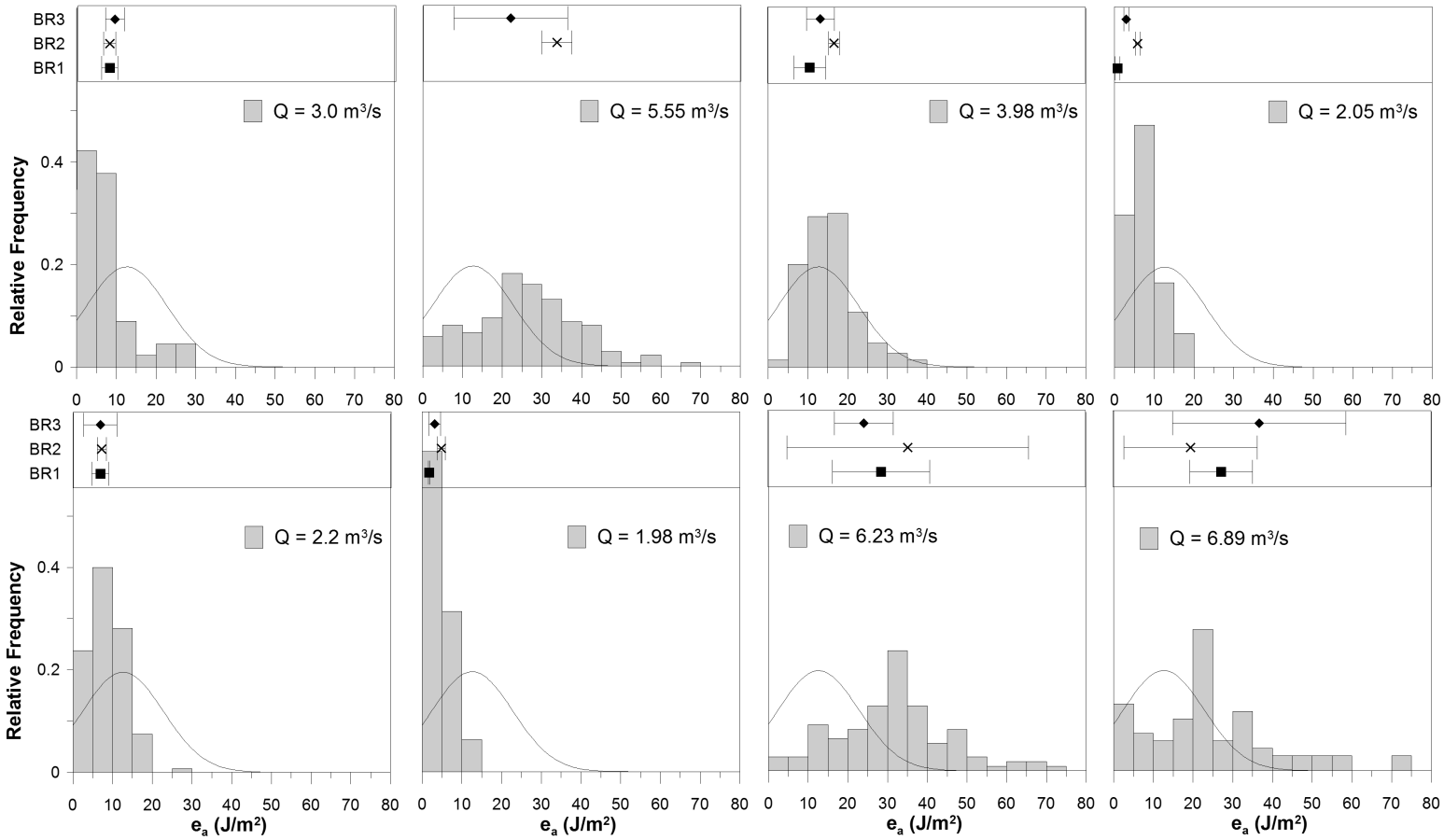

Figure 5.13: Relative frequency histograms of turbulent kinetic energy at various discharges (grey) and measurements collected during entire sampling year (solid line), with average and standard deviation of turbulent kinetic energy over the tailspill

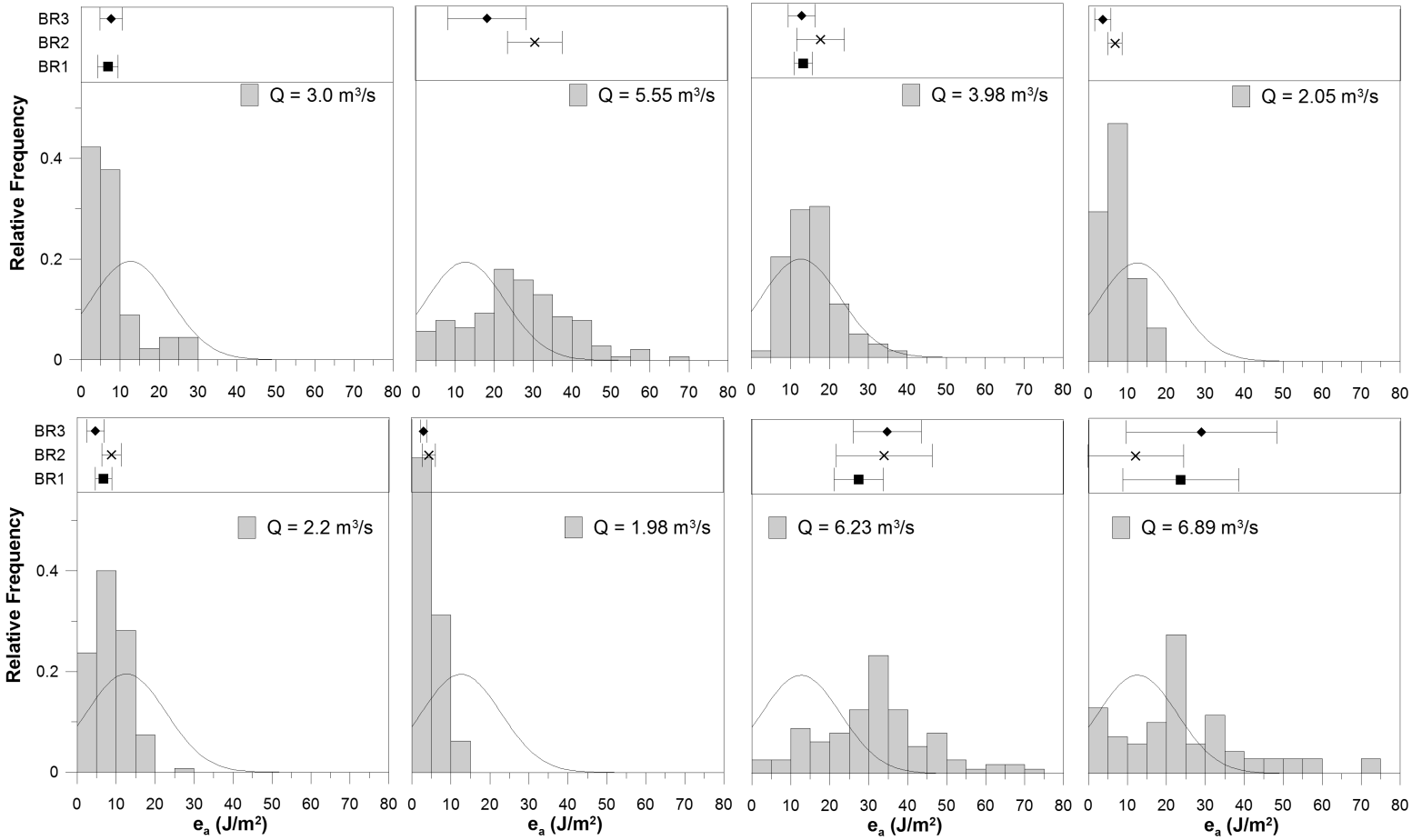

Figure 5.14: Relative frequency histograms of riffle-wide turbulence kinetic energy at various discharges (grey) and riffle-wide measurements collected during entire sampling year (solid line), with average and standard deviation of turbulence kinetic energy over the pit

5.4 Spatial characterisation of redds

The seasonal omni-directional semivariograms in Figures 5.15 and 5.16 for depth-averaged velocity were calculated both around the redds and riffle-wide. As opposed to the global prediction method used in Section 4.4, these semivariograms include only a subset in a spatial neighbourhood around the redd location: a forced sample semivariogram. An elliptical search was used to determine which points were within the region of the redd. The regionalized semivariograms were calculated, following the standard semivariogram approach but limited to the region of the redd using a lag increment (ξ) of 0.25 m. The semivariogram models were developed but not explicitly used in the estimation of the redd-regional semivariograms due to the lack of coherent spatial structure defined by these omni-directional semivariograms. The redds do not appear to significantly deviate from the seasonal riffle-wide spatial patterns established in Section 4.4, with the exception of BR1 which begins to slightly deviate from the remaining redd- and riffle-scale semivariograms during the January sampling period. Additionally, when comparing the semivariograms from prior to and following the bed mobilizing event in March ($Q = 6.23\,\mathrm{m}^3/\mathrm{s}$ and $Q = 6.89\,\mathrm{m}^3/\mathrm{s}$), the maximum semivariance (sill) is observed to have increased at all redds. The bed mobilizing event appears to have increased the spatial variance observed on R4.

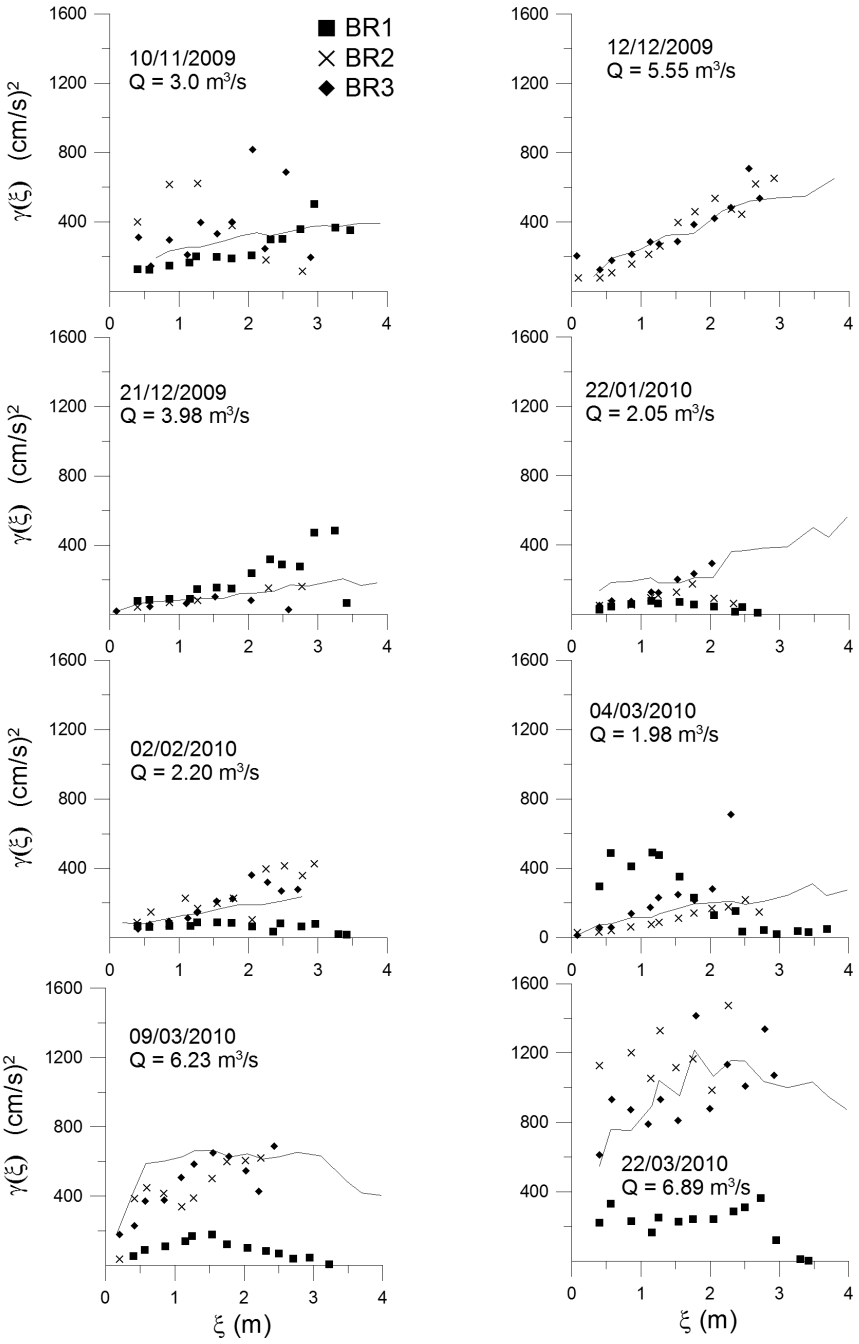

Figure 5.15: Redd-regional semivariograms of depth-averaged velocity around brown trout redds on R4, compared with riffle-scale semivariogram

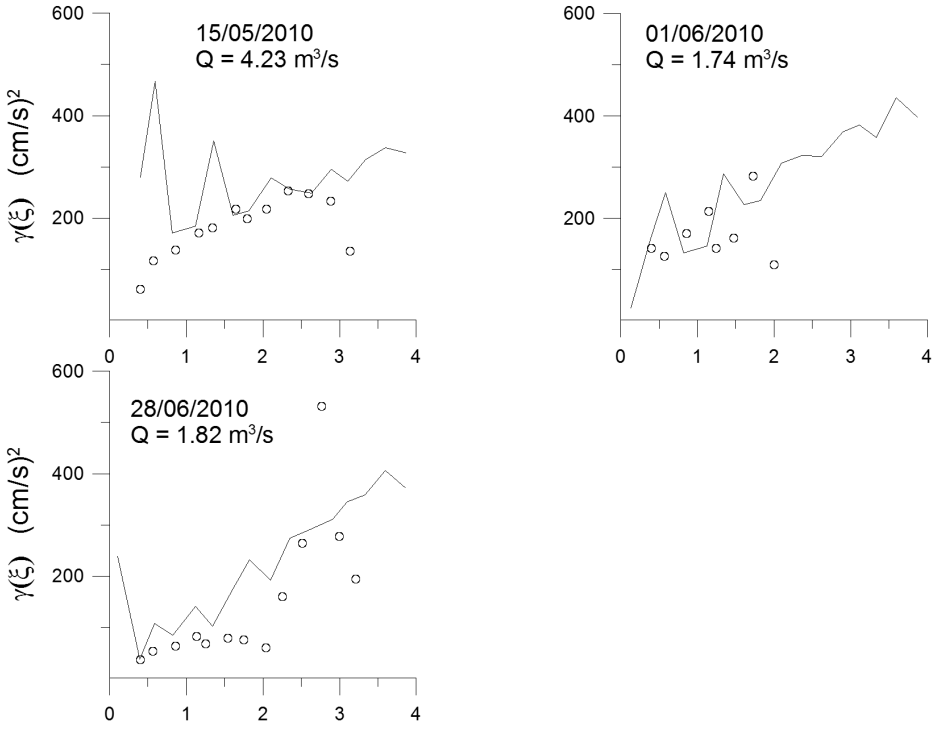

Figure 5.16: Redd-regional semivariograms of depth-averaged velocity at rainbow trout redd on R3, compared with riffle-scale semivariogram

Chapter 6

Conclusions and recommendations

The spatial and temporal variability in hydrodynamic characteristics of four riffles in a gravel-bed river and the salmonid redds which they contained was measured and quantified. The relationship between physical habitat metrics (derived from velocity and substrate measurements) and brown and rainbow trout spawning site selection and the incubation environment was investigated. Various metrics (depth-averaged velocity, bed shear stress, flow depth, Froude number, Reynold's number, turbulent kinetic energy per unit area) were analyzed at both the riffle and redd spatial scale, using traditional statistical techniques as well as geostatistical methods (semivariograms in this case) seldom applied to fluvial hydraulics.

The four seasonal velocity data sets collected at each riffle had means and variances which were highly sensitive to differences in river discharge during sampling. These changes in discharge however did not produce measurable differences in the spatial structure indicated by the semivariograms. Geostatistical analysis of the riffles revealed spatial dependencies of velocity in the streamwise direction acting at a scale two to three times greater than the transverse direction, as well as the presence of nested spatial structures operating at several scales. Similarly, the transverse spatial structure was consistently less smooth, and showed a less important spatial variability than the streamwise direction. The nugget values identified in the semivariogram analysis may be useful in determining a sampling resolution required to capture particular flow structures acting at a scale smaller than the original measurement resolution.

Four redds constructed by salmonids ranging in sizes estimated from 40 cm to 60 cm were found to be located in regions which during a bankfull event, were subjected to scour ($<$10 cm) which was lower than the estimated egg burial depth ($\approx$15 cm). Frequent high-resolution nose-level velocity measurements at varying discharges during incubation revealed the presence of convective flow acceleration over the tailspill of the redd, increasing the likelihood for inter-gravel flow through the tailspill sediment at the egg pockets.

Furthermore, the relationship between turbulent kinetic energy at the redds reveals that salmonids selected sites during spawning (at low discharge) which allow for lower turbulence than the remaining riffle, within the range of wadeable flow depths examined.

The importance of profile-derived turbulent kinetic energy in salmonid spawning was confirmed. Conversely the lack of distinctiveness in local Froude number was also revealed in the intensive redd-proximal velocity measurements. Spatial patterns in discretized high-resolution velocity measurements on a gravel-bed river were quantified and distinguished using the semivariogram approach, revealing a complex system of multi-scaled dependencies.

The field techniques described in this study should continue to be refined and optimized. Collecting data at a sufficient resolution which permits an accurate spatial characterisation of the riffle habitat at a wide range in flows is a process which requires further validation. The use of one-dimensional models (such as HEC-RAS) to complete the hydrodynamic picture during non-wadeable flow depths in a hydrograph will not capture the variability observed at the riffle-scale in a gravel-bed stream. The turbulent velocity profiles presented in this study may benefit from further analysis using non-linear regression approaches to characterise the distribution with other theoretical relationships, such as the power-law. A time-series based statistical analysis of turbulence may also reveal coherent turbulent structures not captured using profile-based turbulent kinetic energy per unit area. In terms of river research and engineering, spawning habitat enhancement projects could benefit from redd microhabitat measurements such as those provided in this study. The ability to quantify available habitat at an appropriate scale using metrics which are readily collected is of great value.

Bibliography

Afzalimehr, H., & Anctil, F. 2001. Friction velocity associated to a non-uniform flow and an intermediate scale roughness. *Journal of Hydraulic Research*, **39**(2), 181–186. 8

Afzalimehr, H., & Rennie, C.D. 2009. Determination of bed shear stress in gravel-bed rivers using boundary-layer parameters. *Hydrological Sciences Journal*, **54**(1), 147–159. 8

Anderson, D.W. 1983. *Factors affecting brown trout reproduction in southeastern Minnesota streams*. Tech. rept. Minnesota Department of Natural Resources, Division of Fish and Wildlife, Section of Fisheries. 6

Armstrong, J.D., Kemp, P.S., Kennedy, G.J.A., Ladle, M., & Milner, N.J. 2003. Habitat requirements of Atlantic salmon and brown trout in rivers and streams. *Fisheries Research*, **62**(2), 143–170. 4, 7

Armstrong, M. 1998. *Basic linear geostatistics*. Springer Verlag. 49

Biron, P.M., Lane, S.N., Roy, A.G., Bradbrook, K.F., & Richards, K.S. 1998. Sensitivity of bed shear stress estimated from vertical velocity profiles: the problem of sampling resolution. *Earth Surface Processes and Landforms*, **23**(2), 133–139. 10

Bradbrook, K.F., Lane, S.N., Richards, K.S., Biron, P.M., & Roy, A.G. 2000. Large eddy simulation of periodic flow characteristics at river channel confluences. *Journal of Hydraulic Research*, **38**(3), 207–215. 11

Bridge, J.S. 2003. *Rivers and floodplains: forms, processes, and sedimentary record*. Blackwell Science. 8

Bunte, K., & Abt, S.R. 2001. *Sampling surface and subsurface particle size distributions in wadable gravel-and cobble-bed streams for analyses in sediment transport, hydraulics, and streambed monitoring*. Tech. rept. US Department of Agriculture, Forest Service, Rocky Mountain Research Station. 20, 21

Burner, C.J. 1951. *Characteristics of spawning nests of Columbia River salmon.* Tech. rept. USDI Fish and Wildlife Service Fisheries Bulletin 61. ix, 4, 6

Casado, M.R., Bellamy, P., White, S., Maddock, I., Dunbar, M., & Booker, D. 2005. Defining spatial and temporal hydromorphological sampling strategies for the Leigh Brook river site. *Pages 293–304 of: European Aquatic Modelling Network: proceedings from the final meeting in Silkeborg, Danemark.* 1, 11, 25, 52

Chakravarti, I.M., Laha, R.G., & Roy, J. 1967. *Handbook of methods of applied statistics: techniques of computation, descriptive methods, and statistical inference.* Wiley. 35

Chapman, D.W. 1988. Critical review of variables used to define effects of fines in redds of large salmonids. *Transactions of the American Fisheries Society*, **117**(1), 1–21. 4, 5, 8

Chiles, J.P., & Delfiner, P. 1999. *Geostatistics: modeling spatial uncertainty.* Wiley-Interscience. 13, 29, 31

Chow, V.T. 1959. *Open-channel hydraulics.* McGraw-Hill College. 6, 7

Clifford, N.J., Soar, P.J., Harmar, O.P., Gurnell, A.M., Petts, G.E., & Emery, J.C. 2005. Assessment of hydrodynamic simulation results for eco-hydraulic and eco-hydrological applications: a spatial semivariance approach. *Hydrological processes*, **19**(18), 3631–3648. 29, 30

Cooper, A.C. 1965. *The effect of transported stream sediments on the survival of sockeye and pink salmon eggs and alevin.* Tech. rept. International Pacific Salmon Fisheries Commission Bulletin 18. 6

Cressie, N. 1985. Fitting variogram models by weighted least squares. *Mathematical geology*, **17**(5), 563–586. 31

Crisp, D.T., & Carling, P.A. 1989. Observations on siting, dimensions and structure of salmonid redds. *Journal of Fish Biology*, **34**(1), 119–134. 4, 5, 43, 58

Deutsch, C.V., & Journel, A.G. 1998. *GSLIB: Geostatistical Software Library and User's Guide.* 30

DeVries, P. 1997. Riverine salmonid egg burial depths: review of published data and implications for scour studies. *Canadian Journal of Fisheries and Aquatic Sciences*, **54**(8), 1685–1698. 43

Dingman, S.L. 2009. *Fluvial hydraulics.* Oxford University Press. ix, 1, 3, 7, 8, 9

Dyer, F.J., & Thoms, M.C. 2006. Managing river flows for hydraulic diversity: an example of an upland regulated gravel-bed river. *River Research and Applications*, **22**(2), 257–267. 1

Emmett, W.W., & Leopold, L.B. 1963. Downstream pattern of river-bed scour and fill. *Pages 399–409 of: Proceedings of the Federal Inter-Agency Sedimentation Conference*. US Department of Agriculture. 21

French, R.H. 1985. *Open-channel hydraulics*. McGraw Hill Book Co. 9

Gartner, J.W., & Ganju, N.K. 2002. A preliminary evaluation of near-transducer velocities collected with low-blank acoustic Doppler current profiler. *Water Resources*, **29**, 31. 22

Gauckler, P. 1867. *Etudes Théoriques et Pratiques sur l'Ecoulement et le Mouvement des Eaux*. Gauthier-Villars. 9

González, J.A., Melching, C.S., & Oberg, K.A. 1996. Analysis of open-channel velocity measurements collected with an acoustic Doppler current profiler. *Proc. RiverTech96, IWRA, Chicago, Illinois*, **2**, 838–845. 10

Goovaerts, P. 1997. *Geostatistics for natural resources evaluation*. Oxford University Press. 12, 49

Gordon, N.D., McMahon, T.A., Finlayson, B.L., Gippel, C.J., & Nathan, R.J. 2006. *Stream hydrology: an introduction for ecologists. 2nd Edition*. John Wiley & Sons Inc. 3, 7

Graf, W.H., & Altinakar, M.S. 1998. *Fluvial hydraulics*. Wiley. 6, 7

Gurnell, A.M., Gregory, KJ, & Petts, G.E. 1995. The role of coarse woody debris in forest aquatic habitats: implications for management. *Aquatic Conservation: Marine and Freshwater Ecosystems*, **5**(2), 143–166. 45

Hartley, A.M. 1999. *The pool-riffle sequence as the principal design component of low-gradient, meandering gravel-bed channels*. Master's Thesis, University of Guelph. 14, 41

Hartman, G.F., & Galbraith, D.M. 1970. *Reproductive biology of the Gerrard stock rainbow trout*. Tech. rept. British Columbia Department of Recreation and Conservation, Fisheries Research Section, Fisheries Management Publication 15. x, 59

Heede, B.H., & Rinne, J.N. 1990. Hydrodynamic and fluvial morphologic processes: implications for fisheries management and research. *North American Journal of Fisheries Management*, **10**(3), 249–268. 1

Heiberger, R.M., & Holland, B. 2004. *Statistical analysis and data display: an intermediate course with examples in S-plus, R, and SAS*. Springer Verlag. 22, 35

Hobbs, D.F. 1937. Natural reproduction of quinnat salmon, brown and rainbow trout in certain New Zealand waters. *New Zealand Marine Department Fisheries Bulletin*. x, 59

Imhof, J.G., Fitzgibbon, J., & Annable, W.K. 1996. A hierarchical evaluation system for characterizing watershed ecosystems for fish habitat. *Canadian Journal of Fisheries and Aquatic Sciences*, **53**(S1), 312–326. ix, 3

Journel, A.G., & Huijbregts, C. 1978. *Mining geostatistics*. Harcourt Brace and Company. 47

Julien, P.Y. 2010. *Erosion and sedimentation*. Cambridge University Press. 7, 8, 9, 11, 12, 23, 25

Kemp, J.L., Harper, D.M., & Crosa, G.A. 2000. The habitat-scale ecohydraulics of rivers. *Ecological Engineering*, **16**(1), 17–29. 1, 7

Kerr, D.J., Shen, H.T., & Daly, S.F. 2002. Evolution and hydraulic resistance of anchor ice on gravel bed. *Cold Regions Science and Technology*, **35**(2), 101–114. 40

Kilsby, N.N. 2008. *Reach-scale spatial hydraulic diversity in lowland rivers: characterisation, measurement and significance for fish*. PhD Thesis, University of Adelaide, School of Civil, Environmental and Mining Engineering. 27, 38

Kilsby, N.N., & Walker, K.F. 2010. Linking the swimming ability of small freshwater fish to body form and ecological habit. *Transactions of the Royal Society of South Australia*, **134**(1), 89–96. 1

Knapp, R.A., & Vredenburg, V.T. 1996. Spawning by California golden trout: characteristics of spawning fish, seasonal and daily timing, redd characteristics, and microhabitat preferences. *Transactions of the American Fisheries Society*, **125**(4), 519–531. 4

Kobashi, D. 2009. *Bottom Boundary Layer Physics and Sediment Transport Along a Transgressive Sand Body, Ship Shoal, South-central Louisiana: Implications for Fluvial Sediments and Winter Storms*. Ph.D. thesis, Tokai University. 22

Kondolf, G.M. 2000. Assessing salmonid spawning gravel quality. *Transactions of the American Fisheries Society*, **129**(1), 262–281. 5

Kondolf, G.M., & Wolman, M.G. 1993. The sizes of salmonid spawning gravels. *Water Resources Research*, **29**(7), 2275–2285. x, 4, 59

Kondolf, G.M., Williams, J.G., Horner, T.C., & Milan, D. 2008. Assessing physical quality of spawning habitat. *In: American Fisheries Society Symposium*, vol. 65. American Fisheries Society. ix, 4, 5, 6, 58

Kostaschuk, R., Best, J., Villard, P., Peakall, J., & Franklin, M. 2005. Measuring flow velocity and sediment transport with an acoustic Doppler current profiler. *Geomorphology*, **68**(1-2), 25–37. 10

Lacy, J.R., & Sherwood, C.R. 2004. Accuracy of a pulse-coherent acoustic Doppler profiler in a wave-dominated flow. *Journal of Atmospheric and Oceanic Technology*, **21**(9), 1448–1461. 22

Lacy, J.R., Sherwood, C.R., Wilson, D.J., Chisholm, T.A., & Gelfenbaum, G.R. 2005. Estimating hydrodynamic roughness in a wave-dominated environment with a high-resolution acoustic Doppler profiler. 10

Lane, S.N., Biron, P.M., Bradbrook, K.F., Butler, J.B., Chandler, J.H., Crowell, M.D., McLelland, S.J., Richards, K.S., & Roy, A.G. 1998. Three-dimensional measurement of river channel flow processes using acoustic Doppler velocimetry. *Earth Surface Processes and Landforms*, **23**(13), 1247–1267. 22

Legleiter, C.J., Phelps, T.L., & Wohl, E.E. 2007. Geostatistical analysis of the effects of stage and roughness on reach-scale spatial patterns of velocity and turbulence intensity. *Geomorphology*, **83**(3-4), 322–345. 11, 13, 29, 36, 47, 51

Leopold, L.B. 1994. *A View of the River*. Harvard University Press. 9, 10, 64

Leopold, L.B., & Maddock, T. 1953. *The hydraulic geometry of stream channels and some physiographic implications*. US Government Printing Office. 7

Leopold, L.B., Wolman, M.G., & Miller, J.P. 1995. *Fluvial processes in geomorphology*. Dover Publications. 12

Lotspeich, F.B., Everest, F.H., Forest, P.N., *et al.* 1981. *A new method for reporting and interpreting textural composition of spawning gravel*. Tech. rept. US Department of Agriculture, Forest Service, Pacific Northwest Forest and Range Experiment Station. 21

Lounder, V.G., & Thompson, P.J. 2009. *Whiteman's Creek rehabilitation alternatives: Apps' Mill Conservation Area*. Prepared for CIVE 770 - Stream Restoration (University of Waterloo). 35, 42

MacVicar, B.J., & Roy, A.G. 2011. Sediment mobility in a forced riffle-pool. *Geomorphology*, **125**(3), 445 – 456. 21

Maddux, H.R., Kubly, D.M., deVos Jr, J.C., Persons, W.R., Staedicke, R., & Wright, R.L. 1987. Effects of varied flow regimes on aquatic resources of Glen and Grand Canyons. *Final Report Bureau of Reclamation. Arizona Game and Fish Department, Phoenix*. x, 59

Maindonald, J.H., & Braun, J. 2007. *Data analysis and graphics using R: an example-based approach*. Cambridge University Press. 22

Marchildon, M. 2009. *A High-Resolution Hydrodynamic Investigation of Brown Trout and Rainbow Trout Redds*. Master's Thesis, University of Waterloo, Civil/Environmental Engineering. ix, 10, 14, 18, 19, 27, 38, 41

Marchildon, M.A., Annable, W.K., Imhof, J.G., & Power, M. 2011. A high-resolution hydrodynamic investigation of brown trout (Salmo trutta) and rainbow trout (Oncorhynchus mykiss) redds. *River Research and Applications*, **27**(3), 345–359. 8, 66

Martini, M., Lightsom, F.L., Sherwood, CR, Xu, J., Lacy, J.R., Ramsey, A., & Horwitz, R. 2005. *Hydratools, a MATLAB® based data processing package for Sontek Hydra data*. 22

Meyer-Peter, E., & Müller, R. 1948. Formulas for bed-load transport. *Pages 39–64 of: Proceedings of the 2nd Meeting of the International Association for Hydraulic Structures Research*. 12

Middleton, G.V., & Southard, J.B. 1984. *Mechanics of sediment movement*. Society of Economic Paleontologists and Mineralogists. 8, 9

Moir, H.J., & Pasternack, G.B. 2008. Relationships between mesoscale morphological units, stream hydraulics and Chinook salmon (*Oncorhynchus tshawytscha*) spawning habitat on the Lower Yuba River, California. *Geomorphology*, **100**(3-4), 527–548. 4, 7, 32

Montgomery, D.R., Buffington, J.M., Peterson, N.P., Schuett-Hames, D., & Quinn, T.P. 1996. Stream-bed scour, egg burial depths, and the influence of salmonid spawning on bed surface mobility and embryo survival. *Canadian Journal of Fisheries and Aquatic Sciences*, **53**(5), 1061–1070. 6, 43

Morris, M.D. 1991. On counting the number of data pairs for semivariogram estimation. *Mathematical geology*, **23**(7), 929–943. 30, 47

Nawa, R.K., & Frissell, C.A. 1993. Measuring scour and fill of gravel streambeds with scour chains and sliding-bead monitors. *North American Journal of Fisheries Management*, **13**(3), 634–639. 12, 21

Nikora, V.I., Goring, D.G., & Biggs, B.J.F. 1998. On gravel-bed roughness characterization. *Water resources research*, **34**(3), 517–527. 9, 26

Nikuradse, J. 1933. Strömungsgestze in rauhen Rohren. *Forschung auf dem Gebiete des Ingenieurwesens*. 9

Oberg, K., Mueller, D.S., *et al.* 2007. Validation of streamflow measurements made with acoustic Doppler current profilers. *Journal of Hydraulic Engineering*, **133**, 1421. 10

Ontario Geological Survey. 2007. *OGS Earth 2: Data for Land and Water Stewardship*. 14, 41

Ontario Ministry of Natural Resources, The. 2008. *Southern Ontario Land Resource Information System (SOLRIS) Land Use Data"*. 14

Ottaway, E.M., Carling, P.A., Clarke, A., & Reader, N.A. 1981. Observations on the structure of brown trout redds. *Journal of Fish Biology*, **19**(5), 593–607. 4, 8

Parsons, M., Thoms, M.C., & Norris, R.H. 2004. Using hierarchy to select scales of measurement in multiscale studies of stream macroinvertebrate assemblages. *Journal of the North American Benthological Society*, **23**(2), 157–170. 3

Pebesma, E.J., & Wesseling, C.G. 1998. Gstat: a program for geostatistical modelling, prediction and simulation. *Computers & Geosciences*, **24**(1), 17–31. 30

Platts, W.S., Shirazi, M.A., & Lewis, D.H. 1979. *Sediment particle sizes used by salmon for spawning with methods for evaluation*. Tech. rept. Environmental Protection Agency, Office of Research and Development, Corvallis Environmental Research Laboratory. x, 59

Reiser, D.W. 1976. *Determination of physical and hydraulic preferences of brown and brook trout in the selection of spawning locations*. M.Phil. thesis, University of Wyoming. x, 4, 59

Rennie, C.D., & Millar, R.G. 2000. Spatial variability of stream bed scour and fill: a comparison of scour depth in chum salmon (Oncorhynchus keta) redds and adjacent bed. *Canadian Journal of Fisheries and Aquatic Sciences*, **57**(5), 928–938. 5, 6

Richards, K.S. 1973. Hydraulic geometry and channel roughness; a non-linear system. *American Journal of Science*, **273**(10), 877. 43

Rosgen, D.L., & Silvey, H.L. 1996. *Applied river morphology*. Vol. 1481. Wildland Hydrology. 42

Roy, M. 2006. *Caracterisation de l'ecoulement turbulent en riviere a lit de graviers peu profonde: Strategie d'echantillonnage, interpolation et structure spatiale.* Master's Thesis, Universite de Montreal, Department of Geography. 11, 13, 29

Roy, M.L., Roy, A.G., & Legendre, P. 2010. The relations between standardfluvial habitat variables and turbulent flow at multiple scales in morphological units of a gravel-bed river. *River Research and Applications*, **26**(4), 439–455. 1

Schlichting, H., & Gersten, K. 2000. *Boundary-layer theory.* Springer-Verlag. 9

Schmetterling, D.A. 2000. Redd characteristics of fluvial westslope cutthroat trout in four tributaries to the Blackfoot River, Montana. *North American Journal of Fisheries Management*, **20**(3), 776–783. 4, 6, 65

Smart, G.M. 1999. Turbulent velocity profiles and boundary shear in gravel bed rivers. *Journal of Hydraulic Engineering*, **125**, 106. 8, 9, 10

Song, T., & Chiew, Y.M. 2001. Turbulence measurement in nonuniform open-channel flow using acoustic Doppler velocimeter (ADV). *Journal of engineering mechanics*, **127**, 219. 8

SonTek/YSI, Inc. 2004. *PC-ADP Read Me First!* San Diego, California. 18, 19, 22

Spina, A.P. 2001. Incubation discharge and aspects of brown trout population dynamics. *Transactions of the American Fisheries Society*, **130**(2), 322–327. 5

Spoon, R.L. 1985. *Reproductive biology of brown and rainbow trout below Hauser Dam, Missouri River, with reference to proposed hydroelectric peaking.* M.Phil. thesis, Montana State University. x, 59

Stone, M.C., & Hotchkiss, R.H. 2007. Evaluating velocity measurement techniques in shallow streams. *Journal of Hydraulic Research*, **45**(6), 752–762. 22

Thibodeaux, L.J., & Boyle, J.D. 1987. Bedform-generated convective transport in bottom sediment. 6

Thomson, J.R., Taylor, M.P., Fryirs, K.A., & Brierley, G.J. 2001. A geomorphological framework for river characterization and habitat assessment. *Aquatic Conservation: Marine and Freshwater Ecosystems*, **11**(5), 373–389. 1

Thurow, R.F., & King, J.G. 1994. Attributes of Yellowstone cutthroat trout redds in a tributary of the Snake River, Idaho. *Transactions of the American Fisheries Society*, **123**(1), 37–50. 6

Tilston, M. 2005. *Three-dimensional flow structure, turbulence and bank erosion in a 180 meander loop*. Master's Thesis, Universite de Montreal, Department of Geography. 10

Tukey, J.W. 1973. *The problem of multiple comparisons*. Princeton University. 35

Von Kármán, T. 1930. *Mechanische ähnlichkeit und turbulenz*. Weidmannsche Buchh. 7

Wackernagel, H. 1995. *Multivariate geostatistics*. Vol. 220. Springer Berlin. 28, 29

Webster, R., & Oliver, M.A. 2007. *Geostatistics for environmental scientists*. John Wiley & Sons Inc. 30, 47, 49

Wiberg, P.L., & Smith, J.D. 1987. *Initial motion of coarse sediment in streams of high gradient*. Tech. rept. 23

Witzel, L.D., & MacCrimmon, H.R. 1983. Redd-site selection by brook trout and brown trout in southwestern Ontario streams. *Transactions of the American Fisheries Society*, **112**(6), 760–771. 4, 43

Woods, A.J., Omernik, J.M., Brown, D.D., & Kiilsgaard, C.W. 1996. Level III and IV ecoregions of Pennsylvania and the Blue Ridge mountains, the Ridge and Valley, and the central Appalachians of Virginia, West Virginia, and Maryland. *EPA/600R*, **96**, 077. 3

Wu, F.C. 2000. Modeling embryo survival affected by sediment deposition into salmonid spawning gravels: Application to flushing flow prescriptions. *Water Resources Research*, **36**(6), 1595–1603. 6, 65

Yalin, M.S. 1992. *River mechanics*. Pergamon Press. 8, 9

Yen, B.C. 2002. Open channel flow resistance. *Journal of Hydraulic Engineering*, **128**(1), 20–39. 10

Zimmer, M.P., & Power, M. 2006. Brown trout spawning habitat selection preferences and redd characteristics in the Credit River, Ontario. *Journal of fish biology*, **68**(5), 1333–1346. ix, 4, 18